

## **INFORMATION TO USERS**

This manuscript has been reproduced from the microfilm master. UMI films the text directly from the original or copy submitted. Thus, some thesis and dissertation copies are in typewriter face, while others may be from any type of computer printer.

**The quality of this reproduction is dependent upon the quality of the copy submitted.** Broken or indistinct print, colored or poor quality illustrations and photographs, print bleedthrough, substandard margins, and improper alignment can adversely affect reproduction.

In the unlikely event that the author did not send UMI a complete manuscript and there are missing pages, these will be noted. Also, if unauthorized copyright material had to be removed, a note will indicate the deletion.

Oversize materials (e.g., maps, drawings, charts) are reproduced by sectioning the original, beginning at the upper left-hand corner and continuing from left to right in equal sections with small overlaps. Each original is also photographed in one exposure and is included in reduced form at the back of the book.

Photographs included in the original manuscript have been reproduced xerographically in this copy. Higher quality 6" x 9" black and white photographic prints are available for any photographs or illustrations appearing in this copy for an additional charge. Contact UMI directly to order.

**UMI**

A Bell & Howell Information Company  
300 North Zeeb Road, Ann Arbor MI 48106-1346 USA  
313/761-4700 800/521-0600



# **Receiver Issues Related to Spread Spectrum Communications**

**by**

**Mark David Hahm**

**Submitted in Partial Fulfillment  
of the  
Requirements for the Degree  
Doctor of Philosophy**

**Supervised by  
Professor Edward L. Titlebaum  
and  
Professor Eby G. Friedman**

**Department of Electrical Engineering  
The College  
The School of Engineering and Applied Sciences**

**University of Rochester  
Rochester, New York**

**1997**

**UMI Number: 9728443**

---

**UMI Microform 9728443**  
**Copyright 1997, by UMI Company. All rights reserved.**

**This microform edition is protected against unauthorized  
copying under Title 17, United States Code.**

---

**UMI**  
**300 North Zeeb Road**  
**Ann Arbor, MI 48103**

## CURRICULUM VITAE

The author was born in Rochester, New York on October 20, 1971. He attended the University of Rochester from the fall of 1989 to the spring of 1993 and graduated with a Bachelor of Science and a Master of Science degree in electrical engineering in May of 1993. As an undergraduate, he was inducted into the Phi Beta Kappa academic honor society, was awarded the Donald M. Barnard prize for outstanding scholarship, and graduated with Highest Distinction at the top of his engineering class. In the fall of 1993, he began Ph.D. studies in electrical engineering at the University of Rochester under the direction of Professor Edward L. Titlebaum and Professor Eby G. Friedman. His research centered around the signal processing algorithms and physical implementation of spread spectrum receivers. In the spring of 1994, he was awarded the AT&T Bell Laboratories Ph.D. fellowship, and he interned at AT&T Bell Laboratories in Whippany, New Jersey during the summer of 1995. Currently, the author works for Lucent Technologies in Whippany, New Jersey.

## ABSTRACT

Of central interest in this dissertation are algorithms, signals, and circuit structures appropriate for use within the receivers of spread spectrum communication systems. In general, tasks that a spread spectrum receiver must perform include channel estimation, timing and frequency alignment for proper demodulation, and despreading of the received wideband waveform.

Pertaining to the task of channel estimation, the problem of obtaining accurate parameter estimates in a Doppler multipath environment is considered. Through analysis and simulations, it is shown that deconvolution algorithms designed for multipath parameter estimation in the absence of Doppler may also be profitably applied to a Doppler multipath environment. Thus employed, these deconvolution procedures are able to produce estimates of the Doppler channel parameters with much finer resolution than correlation methods.

Before channel estimation or demodulation can occur, the receiver must first know or acquire the precise carrier frequency of the transmitted waveform. The correlation-based receivers that are used within spread spectrum systems are sensitive to small mismatches between the local oscillator frequencies of the transmitter and receiver. Algorithm and signal design issues associated with this problem are discussed, and simulation results are given for a new algorithm which yields a dramatic decrease in the time needed by a spread spectrum receiver to acquire the carrier frequency of the received signal.

A parallel matched filter is central to the operation of an asynchronous spread spectrum receiver and permits reduced search and acquisition times in synchronous systems. The matched filter is often required to perform tens of billions of multiply-add operations per second. This enormous computational load tends to translate into a circuit that can quickly drain the power source of a portable spread spectrum receiver. In this dissertation, a methodology is discussed for implementing low-power matched filters. Both analog and digital circuits are considered, with power consumption being used as the primary metric of comparison. This methodology is applied to the physical implementation of an integrated circuit matched filter built in a 1.2  $\mu\text{m}$  analog CMOS technology. The design, simulation, and experimental results associated with this filter are also presented.

# TABLE OF CONTENTS

<b>Chapter 1</b>	<b>Introduction .....</b>	<b>1</b>
1.1	Overview .....	1
1.2	Dissertation Goals .....	4
1.3	Dissertation Outline .....	6
<b>Chapter 2</b>	<b>A Review of Spread Spectrum Systems and Techniques</b>	<b>10</b>
2.1	Spread Spectrum: The Concept .....	11
2.2	Methods of Spectrum Spreading and De-Spreading .....	13
2.2.1	Direct Sequence Spread Spectrum Systems .....	14
2.2.2	Frequency-Hopping Spread Spectrum Systems .....	18
2.2.3	Pulsed FM (Chirp) Spread Spectrum Systems .....	22
2.3	Some Benefits of Spread Spectrum Systems .....	25
2.3.1	Anti-Jamming Properties .....	25
2.3.2	High Resolution Ranging (Radar) Applications .....	27
2.3.3	Covertness and Low-Power Signal Transmission .....	27
2.3.4	Cryptographic Incorporation .....	28
2.3.5	Multipath Mitigation and Exploitation .....	29
2.3.6	Multiple-Access Overlay .....	32
<b>Chapter 3</b>	<b>Parameter Estimation of Specular Multipath Channels in the Presence of Doppler .....</b>	<b>34</b>
3.1	Introduction .....	35
3.2	Inverse Filtering in the Presence of Doppler Multipath .....	41
3.2.1	The Inverse Filter Output for a Windowed Sinusoid Input .....	43
3.2.1.1	Derivation of the Inverse Filter Output for a Windowed Sinusoid Input .....	46
3.2.2	The Inverse Filter Output for a Transmitted Signal with a Flat Spectrum .....	52
3.2.2.1	The Ambiguity Function Effect .....	54
3.2.2.2	The Cosine Effect .....	56
3.2.3	The Total Estimate of the Inverse Filter Output .....	61
3.3	Deconvolution in the Presence of Doppler .....	66
3.3.1	Doppler Multipath Parameter Estimation Via POCS ..	67

3.3.1.1	Description of the Post-Processor Curve-Fitting Operation .....	74
3.3.2	Least Squares Estimation Applied to Doppler Multipath .....	76
3.3.3	A Word About Resolution .....	83
3.4	Discussion and Conclusions .....	84
<b>Chapter 4</b>	<b>Analysis of Low-Power Matched Filter Structures for Asynchronous CDMA Receivers .....</b>	<b>88</b>
4.1	Introduction .....	89
4.2	A Review of Matched Filters .....	90
4.3	A Digital Matched Filter Implementation .....	94
4.3.1	Data and Reference Quantization Levels .....	96
4.3.2	Digital Matched Filter Subcircuits .....	97
4.3.3	Power Estimate of the Digital Matched Filter .....	100
4.4	An Analog Matched Filter Implementation .....	103
4.4.1	Analog Matched Filter Subcircuits .....	104
4.4.2	Analog Matched Filter Power Estimate .....	106
4.5	Comparison of the Digital and Analog Matched Filter Implementations .....	109
4.6	Conclusions .....	111
<b>Chapter 5</b>	<b>Signal Design Issues and Local Oscillator Mismatch ..</b>	<b>115</b>
5.1	Introduction .....	115
5.2	Suitable Signals.....	117
5.3	An Algorithm for Speedy LO Alignment .....	122
5.4	Conclusions.....	127
<b>Chapter 6</b>	<b>Design, Simulation, and Experimental Results for a Parallel Programmable Matched Filter Circuit .....</b>	<b>128</b>
6.1	Pseudo-FM Asynchronous CDMA Wireless Voice.....	129
6.2	Design of an Integrated Circuit Matched Filter.....	132
6.2.1	Process Selection: Analog or Digital? .....	133
6.2.2	Matched Filter Circuit Design.....	133
6.2.2.1	The CCD Delay Line.....	134
6.2.2.2	The CCD Floating Gate Taps.....	138
6.2.2.3	Tap Weight Storage and Signal Summing Busses.....	139
6.2.2.4	Other Chip Features.....	140
6.2.2.5	Chip Floorplan and Design Statistics .....	142

6.3	Conclusions.....	144
<b>Chapter 7</b>	<b>Summary and Conclusions .....</b>	<b>146</b>
7.1	Review of Dissertation Contributions.....	146
<b>Chapter 8</b>	<b>Future Work .....</b>	<b>149</b>
8.1	Future Work in Multipath Parameter Estimation.....	150
8.2	Future Work in Matched Filter Power Estimation.....	151
8.3	Future Work in Local Oscillator Alignment .....	152
8.4	Future Work in CDMA Receiver Integration.....	153
8.5	Concluding Remarks.....	155
<b>Bibliography</b>	.....	<b>156</b>
<b>Appendix</b>	<b>Publications .....</b>	<b>164</b>

## LIST OF TABLES

<u>Table</u>	<u>Title</u>	<u>Page</u>
6.1	Computational requirements for 3.2 kHz bandwidth speech coders [101]. .....	130
6.2	Summary of chip features and specifications. ....	145

## LIST OF FIGURES

<u>Figure</u>	<u>Title</u>	<u>Page</u>
1.1	The block diagram of a simplified generic spread spectrum receiver is given. The contributions of this dissertation —as they pertain to the overall function of spread spectrum receivers in general— are annotated in the shaded boxes and linked to the appropriate receiver blocks.....	9
2.1	Shown in the figure are some of the key features of a DS-SS system. Spreading by the PN code is demonstrated in (a), the spectral characteristics of the DS-SS waveform are shown in (b), and block diagrams of a transmitter and synchronous receiver are shown in (c). .....	16
2.2	A matched filter block, which is used in asynchronous spread spectrum receivers in place of the correlator block of Figure 2.1c, is shown in (a). In (b) are given a sample matched filter output and an illustration of how data recovery can be achieved by thresholding the matched filter output. .....	17
2.3	Key features of a FH-SS system. A hop pattern is shown in (a), and a corresponding waveform is shown in (b). The spectrum of the waveform is shown in (c) and (d) for two different values of TW. Transmitter and receiver structures for a slow FH-SS system and a fast FH-SS system are shown in (e) and (f), respectively. .....	20
2.4	A chirp waveform is shown in (a), and the output of a chirp matched filter output is shown in (b). An illustration of the detection properties of chirp systems in a Doppler environment or in a system that contains local oscillator drift phenomena is given in (c). .....	24
2.5	In (a) is shown a matched filter output from a system that is operating in the presence of four strong multipath components. The three-fingered rake receiver that is shown in (b) combines the energy from the three strongest paths, while the searching finger looks for new strong paths. .....	31

3.1	Sources of Doppler multipath. ....	36
3.2	The block diagram for the Doppler multipath channel model is shown at the left. The right side of the figure shows the generalized block diagram of a deconvolution-based channel parameter estimation system. ....	41
3.3	(a) shows the characteristics the spectrum of a well-behaved wideband probing signal, $X(\omega)$ , and (b) shows the characteristics of the same spectrum when plotted on a log scale. (c) shows what happens when $X(\omega)$ is inverted. Note the energy in the region of the spectrum formerly occupied by the skirts. (d) shows the output spectrum of the inverse filter (IF); note that the skirts of the finite time-length transmitted signal and Doppler mismatched with the stored reference signal cause significant energy to appear in the output spectrum of the IF in the region formerly occupied by the signal skirts. (e) shows the flat part of the IF output spectrum, and (f) shows the remaining part of the IF output spectrum, which contains skirt effects. The 3 dB points of $X(\omega)$ are also shown on the $\omega$ axis. ....	54
3.4	Plot of the spectra of a linear FM chirp and a windowed sinusoid, both of sampled time-length $N = 50$ . Note the similarity in the form of the skirts. This similarity is employed to approximate the effects of the spectral skirts on the output of an IF/deconvolution system. ....	57
3.5	Contour of integration for analysis of the inverse filter output when the transmitted signal has a flat bandwidth. ....	58
3.6	(a) shows a mesh plot of the output of an ideal inverse filter (IF) in the presence of Doppler for the case when the input is a linear FM chirp with sampled time-length of $N=450$ and radian bandwidth of $BW=0.8\pi$ . (b) shows a contour plot of the same data. (c) shows the contour plot of the IF output when only the region of the IF output spectrum inside $[\omega_1, \omega_2]$ (as shown in Figure 3.1) is considered, thus showing the ambiguity function effect. (d) considers only the effect of the region of the IF output spectrum outside $[\omega_1, \omega_2]$ and shows that this region contributes directly to the cosine effect. (e) shows a slice of the IF output parallel to the Doppler axis at $Delay = 0$ and overlays the two contributors to the total IF output, verifying the presence and relative weights of the auto-ambiguity function and cosine effects	

	as described by equation (3.42). .....	64
3.7	The plots show the output of an ideal inverse filter (IF) for four different probing signals. The probing signals differ in their design and in the degree to which they can be considered as well-behaved. Each probing signal has a sampled time-length of $N = 360$ and a radian bandwidth of $B W_x = 0.5\pi$ . (a) shows the IF output for a linear FM chirp. (b) is for a hyperbolic FM sweep. (c) is for a linear congruence frequency-hop code with prime = 11 and multiplier = 2. (d) is for a Welch-Costas frequency-hop code with prime = 11, primitive root = 2, and multiplier = 3. Note that the signals used for (a) and (b) are reasonably well-behaved, and the IF outputs shown in (a) and (b) correspond closely to the estimate in equation (3.42b). The IF output (c) begins to depart from the estimates of (3.42b), showing significant artifacts away from the Doppler axis. The IF output of (d) is for the case when the probing signal is a Welch-Costas frequency-hop code. The phase jumps in this signal are more severe than those in the linear congruence code, as is evidenced in (d) by the greater prevalence of artifacts in the IF output away from the Doppler axis and also by the weakening of the ridge along the Doppler axis. .....	65
3.8	(a) shows the output of a correlation-type estimator when the input is a linear FM chirp with time-length $N = 450$ and radian bandwidth of $B W_x = 1.0$ . Note how the two closely spaced peaks near <i>Delay</i> = 10 are not resolved and how the range-Doppler coupling of the chirp signal causes "tilt" and, hence, uncertainty along the Doppler axis. (b) shows the output of the POCS deconvolution system for a CW probing signal. (c) shows the final result after post-processing that is based on equation (3.42). Note how most of the extraneous, noise-related information is removed by the post-processing. .....	71
3.9	(a) shows the output of the POCS deconvolution system when the probing signal is a hyperbolic congruence frequency-hop code [25] with time-length $N = 450$ and radian bandwidth of $B W_x = 1.25$ . (b) shows the result after post-processing based on (3.42) has been applied to the POCS output. .....	73
3.10	(a) shows the output of a deconvolution system based on least-squares (LS) estimation. (b) shows the final output after post-processing, which relies on the result given in equation (3.42),	

	has been applied to the LS output. Note that, in this case, the post-processing was able to reject all of the noise-related artifacts..	79
3.11	Performance of the least squares (LS) deconvolution procedure in the presence of noise and Doppler. (a) Probability of a miss as a function of input SNR. (b) Probability of a false alarm as a function of input SNR. (c) Average delay uncertainty as a function of input SNR. (d) Average Doppler error as a function of input SNR. ....	81
4.1	The utility of a matched filter in a communications environment is shown in (a) through (d). The matched filter can pluck a pulse-compression spread-spectrum signal (in this case a hyperbolic-congruence frequency-hop code [25]) out of a noisy channel by concentrating the energy of the signal into a small time slot around $t = T$ . ....	92
4.2	The block diagram of the parallel matched filter structure is shown in (a). The digital and analog circuit implementations are outlined in (b) and (c), respectively. ....	95
4.3	Effects of technology scaling on digital circuit power consumption. ....	103
4.4	Analog matched filter power as a function of supply voltage and filter length. ....	108
4.5	Surface of equal power dissipation for the analog and digital matched filter implementations as a function of filter length, sampling frequency, and technology. ....	110
4.6	Surface of equal power dissipation for the analog and digital matched filter implementations, demonstrating the effect of varying quantization level (or, equivalently, varying the analog SNR). The $Q_d \times Q_r$ bit equivalent quantization levels for Figures 6a through 6e are (a) 2 x 2 bit, (b) 3 x 2 bit, (c) 4 x 2 bit, (d) 5 x 2 bit, and (e) 6 x 2 bit. The analog process parameter $N_{ss}$ has a value of $5000 / \mu\text{m}^2 \cdot \text{eV}$ . ....	112
4.7	Surface of equal power dissipation for the analog and digital matched filter implementations, demonstrating the effect of improving the quality of the analog fabrication process — as measured by the surface state density, $N_{ss}$ (smaller values of	

$N_{ss}$ indicate a superior analog process). Figures 7a through 7d are for a 4 x 2 bit equivalent SNR and $N_{ss}$ values of (a) 500 / $\mu\text{m}^2 \cdot \text{eV}$ , (b) 1000 / $\mu\text{m}^2 \cdot \text{eV}$ , (c) 2000 / $\mu\text{m}^2 \cdot \text{eV}$ , (d) 5000 / $\mu\text{m}^2 \cdot \text{eV}$ .....	113
5.1 Generic ambiguity function. ....	116
5.2 Ambiguity function of a linear FM chirp. ....	118
5.3 Hopping patterns of the entire linear congruence code family for $p = 11$ . An enlarged view of the $a = 3$ code is shown with a description of the axes.....	120
5.4 Ambiguity function of the $a = 3$ , $p = 11$ linear congruence FH code. ....	120
5.5 Auto-hit array of the $a = 3$ , $p = 11$ linear congruence FH code.....	121
5.6 Contour plot of the ambiguity function shown in Figure 5.4.....	121
5.7 Speedy acquisition/alignment process for linear congruence FH code. ....	124
5.8 Acquisition/alignment process for a typical spreading waveform... .	125
5.9 Acquisition time required for the conventional search algorithm (top curve) and the speedy receiver alignment algorithm (bottom curve). .	126
6.1 Important waveforms in the pseudo-FM transmitter and receiver. (a) the original analog waveform (smooth thick curve), the sampled waveform (thin solid horizontal line segments), and various control signals (thin gray lines). The length of time between successive transmitted spreading codes carries the amplitude information and time duration of each sample of the analog waveform. Through the use of a matched filter, the receiver is able to recover this timing information, as shown in (b), and reconstruct the sampled waveform. ....	131
6.2 Pictorial and schematic view of a single analog matched filter cell. ....	134
6.3 Shape and timing characteristics of the CCD delay line clock waveforms for a system sampling frequency of 10 MHz. ....	135

6.4	Shown in (a) is an oscilloscope trace of a sinusoidal input (top) and CCD delay line output (bottom). The bottom trace in (b) provides a close-up view of the CCD delay line output waveform. The output is valid during the high amplitude portion of the step-like waveform. The top trace in (b) is the phase 1 CCD clock.....	136
6.5	A photograph of the test setup used to obtain the traces shown in Figure 6.4.....	137
6.6	A close-up view of the circuit under test. ....	138
6.7	Matched filter chip floorplan.....	143
6.8	Matched filter chip microphotograph. ....	144

# Chapter 1 Introduction

---

Contained in this chapter is a brief overview of the goals of this dissertation and the context into which this work may be applied. As such, this chapter is void of great detail and is meant to serve as a springboard, launching the reader into the dissertation contributions in the succeeding chapters.

## 1.1 Overview

Of central interest in this dissertation are the algorithms, signals, and circuit structures that are appropriate for use within the receivers of spread spectrum systems. The problem of obtaining accurate parameter estimates in a Doppler multipath environment is considered. Provided also are insight into the design and circuit implementation of programmable parallel matched filters, as well as algorithm and signal design for speedy alignment of the transmitter and receiver local oscillators. The issues that are explored have application to radar and sonar systems and multiple-access spread spectrum communication links.

Generally the receiver of a communication system is significantly more

complex than the transmitter. This condition holds true for spread spectrum systems as well. The spread spectrum transmitter is responsible for the data encoding, spectrum spreading, and baseband-to-RF conversion. The receiver must deal with the effects of a noisy channel in addition to undoing each operation that the transmitter had previously performed on the input data stream.

A parallel matched filter has been shown to be an optimum receiver in the presence of white gaussian noise. By *optimum* it is meant that the signal-to-noise ratio at the matched filter output is the greatest possible for any given linear filter. In addition, a matched filter is a useful device for discriminating between multiple-access spread spectrum waveforms that occupy the same bandwidth at the same moment in time. A matched filter is essential for proper operation of an asynchronous spread spectrum communication system and can be applied to reduce search and acquisition times in synchronous systems, as is discussed in Chapters 4 and 5.

Integrated circuit matched filters, however, possess several characteristics that have kept them from widespread use in commercial communication systems. Most notably, matched filters are large and power hungry.<sup>1</sup> These two qualities are not desirable for small, battery-powered communication terminals, and, at the cost of a decrease in performance, a much simpler device —called a *correlator*— is often used in place of a matched filter (in a later chapter, the relative advantages of these two

---

<sup>1</sup> The clarification is made here that “large” and “power hungry” are descriptors that are relevant in the integrated-circuit (IC) community. Otherwise, for those not familiar with IC size and power budgets, it may be difficult to understand how a device that occupies a few square millimeters of a silicon wafer and consumes less than one hundredth the power of an average light bulb could be considered “large” and “power hungry”.

different types of correlation processing are discussed in more detail).

Buildings, low-flying airplanes, and geographic features such as mountains can reflect incident RF energy in much the same way that a mirror can reflect sunlight. The transmitted RF energy that is reflected from one or more such surfaces and that reaches the intended RF receiver causes a *specular multipath condition*. The implications of the presence of a specular multipath condition in a communications channel are different for various communication systems. Within a narrowband AM or FM communications environment, the energy that arrives at the receiver via multiple reflective surfaces may add constructively or destructively and result in loss of signal information through fading effects, or the energy may cause ghosting effects, as visible on analog television sets. Within a radar or sonar system, the reflective surfaces of the multipath environment may be aircraft or naval vessels, and a reflection from one of these surfaces *is* the signal of interest, since the redirected energy contains information about the vehicle that produced the reflection. Within a multiple-access spread spectrum communication system, the wide bandwidth of the transmitted waveforms may allow accurate estimation of the time delays associated with each multipath component. Using this knowledge of the multipath delay parameters, energy from the distinct multipath reflectors may be combined for an effective increase in the average received signal-to-noise ratio. Thus, the presence of multipath in a narrowband system generally degrades system performance, the presence of multipath in a spread spectrum system can —with an appropriate energy combination scheme— enhance system performance, and the multipath parameters

contain the information of interest in a radar or sonar system.

Though the effect of multipath may be different for different communication systems, an accurate estimate of the multipath parameters can benefit all of the aforementioned systems. The information may be used in a narrowband system to combat fading through some kind of equalization or subtraction scheme. The radar or sonar system may glean range, speed, and other information from the multipath parameters. The spread spectrum communication system can use the multipath parameters to realize the energy combination scheme alluded to above.

Often, the multipath parameter estimates must be obtained from an environment where the reflecting surfaces of the multipath are in motion relative to the spread spectrum receiver. A parallel matched filter can be used to obtain an estimate of the Doppler multipath parameters, but the delay and Doppler resolution of such a system is limited by the time-bandwidth product of the probing waveform. There are applications where greater resolution is required, necessitating increased computational effort to achieve this improvement in resolution.

## 1.2 Dissertation Goals

As discussed in section 1.1, high resolution multipath parameter estimates can be used by a number of communication systems to improve the received signal quality and/or to permit proper operation of the system. Programmable parallel matched filters also have great utility when used within spread spectrum receivers,

but the physical characteristics of the matched filters often prohibit their employment in applications where portable, battery-powered receivers are required. Therefore the intended goals of this dissertation are as follows:

- 1) *Develop and characterize the resolution capabilities of a signal processing parameter estimation tool for use in multipath environments where the specular reflectors are in motion relative to the receiver. The tool should lead to estimates of the relative velocity of the specular reflectors and have delay resolution capabilities superior to conventional matched filter based processing methods.*
- 2) *Analyze and provide a design methodology for choosing the appropriate implementing technology for low-power integrated circuit implementations of programmable parallel matched filters for use in portable receivers of asynchronous spread spectrum communication systems.*
- 3) *Explore the role of signal design as a means to reduce the signal acquisition times of spread spectrum receivers that employ matched filter processing. Particular attention will be paid to the case where multiple spread spectrum waveforms may coexist in the same bandwidth and at the same moment in time.*
- 4) *Design and evaluate an integrated circuit programmable parallel matched filter suitable for use in a portable asynchronous spread spectrum receiver.*

### 1.3 Dissertation Outline

Spread spectrum communication systems have in the past been widely applied primarily in military and satellite communications. Only within the last decade have systems that employ spread spectrum methods become available to the general populace. Perhaps for these reasons, the issues and benefits associated with such systems are largely unrecognized.

In Chapter 2 in this dissertation, a brief overview of the fundamental concepts of spread spectrum communication systems is presented. The motivation for spectrum spreading, based on the information theoretical concepts of C.E. Shannon, is reviewed, several of the various means of spectrum spreading are explained, and a discussion of some of the advantages of spread spectrum systems is provided. The material of Chapter 2 is presented in tutorial form and is meant to familiarize the reader with concepts and terminology that are applied in subsequent chapters.

Some waveforms used in spread spectrum systems have properties that facilitate precise distance measurements. At times, however, a greater resolution than that afforded by spread spectrum methods alone is desired. Therefore, various deconvolution methods (described in more detail in Chapter 3) may be used in tandem with spread spectrum waveforms to achieve the desired resolution. The response and resolution properties of these deconvolution methods in a *Doppler* multipath environment (i.e., where motion of the specular multipath reflectors

relative to the receiver causes a time-scaling of the received signal), however, are not precisely known.

In Chapter 3, a known signal processing algorithm that uses deconvolution for obtaining high resolution multipath parameter estimates is investigated. It is shown that, with minor modifications, this algorithm becomes a suitable tool for use in a Doppler multipath environment. A general characterization of deconvolution methods in the presence of Doppler multipath is given, resolution properties are described, and applications are discussed.

For those applications where the superior range resolution of the deconvolution methods is not a prerequisite, conventional correlation processing may be employed. For these applications, a parallel matched filter may be utilized.

A matched filter can detect the presence of a properly designed waveform, even if the adverse effects of the channel have buried the waveform in noise. The parallel matched filter is an essential component of an asynchronous spread spectrum communication system and may be used within synchronous spread spectrum systems to reduce the initial code acquisition time and to exploit the diversity effects of multipath.

The integrated circuit implementation of low-power matched filters suitable for portable wireless applications is discussed in Chapter 4. The basics of matched filter operation and utility are reviewed, the merits of both analog and digital circuit implementations are investigated, and a design methodology is described that may serve as an aid to system designers in choosing an appropriate implementing

technology for maximum power efficiency.

In Chapter 5, signal and algorithm design issues that facilitate speedy signal acquisition of spread spectrum signals in an environment prone to local oscillator mismatch are investigated. A novel acquisition scheme is proposed which may reduce search and acquisition time by orders of magnitude, compared to conventional acquisition methods.

The methodology presented in Chapter 4 is applied in Chapter 6 to the design of an integrated circuit matched filter that is suitable for use in a pseudo-FM asynchronous spread spectrum voice demodulator. Some interesting design issues are described, and results from simulations and experiments are discussed.

A review of the dissertation contributions is given in Chapter 7. Future work in the field of spread spectrum receiver issues is outlined in Chapter 8.

A simple generic spread spectrum receiver is shown below in Figure 1.1. The function of the individual blocks is explained in Chapter 2. In the figure, the contributions of this dissertation and are indicated. The figure itself serves as a summary of the outline given above and unifies the separate topics of the following chapters under the heading of *Receiver Issues Related to Spread Spectrum Communications*.

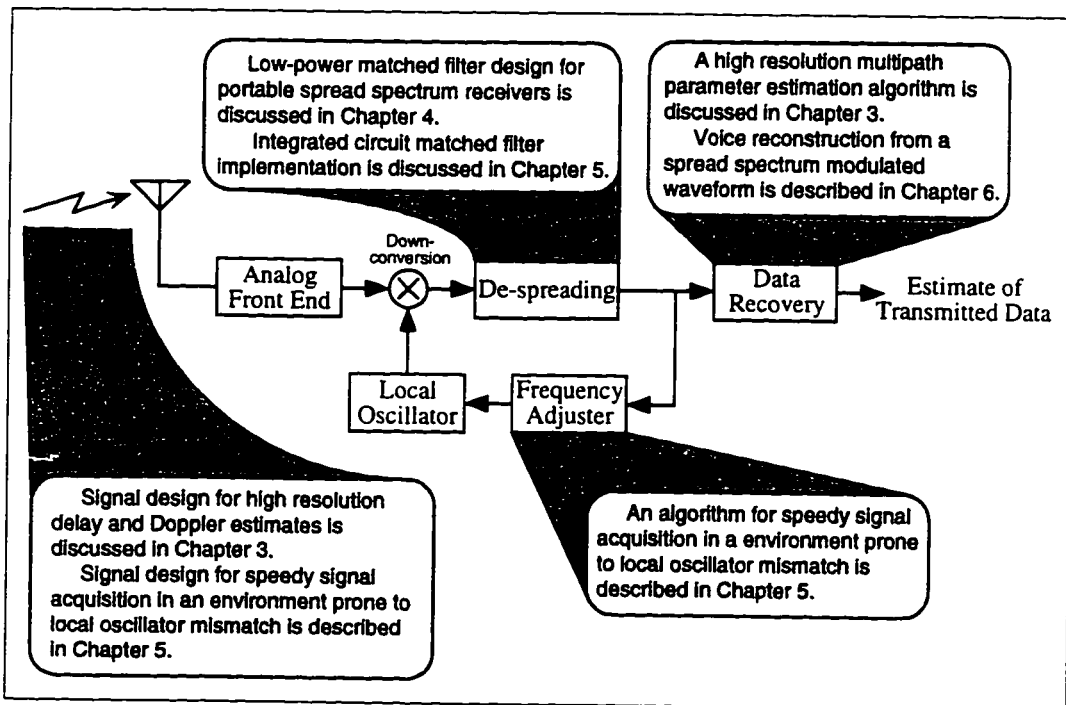


**Figure 1.1** The block diagram of a simplified generic spread spectrum receiver is given. The contributions of this dissertation —as they pertain to the overall function of spread spectrum receivers in general— are annotated in the shaded boxes and linked to the appropriate receiver blocks.

## Chapter 2 A Review of Spread Spectrum Systems and Techniques

---

Spread spectrum systems have been employed for communications and high resolution ranging applications for nearly half a century. The high cost and complexity associated with the transmitters and especially the receivers of such systems have, until recently, limited the application of spread spectrum systems, such that widespread use was observed only in the areas of military and satellite communications [1-3]. Recent advances in high density semiconductor fabrication technologies now permit the complex circuits required by spread spectrum transmitters and receivers to be implemented on a single integrated circuit (*e.g.*, [4]) in a cost-effective manner. Partly in response to these advances, spread spectrum has now become viable for a number of commercial applications [5-8].

The bulk of this dissertation is closely connected to the application of spread spectrum communications. A brief description and review of the basic issues associated with the spread spectrum concept are given in the remainder of this chapter. In section 2.1, spread spectrum is defined, and a brief motivation for its use is given. Several of the modulation techniques used to achieve spectrum spreading

are described in section 2.2. Lastly, in section 2.3, a list of the potential benefits of spectrum spreading is presented and expounded upon. The information in this chapter is intended to serve as background material only and does not represent original contributions made by the author.

## 2.1 Spread Spectrum: The Concept

In order for a signal to be considered as a member of the spread spectrum family, the transmitted bandwidth of the signal must be large relative to the information rate of the data being transmitted [1,2,9]. With this qualifier alone, large deviation FM, where  $\beta = \Delta f_{carrier} / f_{modulation}$  is large relative to unity, might be considered as a spread spectrum technique. Typically, however, in order for a signal to be considered as a member of the spread spectrum family, an additional qualifier is appended which requires that the transmitted bandwidth be determined by a process not directly related to the transmitted information [1]. This second requirement disqualifies large deviation FM.

A manipulation of the channel capacity relation originally given by Shannon [10,11] provides insight into the benefits that may be derived from a spread spectrum system (this derivation is adapted from [1]). In the presence of additive white gaussian noise, the channel capacity can be written as

$$C = W \log_2 \left( 1 + \frac{S}{N} \right), \quad (2.1)$$

where  $C$  = the channel information capacity in bits per second,

$W$  = the signal bandwidth in hertz,

$N$  = the noise power,

and  $S$  = the signal power.

Changing bases and rearranging terms gives

$$\frac{C}{W} \cong 1.44 \log_e \left( 1 + \frac{S}{N} \right), \quad (2.2)$$

and for small signal-to-noise ratios,  $S / N \ll 1$ , a Taylor series approximation of (2.2) yields

$$\frac{C}{W} \cong 1.44 \frac{S}{N}, \quad (2.3a)$$

$$\text{or } C \cong 1.44 \frac{S}{N} W. \quad (2.3b)$$

From (2.3b), it is observed that an increase in the transmission bandwidth,  $W$ , leads to a corresponding increase in the information-carrying capacity of the channel. C. Alternatively, it is possible to compensate for an arbitrarily poor received signal-to-noise ratio (SNR) through the choice of an appropriately wide transmission bandwidth. These concepts provide the basis for understanding the benefits of spectrum spreading. A more detailed look at a number of the consequential benefits

of spread spectrum, as embodied in (2.3b), is given in section 2.3.

## 2.2 Methods of Spectrum Spreading and De-Spreading

The history of the methods and applications of spread spectrum systems are traced in chapter 2 of [2]. Most of the spreading techniques that are in use today and that have been proposed for use in future systems can be grouped into one of three categories [1]:

1. Modulation of a carrier by a digital code sequence whose chip rate is much higher than the information signal bandwidth. Such systems are called "direct sequence" modulated systems.
2. Carrier frequency shifting in discrete increments in a pattern dictated by a code sequence. These are called "frequency hoppers." The transmitter jumps from frequency to frequency within some predetermined set; the order of frequency usage is determined by a code sequence.
3. Pulsed-FM or "chirp" modulation in which a carrier is swept over a wide band during a given pulse interval.<sup>1</sup>

Each of these methods are discussed briefly below.

For future reference, the term *chip* is used in the context of spread spectrum systems to denote a single symbol of the spreading waveform. A single spreading waveform is made up of multiple chips. Within direct sequence systems, a chip typically belongs to the binary set {0,1}, whereas in frequency-hop systems, the term *chip* is sometimes used to describe a single *hop* of the output carrier frequency. The

---

<sup>1</sup> Quoted from [1], pages 6-7.

term *chip* is introduced to permit discrimination between the symbols of the spreading codes and the *bits* of the information data.

### 2.2.1 Direct Sequence Spread Spectrum Systems

The binary-valued spreading waveforms generally employed in direct sequence spread spectrum (DS-SS) systems are designed to have noise-like properties. The waveforms used in most practical systems, however, are periodic and, therefore, are called *pseudonoise* (PN) or *pseudorandom* codes. These codes typically have a period equal to or greater than the period of a single data bit of the system in which they are employed. It is desirable that these PN codes have low sidelobes in their auto-correlation functions and/or low peak values in the cross-correlation with some given set or family of codes. The efficient generation of PN codes that have these and other desirable properties has been widely studied (see [1,2,9,12-18] and the references therein). Codes can be generated quickly and compactly through the use of linear feedback shift registers (*e.g.*, [1, 12]).

An illustration of the key features of a DS-SS system is given in Figure 2.1. In this figure, the spreading sequence has a chip rate that is sixteen times greater than the information data rate. When binary-valued waveforms are employed (as is shown in the figure), the modulation operation takes place through a simple modulo-two addition of the information data and the spreading sequence (note that this is equivalent to the multiplication of the input data stream and the spreading sequence if

the binary values of 0 and 1 are interpreted as symbols that represent the numbers +1 and -1, respectively).

The  $(\sin(x) / x)^2$  envelope of the magnitude of the power spectrum of the information data and the DS-modulated data is shown in Figure 2.1b. In practice, the transmitted bandwidth of a DS-SS system must be truncated to prevent out-of-band interference. The actual transmitted bandwidth is usually some value between the chip rate (*i.e.*, [8]),  $R_{pn}$ , and twice the chip rate [1],  $2 \times R_{pn}$ , with the former being the Nyquist-rate-limited value and the latter being the bandwidth that contains the entire main lobe of the  $(\sin(x) / x)^2$  envelope and roughly 90% of the total power contained in the entire  $(\sin(x) / x)^2$  power spectrum.

The major blocks that are required for a transmitter and receiver in a synchronous DS-SS system are shown in Figure 2.1c. The receiver must maintain precise synchronization with the incoming DS-SS signal. Because most PN codes are intentionally designed to have low auto-correlation sidelobes, slippage of synchronization by a single chip of the PN code will generally render the output of the correlator meaningless [1,5,18].

In asynchronous systems or in environments where synchronization is difficult to establish, a matched filter may be used in place of the correlator [19]. The integrate-and-dump style correlator (also known as a *serial matched filter*) shown in Figure 2.1c produces a single point in the cross-correlation between the received signal and the locally stored replica of the spreading waveform. The output of the (parallel) matched filter shown in Figure 2.2 is the entire discrete-time cross-

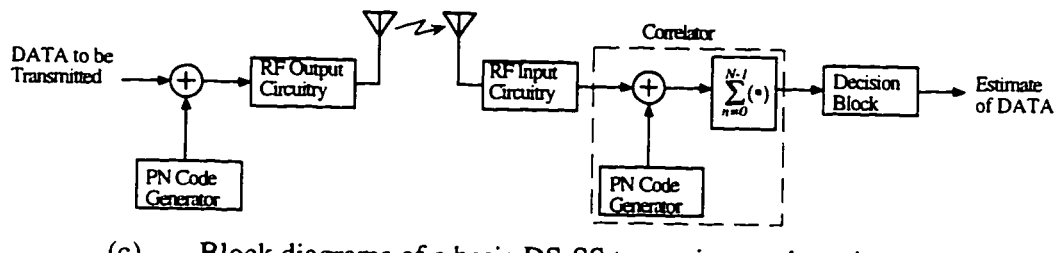
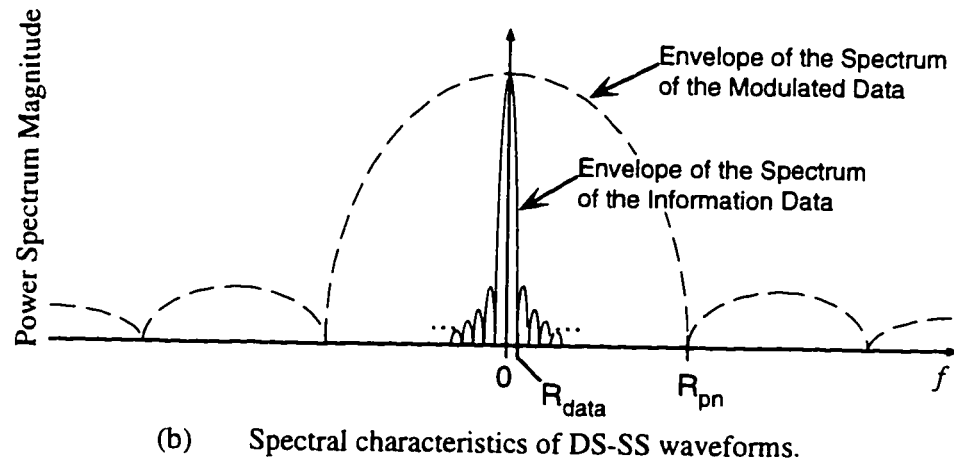
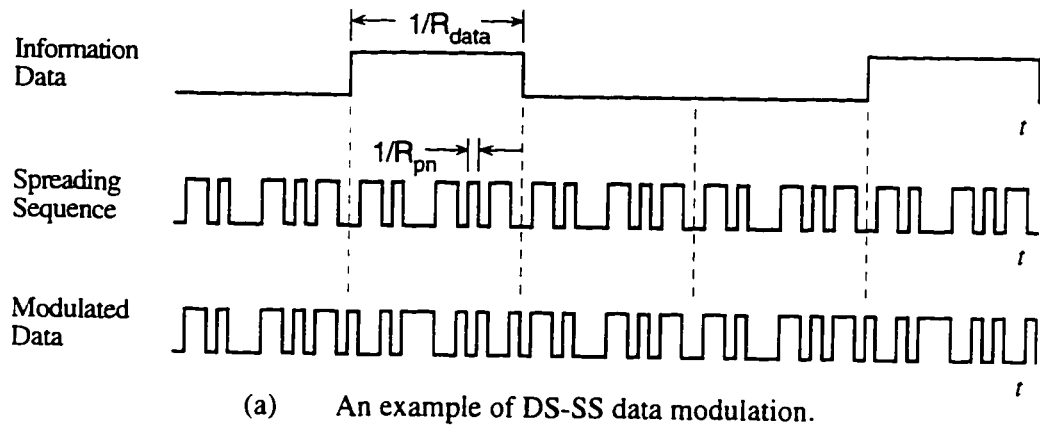
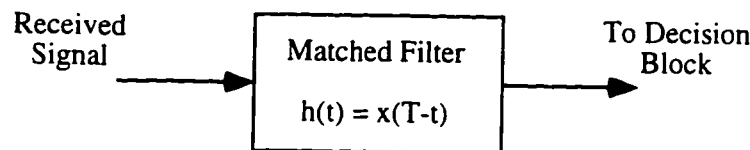
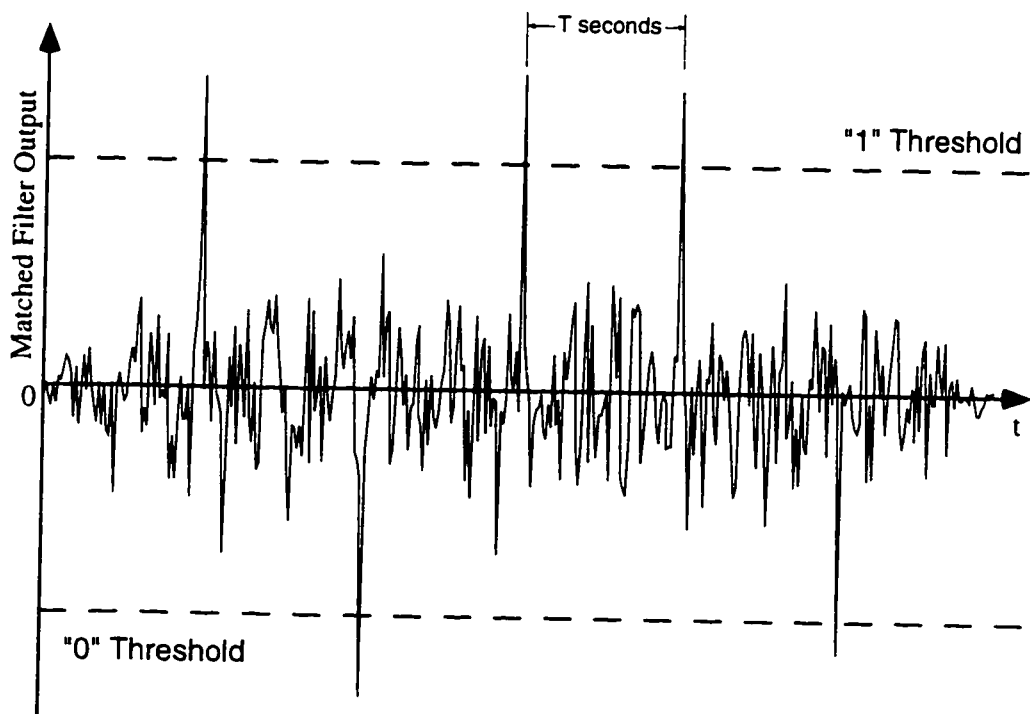


**Figure 2.1** Shown in the figure are some of the key features of a DS-SS system. Spreading by the PN code is demonstrated in (a), the spectral characteristics of the DS-SS waveform are shown in (b), and block diagrams of a transmitter and synchronous receiver are shown in (c).



(a) The matched filter block that is shown here can be used in place of the correlator block in Figure 2.1a. The impulse response,  $h(t)$ , of the causal matched filter is a time-reversed replica of the original spreading sequence,  $x(t)$ .



(b) Matched filter output for an input data sequence of 10110. The spreading sequence has 64 PN chips per data bit, a time length of  $T$  seconds, and the received SNR is zero dB. Data recovery can be achieved by a simple threshold operation.

**Figure 2.2** A matched filter block, which is used in asynchronous spread spectrum receivers in place of the correlator block of Figure 2.1c, is shown in (a). In (b) are given a sample matched filter output and an illustration of how data recovery can be achieved by thresholding the matched filter output.

correlation between the received signal and the locally stored replica of the spreading waveform. If synchronization is not achieved, the correlator will not sample the correlation function at the peak value, and the output of the decision block will be of no use in determining an estimate of the transmitted data. The matched filter output, however, will always contain the data-related peak, making matched filter processing much more powerful than processing by a single correlator.

### 2.2.2 Frequency-Hopping Spread Spectrum Systems

As the name suggests, frequency-hopping spread spectrum (FH-SS) systems achieve spectrum spreading by directing the carrier frequency to *hop* from frequency to frequency according to some predetermined pattern. A sample hopping pattern is shown in Figure 2.3a. The frequency axis on the hopping pattern in Figure 2.3a is discretized, with the corresponding actual frequencies belonging to the set

$$\left\{ f_i \left| f_i = f_{carrier} + \alpha_i \frac{W}{N_{hops} - 1} \right. \right\}, \quad 1 \leq i \leq p - 1, \quad (2.4)$$

where  $\alpha_i$  = the *placement operator*,

$W$  = the approximate bandwidth of the FH-SS system,

$f_{carrier}$  = the system carrier frequency, and

$N_{hops}$  = the number of discrete frequencies that the system occupies within  $W$ .

Each of the frequency hops is generally assumed to be sustained for a duration

$$T_i - T_{i-1} = \frac{T}{N_{hops}}, \quad (2.5)$$

where  $T_i$  marks the beginning of the  $i^{th}$  frequency hop,

$T$  = the time-length of the entire FH code, and

$N_{hops}$  = as defined in (2.4).

A waveform represented by the hop pattern in Figure 2.3a is shown in Figure 2.3b.

The shape of the spectrum of the FH code shown in Figure 2.3a is depicted in Figure 2.3c and 2.3d for two different values of  $T$ .

The search for families of hopping patterns that possess certain desirable qualities, similar to those described above for DS-SS codes, is a rich area of research (e.g., [20-26]) and has resulted in the discovery of a number of code families useful for communications and ranging applications. The hop pattern shown in Figure 2.3a, for example, is from the family of linear congruence FH codes [21], where the placement operator for this family is described by the following relation:

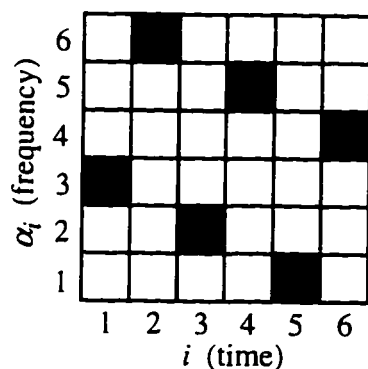
$$\alpha_i = (a \cdot i + b) \bmod p, \quad (2.5)$$

where  $a$  = an integer in the set {1,2,...,p-1},

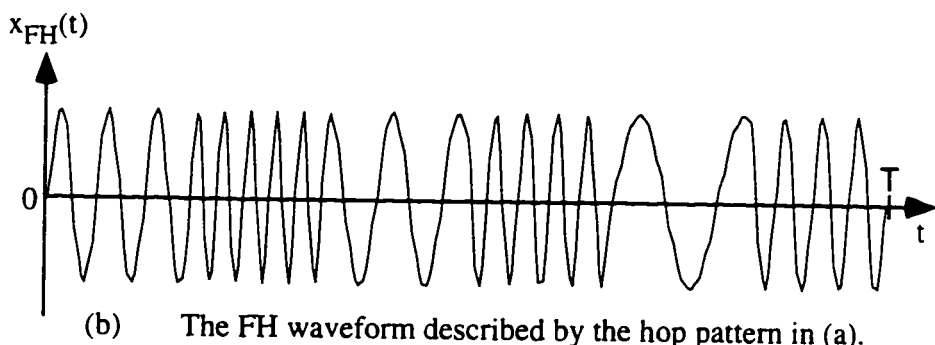
$b$  = an additive constant that is the same for all of the codes in the family, and the arithmetic is performed modulo- $p$ , where  $p$  is prime.

In the example of Figure 2.3a,  $a = 3$ ,  $b = 0$ , and  $p = 7$ .

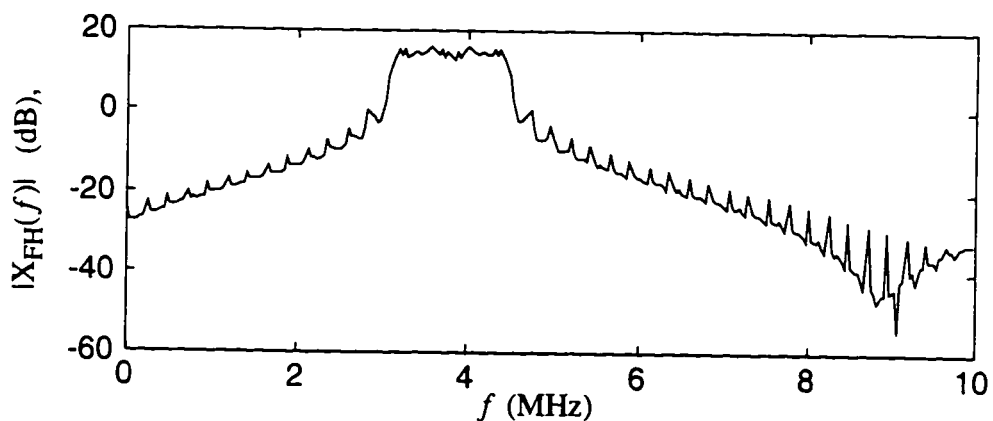
A number of methods exist for impressing the data on the FH code, or vice



(a) Hop pattern for a linear congruence FH code with  $a = 3$ ,  $b = 0$ , and  $p = 7$ .

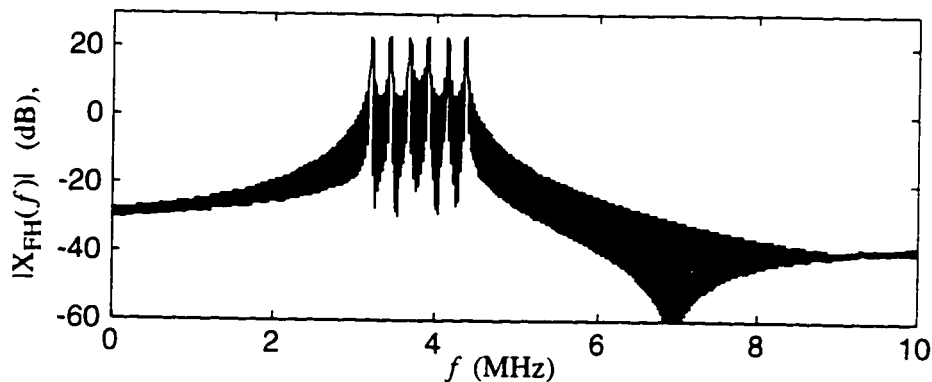


(b) The FH waveform described by the hop pattern in (a).

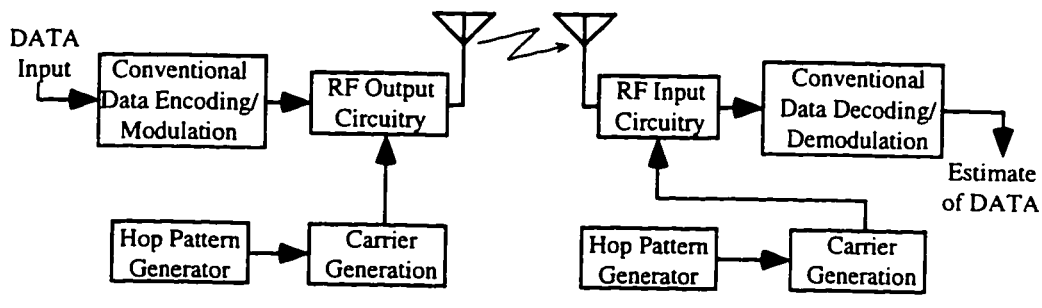


(c) Spectrum for the FH waveform described by the hop pattern in (a). Time-length and bandwidth were chosen to produce a nearly flat spectrum.

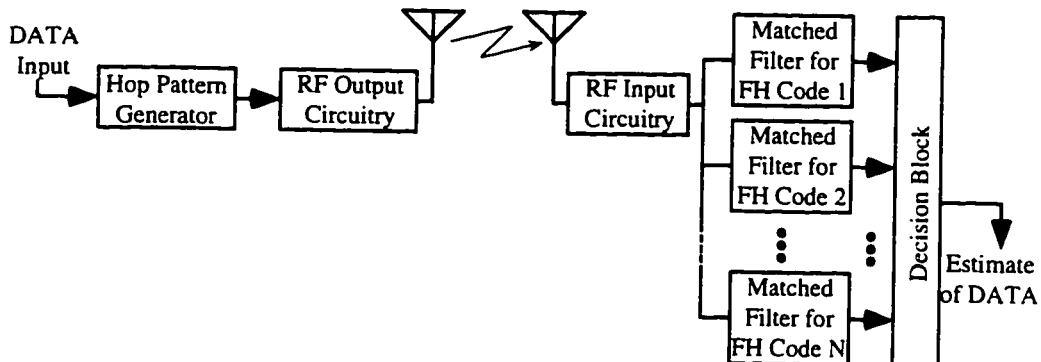
Figure 2.3 is continued on the following page.



(d) Spectrum for the FH waveform described by the hop pattern in (a), shown here with a TW product eight times greater than that used for (c).



(e) Simplified transmitter and receiver for a slow FH-SS system.



(f) Simplified transmitter and receiver for a fast FH-SS system.

**Figure 2.3** Key features of a FH-SS system. A hop pattern is shown in (a), and a corresponding waveform is shown in (b). The spectrum of the waveform is shown in (c) and (d) for two different values of TW. Transmitter and receiver structures for a slow FH-SS system and a fast FH-SS system are shown in (e) and (f), respectively.

versa. In *slow FH* systems [2], the hopping rate is slower than the data rate, and the transmitted waveform may be a conventional amplitude-, frequency-, phase-modulated, or even a DS-SS signal with a carrier that hops from frequency to frequency. Once synchronization is achieved in the receivers for such systems, the downconversion operation incorporates the hops of the placement operator, allowing the data demodulation to be done in the conventional manner (see Figure 2.3e).

Alternatively, there also exist *fast FH* systems [2], in which the hopping rate is faster than the information data rate. In these systems, the hopping patterns themselves may represent the data symbols to be transmitted. For example, separate hopping patterns may be chosen to transmit a *mark* and a *space*, respectively. Depending on the degree of synchronization that is inherent in the system, a correlator or matched filter similar to those described above in section 2.2.1 may be incorporated into a fast FH receiver (see Figure 2.3f).

### 2.2.3 Pulsed FM (Chirp) Spread Spectrum Systems

Pulsed FM, or *chirp*, spread spectrum systems were first used in World War II as a means to increase radar resolution for a given fixed transmit power [2]. The most common type of waveform used in pulsed FM spread spectrum systems belongs to the family of the linear FM sweep [1]. These signals are described by the equation,

$$x(t) = A \cdot \cos\left(\omega_1 t + \frac{t^2}{2T}(\omega_2 - \omega_1)\right), \quad (2.7)$$

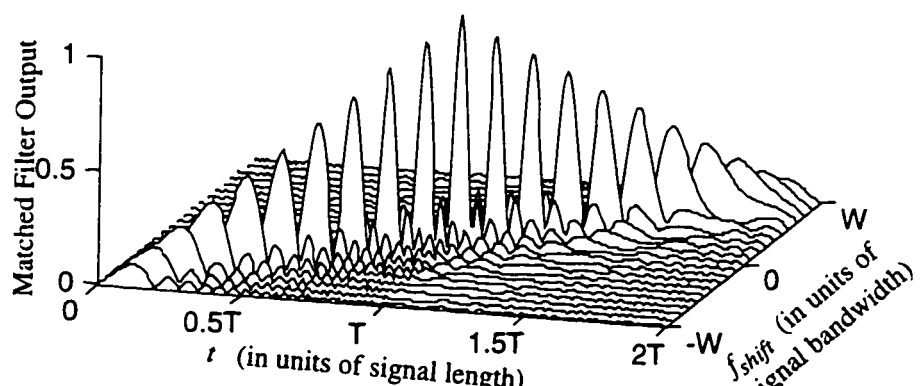
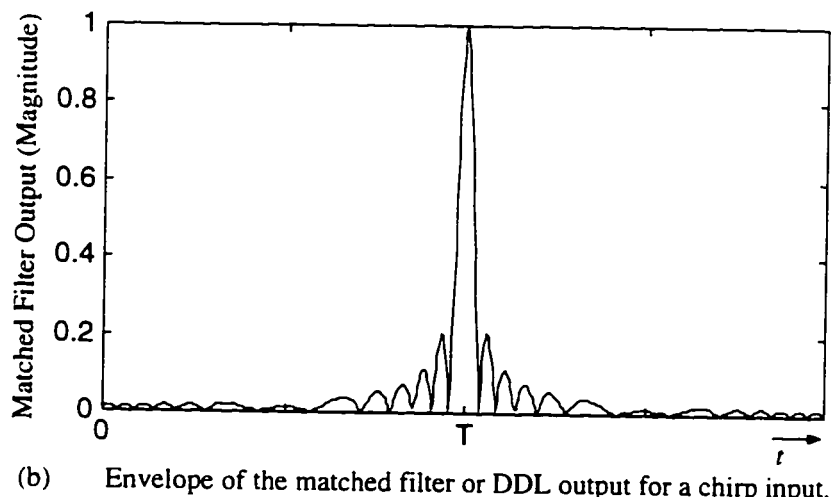
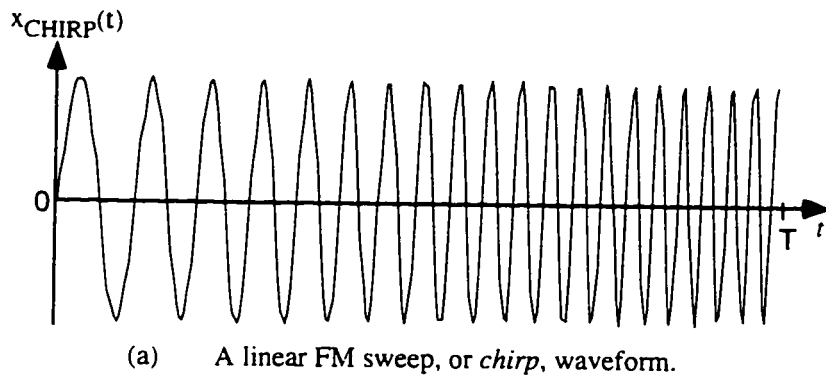
where  $A$  = the amplitude,

$T$  = the time duration of the pulse, and

$\omega_1$  and  $\omega_2$  = the starting and ending frequencies, respectively, of the chirp.

Receivers of chirp systems may incorporate a dispersive delay line (DDL), which has the effect of delaying the frequencies near  $\omega_1$  more than the frequencies near  $\omega_2$ . The received signal energy can in this way be compressed into a narrow pulse at the DDL output, leading to greater detection capabilities over waveforms that do not experience such pulse compression (see Figure 2.4). Alternatively, receivers in chirp systems may employ a tapped delay line matched filter, as described in 2.2.1, in place of the DDL to achieve the same pulse compression.

In a communications environment, chirp spread spectrum systems offer some features that are not available from either DS- or FH-SS systems. Most notably, chirp waveforms are especially tolerant to Doppler shifts and/or local oscillator drift phenomena [27-29]. This property can lead to synchronization and detection in environments where DS- or FH-SS systems fail. Unfortunately, the number of unique chirp waveforms that can coexist in the same bandwidth at the same time while still maintaining the beneficial properties outlined above is small relative to the DS and FH family sizes. This characteristic is probably responsible for keeping chirp spread spectrum systems from widespread use in multiple-access communications.



(c) The matched filter output is shown along the x-axis for varying degrees of local oscillator drift or Doppler shift, as characterized by  $f_{shift}$  on the y-axis.

**Figure 2.4** A chirp waveform is shown in (a), and the output of a chirp matched filter output is shown in (b). An illustration of the detection properties of chirp systems in a Doppler environment or in a system that contains local oscillator drift phenomena is given in (c).

## 2.3 Some Benefits of Spread Spectrum Systems

The positive aspects of spectrum spreading go beyond the potential capacity gains outlined in (2.1) through (2.3). These other benefits were first effectively applied to military communications [1,2] and have recently been the subject of considerable interest for consumer applications [5-8,30-32]. In the following, an introductory description of some of these benefits is provided.

### 2.3.1 Anti-Jamming Properties

In the military, reliable means of communication are crucial. While wireless communication during peacetime may require a system that is able to cope with geographic and atmospheric anomalies, wireless communications during war must, in addition, be robust against deliberate interference from a hostile source. By radiating high-power RF signals in the appropriate frequency band, an opposing force may attempt to impede the wireless communications of its opponent (see chapter 2 of [2] or [33] for a description of how this tactic was successfully applied by Allied forces in the Battle of the Bulge in World War II). Spread spectrum systems have an inherent ability to reject this hostile interference.

The utility of spread spectrum in an interference environment can be simply understood by again referring to (2.3). By considering the interference as an additional noise component, it is readily visible from (2.3) that capacity gains can be

achieved in the midst of interference by a further increase in the signal bandwidth. The concept of a *jamming margin* is commonly used [1,2] to describe the advantage of spectrum spreading under hostile circumstances. The jamming margin can be described by [1]

$$M_j = TW - (L_{sys} + SNR_{reqd}), \quad (2.8)$$

where  $M_j$  = the jamming margin in dB,

$TW$  = the product of the time-length  $T$  and RF bandwidth  $W$  in dB,

$L_{sys}$  = the system implementation loss in dB, and

$SNR_{reqd}$  = the receiver output SNR in dB required for recovery of the encoded data.

The quantity  $TW$  is also commonly referred to as the *processing gain* of the system [1]. A system that has a processing gain of 20 dB, system implementation losses of 3 dB, and that requires a minimum output SNR of 6 dB will have a jamming margin of 11 dB. That is, the system would not be expected to operate with interference 11 dB or greater than the desired signal [1]. If the system is expected to routinely operate among interference levels exceeding its jamming margin, the system may be redesigned and the jamming margin increased via additional spectrum spreading.

### 2.3.2 High-Resolution Ranging (Radar) Applications

Ranging applications such as radar are probably the best known use of spread spectrum systems. Ranging is performed by transmitting a known signal and recording the times that each echo is received back at the transmitting station. These times are proportional to the two-way round-trip distance between the transmitter and the reflecting surfaces (targets) responsible for returning the echoes.

The time resolution of a ranging system that uses matched filter processing is approximately equal to the inverse of the RF bandwidth,  $W$ , of the transmitted signal [1,28,29,34]. The detection of the received echoes and the interference rejection properties of the ranging system are related to the  $TW$  product in much the same way as was described above in 2.3.1 for the jamming margin.

### 2.3.3 Covertness and Low-Power Signal Transmission

Spread spectrum offers the military community not only the ability to withstand interference from a hostile source, but also the ability to transmit data in a manner that the enemy is unable to detect. The processing gain inherent in spread spectrum communication systems may permit signal transmission at power levels that are a fraction of the noise power of the channel. Such signals, buried in noise, are nearly impossible to detect without prior knowledge of the exact code that is being employed. By transmitting in this fashion, source localization information is

not yielded to the enemy [1, 2].

The ability to transmit and recover signals at power levels below the level of the channel noise also has utility in consumer applications. Conventional modulation methods do not experience the significant processing gain available from spread spectrum systems. Thus, if an output signal-to-interference ratio of 10 dB is required, the conventional system must transmit at power levels at least 10 dB above the interference level, while a spread spectrum system with a processing gain of 20 dB can transmit at power level roughly 100 times smaller than the conventional system. For applications such as cellular or cordless telephony, the decrease in transmitted power levels afforded by spread spectrum can translate into a smaller power drain on the battery of the portable transmitter, increasing the talk time and/or decreasing the required size of the terminal [35].

### 2.3.4 Cryptographic Incorporation

Most cellular and cordless phone users are unaware that virtually anyone with the desire to do so can listen in on conventional analog wireless phone calls. Not only is voice conversation available to these eavesdroppers, but also available are any credit card numbers, voice mail PINs, bank account numbers, or any other kind of number that cell phone users might type into their keypad. Of principle concern to the service providers in the cellular telecommunications industry is the fact that the ID numbers that mark valid cell phone customers are also currently transmitted over the

open air in a way that can be detected by these same eavesdroppers. These ID numbers can be used to *clone* a cell phone, allowing someone apart from the true owner of the ID numbers to make phone calls (typically overseas and other long distance calls) while charging the bill to the owner's account. The cellular industry has reported losses from this type of fraud to be on the order of one million dollars per day [36].

There is in spread spectrum systems a certain level of protection against such fraud. As long as the spreading waveform is known only by the true transmitter (say, a valid cell phone user) and the true receiver (say, the cell phone base station), the signal that appears in the open air should be difficult to decipher by eavesdroppers. If digital data is being transmitted, further encryption can take place before signal spreading, leading to even more protection against fraud [8].

### 2.3.5 Multipath Mitigation and Exploitation

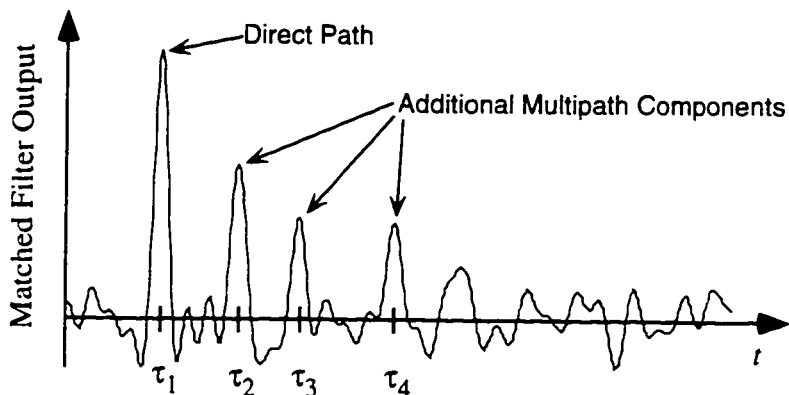
When transmitter energy can arrive at the receiver via more than one path, the potential for multipath-induced *fading* exists. This fading is the result of the destructive interference that can occur between sinusoids with nominally similar frequencies but with phase offsets near 180 degrees. For conventional modulation methods in high multipath environments such as urban centers, fading effects can severely degrade the quality of a data link, leading to fades in excess of 30 dB [37].

The first generation analog cellular phones combated fading largely by increasing

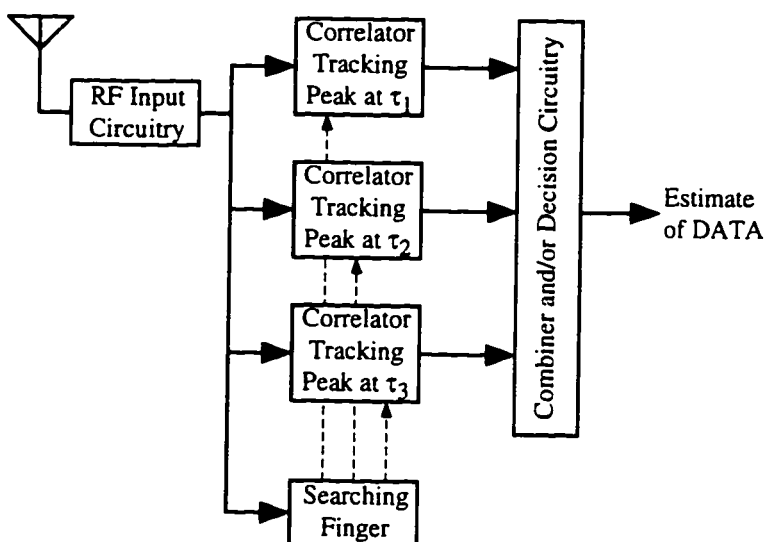
transmit power levels.

Spread spectrum offers immunity to multipath by virtue of the fact that the signal energy is spread over a wider frequency range than with conventional systems, offering a form of frequency diversity. A fade that causes a 20 dB drop in the received power levels for spectral components in a 50 kHz band around the carrier frequency may completely disrupt communications in a 30 kHz FM system, while the same fade will cause a spread spectrum system with a bandwidth of 1 MHz to experience a loss in received signal power of less than five percent.

Communication links based on spread spectrum techniques have the potential to turn multipath from a disadvantage into an advantage. Individual peaks due to the individual received echoes in a multipath environment may be resolved at the correlator or matched filter output if the distance between the first received signal component and the ensuing multipath echoes is greater than  $c / W$ , where  $c$  is the speed of propagation in the channel, and  $W$  is the transmitted RF bandwidth (see Figure 2.5). The secondary peaks in the matched filter output contain signal energy that would not be present if the channel were free from multipath effects. After locating these multipath branches, a new form of diversity can be exploited whereby signal energy from multiple echoes is combined in a way that makes the entire receiver system more robust against certain types of fading [31,38-40].



(a) Matched filter output showing the presence of four strong paths.



(b) A three-fingered *rake receiver*.

**Figure 2.5** In (a) is shown a matched filter output from a system that is operating in the presence of four strong multipath components. The three-fingered rake receiver that is shown in (b) combines the energy from the three strongest paths, while the searching finger looks for new strong paths.

### 2.3.6 Multiple-Access Overlay

It is possible to design families of FH- or DS-SS codes where cross-correlations between any two members of a given family are small [13-15,17,18,21, 25]. A correlator or matched filter that has been programmed to detect a particular code in a family can treat other members of the family as if they were part of the channel noise. This property enables the use of *code-division multiple-access*, or *CDMA*, whereby a number of spread spectrum waveforms can coexist in the same bandwidth at the same time. The different codes can be used to transmit different messages to the same user, or can permit the use of a given swath of spectrum by multiple users.

CDMA is useful in military applications where, for instance, a target is illuminated by multiple radar or sonar sources [26]. If all radars in this scenario were to employ the same probing signal, the receivers may not be able to distinguish a received echo from a received line-of-sight transmission emanating from one of the other radar sources. This ambiguity can be eliminated by requiring each radar source to transmit a different CDMA waveform as a probing signal.

CDMA can also be profitably applied to commercial applications. In cellular telephony, for example, different cells may employ different spreading waveforms (or different time-offsets of the same, well-designed waveform [8]), allowing adjacent cells to utilize the same spectral resources simultaneously. This property helps the proposed CDMA cellular standard to achieve a frequency reuse factor close

to unity [31,41], while the first generation analog cellular system has a frequency reuse factor near 1/7 [6,31,37] (that is, a given frequency channel cannot be used more than once in seven cells).

The CDMA property of spread spectrum systems also permits the same spectrum to be used by diverse applications. In some of the so-called ISM (industrial, scientific, and medical) frequency bands, CDMA methods have permitted cordless telephone, in-plant wireless local-area-networks, and other systems to coexist in the same, nearly unrestricted, unlicensed RF spectrum [5,7].

# Chapter 3 Parameter Estimation of Specular Multipath Channels in the Presence of Doppler

---

High resolution multipath parameter estimates can be obtained through various deconvolution procedures, all of which —in the limit— rely on some form of inverse filtering. Though deconvolution in a multipath environment free from Doppler is well understood and well documented, this is not true for the case where motion of the multipath components relative to the receiver imposes a Doppler shift on the transmitted probing signal. This chapter describes the effects of Doppler on a broad class of deconvolution methods by studying the effects of Doppler on the output of an inverse filter. It is shown that, in the presence of Doppler, the deconvolution outputs are comprised chiefly of two signal-related functions, one of which may be designed in such a way as to be free from the range-Doppler coupling effects inherent in correlation processing. Knowledge of these two functions provides insight into the signal design issues relevant to deconvolution-based multipath parameter estimation systems and is useful in designing appropriate constraints and post-processing algorithms which may lead to an accurate extraction

of the Doppler and delay parameters of the multipath channel. These results are applied to two known deconvolution methods: those being the method of projection onto convex sets (POCS) and the method of least squares (LS).

### 3.1 Introduction

A specular multipath condition exists within a communications channel whenever a single transmitted signal has the potential of arriving at the receiver via a number of distinct, unequal length paths. In such an environment, reflective surfaces of various size and location redirect energy from the transmitter to the receiver. The result of this process is a received signal that is the sum of a number of delayed and amplitude-weighted versions of the original transmitted waveform. Furthermore, if any of the reflecting surfaces have a non-zero radial velocity component relative to the receiver, a Doppler shift (or spread) will be imposed on the corresponding received multipath component (*e.g.*, Figure 3.1). Thus, assuming a Doppler shift, the form of the received signal,  $y(t)$ , in a multipath environment is given by

$$y(t) = \sum_{k=1}^{N_k} \alpha_k x(t - \tau_k) e^{j\omega_{D_k} t} + n(t) , \quad (3.1)$$

where  $\alpha_k$ ,  $\tau_k$ , and  $\omega_{D_k}$  are the amplitude, delay, and Doppler shift of the  $k^{\text{th}}$  multipath component,  $N_k$  is the number of received specular reflections,  $x(t)$  is the transmitted signal, and  $n(t)$  is the channel noise. In practice, the set of the parameters

$\{(\alpha_k, \tau_k, \omega_{D_k}), 1 \leq k \leq N_k\}$  are the unknowns that are to be estimated. In (3.1) the velocity effects of the multipath components are modeled as a frequency shift. This is the so-called *narrowband approximation* [28] and is sufficiently accurate for most wireless and radar applications, but less accurate for sonar and other acoustic systems. The narrowband approximation relates the velocity of a multipath component to the resulting Doppler shift via

$$\omega_D \equiv \frac{2v}{c} \omega_{carrier} \quad (3.2a)$$

and is applicable to systems where

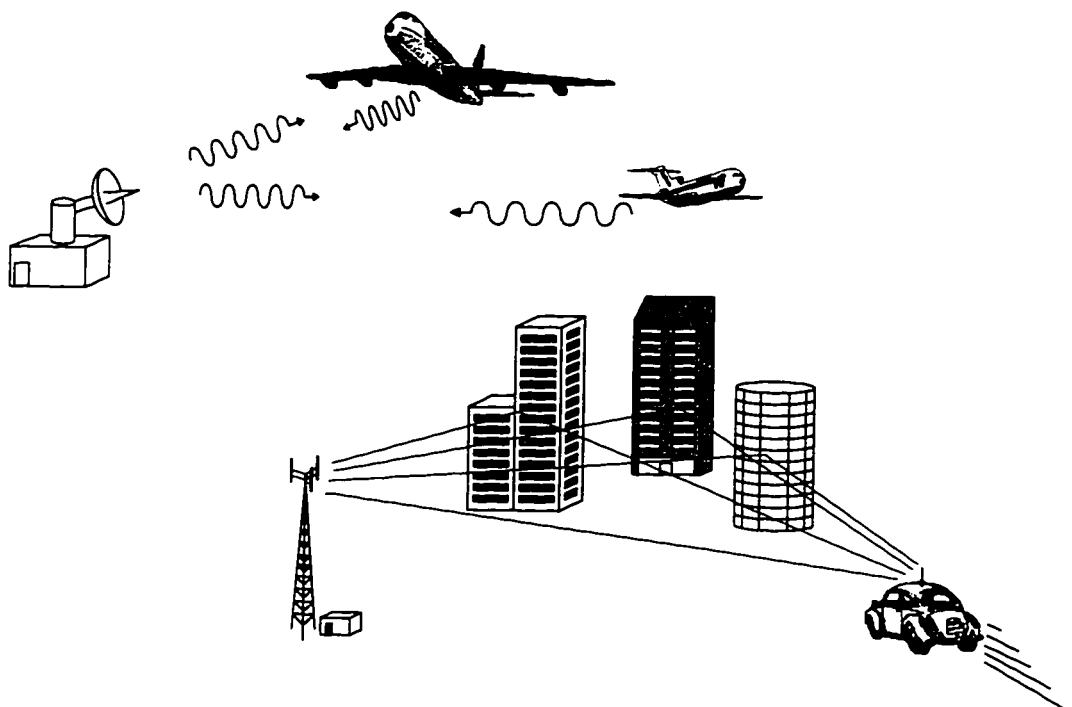


Figure 3.1 Sources of Doppler multipath.

$$\frac{2v}{c} \ll \frac{1}{BW \cdot T}, \quad (3.2b)$$

where  $v$  is the relative radial velocity,  $c$ , is the speed of propagation in the medium.  $BW$  is the signal bandwidth in Hz,  $T$  is the signal time-length in seconds, and  $\omega_{carrier}$  is the carrier frequency of the transmitted signal. Throughout the following analyses, the narrowband assumption is assumed to hold.

In some systems, such as radar or sonar applications, the multipath parameters themselves —related to cross-section, distance, number, and speed of the potential targets within scanning range— may be the desired end result of the estimation procedure. In other systems, such as mobile cellular radio, the estimated parameters may be used as part of a mechanism to improve received signal quality through intelligently combining the signal energy from multiple reflections by means of a *rake receiver* or a similar device [4,6,31,39].

Correlation processing, to be discussed in more detail in the following chapter, may sometimes be an adequate method of delay and Doppler estimation. Within such a scheme, a spread spectrum pulse compression type waveform, such as a linear FM chirp or a fast frequency-hop code [42] may be used as a probing signal. The receiver is then simply a matched filter, or a bank of incrementally Doppler-shifted matched filters. The receiver output, from which the parameters are to be estimated, is a partial view of the cross-ambiguity function [28,29,34] between the received signal and the locally stored reference signal. The delay estimation resolution of such an approach is limited to approximately the inverse of the signal

bandwidth [28,29,34].

In addition to correlation processing, more sophisticated methods of parameter estimation exist. These methods include cepstrum analysis [43], deconvolution procedures, and eigenstructure methods [44-46]. The deconvolution procedures can estimate delays to within one sample period, and the eigenstructure methods —at an increased computational cost— can resolve delays even smaller than a single sample period [44]. Thus, the choice of which class of procedures to implement in a given system is determined by the required resolution and the allowable computational burden of the procedure. The remainder of this chapter will address the issues of multipath parameter estimation relevant to the case where the estimation technique belongs to the family of deconvolution methods.

Deconvolution methods, in general, are means of constrained inverse filtering. In the zero-Doppler case, inverse filtering appears to be a reasonable approach. For example, in the absence of noise and Doppler, if the signal  $x(t)$  is transmitted through a multipath channel with an unknown linear response,  $c(t)$ , then the channel response can be estimated from the received signal and *a priori* knowledge of the transmitted signal via

$$y(t) = x(t) \otimes c(t) \quad (3.3a)$$

$$\Rightarrow c(t) = FT^{-1} \left\{ \frac{Y(\omega)}{X(\omega)} \right\} = FT^{-1} \left\{ \sum_{k=1}^{N_t} \frac{\alpha_k X(\omega) e^{j\omega\tau_k}}{X(\omega)} \right\} = \sum_{k=1}^{N_t} \alpha_k \delta(t - \tau_k), \quad (3.3b)$$

where  $\otimes$  represents the convolution operation, and  $Y(\omega)$  and  $X(\omega)$  are the Fourier

transforms (FTs) of the received and transmitted signals, respectively. In the absence of noise and Doppler, the channel estimate produced by inverse filtering is exact. The adverse effects of inverse filtering when noise is present, including the *ill-conditioned* problem whereby noise in the numerator of (3.3b) is large compared to the signal components in the denominator, are well-known and well-documented [47-55]. These adverse effects are, in fact, what motivated the invention of the constrained inverse filtering methods used in all practical deconvolution systems. These methods are *constrained* in the sense that they disallow output values that lie outside some predefined set and/or in the sense that the inverse operator is never completely formed but only iteratively approximated.

The deconvolution methods do not, however, address the issue of what the form of the output of an inverse filter (IF) will be when the input is a Doppler shifted version of the stored reference signal. Indeed, there is no immediately clear reason why an IF or deconvolution method should work at all within a Doppler multipath environment. Consider again the estimation problem in (3.3), this time allowing for Doppler effects:

$$c(t) = \mathcal{FT}^{-1} \left\{ \frac{Y(\omega)}{X(\omega)} \right\} = \mathcal{FT}^{-1} \left\{ \sum_{k=1}^{N_t} \frac{\alpha_k X(\omega - \omega_{D_k}) e^{j\omega t_k}}{X(\omega)} \right\} \quad (3.4)$$

There is no direct time-domain representation for the ratios of Fourier transforms expressed in (3.4). Yet, it has been shown in the past [51,55] that deconvolution methods are able to resolve both accurate time delay and Doppler shift values.

It has been noted [51,52] that the outputs of a bank of matched filters could be treated as a 2-D image, where, for example, the time response of the matched filters is displayed parallel to the x-axis and the response due to the parametrized Doppler shift is displayed parallel to the y-axis (as is shown in Figure 3.8a). In such treatments, the 2-D image formed by the matched filter outputs is observed to be a 2-D convolution between the auto-ambiguity function of the transmitted signal and the 2-D parametrized channel impulse response. The suggestion is made that an estimate of the channel could be obtained by deconvolving the 2-D matched filter output with the auto-ambiguity function of the transmitted signal, *i.e.*, "deblurring" the image.

However, there exists a difficulty in establishing this analogy with image restoration. Hardware limitations dictate that the bank of matched filters cover only a small range of Doppler shifts, and the information along this range of the Doppler axis is insufficient for a robust estimation of the Doppler/delay parameters, since there are large parts of the "image" along the Doppler axis that are not included in the narrow window yielded by the ensemble of matched filter outputs. Along the time axis, however, large enough segments of the auto-ambiguity function are available, which suggests a solution that is a compromise: a set of 1-D deconvolutions in time can be performed for each accommodated Doppler shift (see Figure 3.2). It is this last procedure that is the topic of discussion for the remainder of this chapter.

The main contribution of this chapter is the derivation of the form of the 1-D IF output in a Doppler multipath environment. This derivation is given in section 3.2, where it is also shown that the output of the IF can be characterized by two

signal-related functions, one of which is —for some signals of interest— free from the range-Doppler coupling effects inherent in correlation processing techniques. In section 3.3, two different examples of existing deconvolution methods are described and employed in the delay-Doppler estimation problem. The estimation properties of these two deconvolution methods are shown to profit from and be consistent with the analyses of section 3.2. In section 3.4, the relevance and significance of the results from 3.2 and 3.3 as they pertain to specular multipath parameter estimation in the presence of Doppler are discussed and summarized.

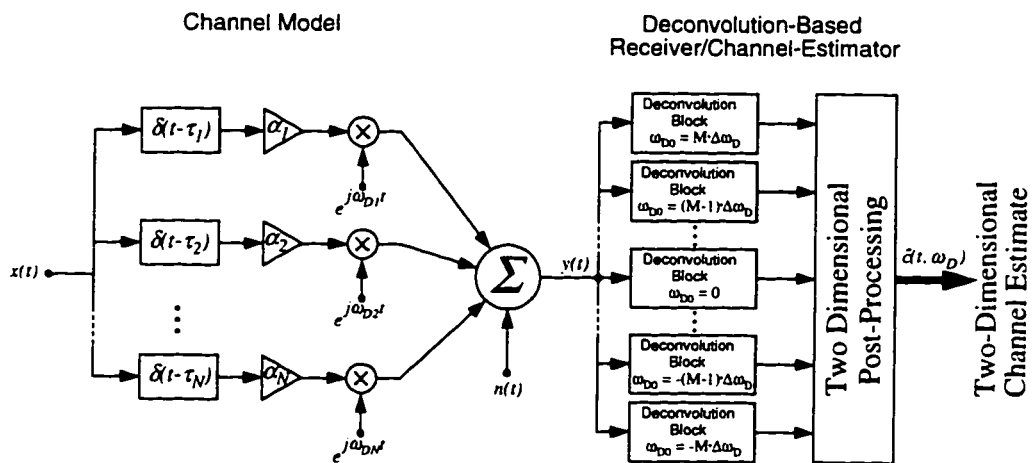


**Figure 3.2** The block diagram for the Doppler multipath channel model is shown at the left. The right side of the figure shows the generalized block diagram of a deconvolution-based channel parameter estimation system.

### 3.2 Inverse Filtering in the Presence of Doppler Multipath

As discussed in the previous section, various deconvolution methods —and hence various forms of inverse filtering— have been applied to the Doppler

multipath parameter estimation problem. This has been done in the hope that the accurate time delay estimation properties of the IF might be maintained in the Doppler environment, and also with the hope that the resulting outputs would be tolerant of or lead to estimates of the Doppler shift of the received multipath components.

There are inherent difficulties associated with IF type procedures when these procedures are used in a Doppler environment. The linearity property of the Fourier transform allows, without loss of generality, the consideration of the effect of a single multipath —in this case, the  $k^{th}$ — component on the IF output. Equation (3.4) then becomes

$$c_k(t) = FT^{-1} \left\{ \frac{Y(\omega)}{X(\omega)} \right\} = FT^{-1} \left\{ \frac{\alpha_k X(\omega - \omega_{D_k}) e^{j\omega\tau_k}}{X(\omega)} \right\}. \quad (3.5)$$

Note here that the  $\alpha_k$  and  $e^{j\omega\tau_k}$  terms contribute directly to amplitude scaling and time delay positioning only. Thus, for the purpose of studying the effects of Doppler on the IF output, it is sufficient to examine

$$\tilde{c}_k(t) = FT^{-1} \left\{ \frac{X(\omega - \omega_{D_k})}{X(\omega)} \right\}. \quad (3.6)$$

Equation (3.6) reveals the root of the so-called *ill-posed* problem (see, for example, [52]), whereby components with small magnitude in the spectrum of  $X(\omega)$  in the denominator of (3.6) do not line up with the corresponding components in the

spectrum of the frequency shifted version of  $X(\omega)$  in the numerator. Various ways of avoiding this problem have been suggested. These include protocol and signal design constraints imposed on the transmitted waveform as well as *post hoc* means of correcting the effects of the poles in the Fourier transform of the IF output. In the analysis that follows, it will be shown that, despite the ill-posed problem inherent in (3.6), an estimate of the IF output can be found for a certain class of probing waveforms which have most of the signal energy concentrated evenly within a region of flat bandwidth.

### 3.2.1 The Inverse Filter Output for a Windowed Sinusoid Input

In practice, an analytic form of the Fourier transform of most transmitted waveforms of interest (FM sweeps, frequency-hop codes, etc.) is hard, if not impossible, to calculate. Thus, an exact or analytic evaluation of (3.6) is often difficult to derive. It is instructive, however, to consider the following simple case: let the transmitted signal be a windowed sinusoid of frequency  $\omega_0$  such that

$$x(t) = \begin{cases} e^{j\omega_0 t}, & \text{for } 0 \leq t \leq N-1 \\ 0, & \text{for } t < 0 \text{ or } t \geq N \end{cases} \quad (3.7)$$

where the sampled signal  $x(t)$  is given as a function of discrete time,  $t$ , and  $N$  is the sampled time-length of  $x(t)$ .

The resulting form of (3.6) for the case of a windowed sinusoid input is given

by

$$\tilde{C}_k(\omega) = \frac{X(\omega - \omega_{D_k})}{X(\omega)} = e^{j\omega_{D_k}(N-1)/2} \left( \frac{\sin\left(\frac{N}{2}(\omega - \omega_{D_k} - \omega_0)\right)}{\sin\left(\frac{N}{2}(\omega - \omega_0)\right)} \right) \left( \frac{\sin\left(\frac{1}{2}(\omega - \omega_0)\right)}{\sin\left(\frac{1}{2}(\omega - \omega_{D_k} - \omega_0)\right)} \right), \quad (3.8)$$

where  $\tilde{C}_k(\omega)$  is the Fourier transform of  $\tilde{c}_k(t)$ . The calculation of  $\tilde{c}_k(t)$  from (3.8) requires that an inverse Fourier transform be performed, with the resulting expression being given by

$$\tilde{c}_k(t) = \frac{1}{2\pi} \int_{(-2\pi)}^{\infty} \tilde{C}_k(\omega) e^{j\omega t} d\omega. \quad (3.9)$$

Though there are  $N - 1$  simple poles on the  $\omega$  axis, (3.9) can be evaluated through the application of Cauchy's Residue Theorem [56] and several trigonometric approximations. The details are given in section 3.2.1.1, and the resulting expression for the IF output, as a function of time and Doppler shift, is given by

$$\tilde{c}_k(t, \omega_{D_k}) \equiv \delta(t) \frac{1}{2} \left( 1 + e^{j\omega_{D_k} N} \right), \quad (3.10a)$$

and the magnitude of the IF output for a windowed sinusoid input is given by

$$|\tilde{c}_k(t, \omega_{D_k})| \equiv \delta(t) \left| \cos\left(\frac{N}{2} \omega_{D_k}\right) \right|, \quad (3.10b)$$

where  $\delta(t)$  is the discrete-time delta-function having values,  $\delta(t) = \begin{cases} 1, & \text{for } t = 0 \\ 0, & \text{for } t \neq 0 \end{cases}$ .

Note the significance of equation (3.10):

- 1.) For the windowed sinusoid without noise, the output of the IF in the presence of Doppler has energy almost exclusively along the Doppler axis at the time delay value,  $t = 0$ . That is, the IF output has most of its energy only at the time delay where it *should* have energy. For all other values of  $t$ , the IF output is nearly zero. Thus, even in the presence of Doppler, the IF is able to determine signal delay parameters to within one sample period.
- 2.) Equation (3.10) has the rather satisfying result that, for  $\omega_{D_k} = 0$  (i.e. the received signal is not Doppler shifted), the output of the IF is exactly  $\delta(t)$ , as one would expect.
- 3.) Equation (3.10) gives the shape of the IF output along the Doppler axis, providing *a priori* knowledge about the effect that a Doppler shifted signal will have on the IF output response. Note also that this IF output response along the Doppler axis is not dependent on the frequency of the original transmitted sinusoid. Only the sampled time-length,  $N$ , determines the periodicity seen on the Doppler axis. This time-length is related to the sampling frequency,  $f_s$ , and the continuous time-length of the original signal,  $T$ , through  $N = Tf_s$ .
- 4.) The *skirts* (the region away from  $\omega_0$  in the signal spectrum) of the spectrum of the windowed sinusoid are due to the time-length of the transmitted waveform. Knowledge of the behavior of the windowed sinusoid in an IF/deconvolution system may provide insight into the behavior of the same system using other probing waveforms with similar skirts, as will be discussed in section 3.2.2.

### 3.2.1.1 Derivation of the Inverse Filter Output for a Windowed Sinusoid Input

The derivation that follows provides an analytic approximation to the time-domain inverse filter (IF) output for the case when the input to the IF system is a windowed sinusoid. This analysis is referenced in section 3.2.1 and used within sections 3.2.2.2 and 3.2.2.3 to describe the IF output for the case when the IF input waveform is a more arbitrary signals.

In the following, let  $t$  represent discrete time, and  $DTFT\{\cdot\}$  denotes the discrete time Fourier transform operation.

$$\text{Let } x(t) = \begin{cases} e^{j\omega_0 t} & , \text{ for } t = 0, 1, 2, \dots, N-1 \\ 0, & \text{for } t < 0 \text{ and for } t \geq N-1 \end{cases} \quad (3.11)$$

$$\text{then } X(\omega) = DTFT\{x(t)\} = \sum_{t=-\infty}^{+\infty} x(t) e^{-j\omega t} = \sum_{t=0}^{N-1} e^{-j(\omega - \omega_0)t} = \frac{1 - e^{-j(\omega - \omega_0)N}}{1 - e^{-j(\omega - \omega_0)}} \\ \Rightarrow X(\omega) = e^{-j(\omega - \omega_0)(N-1)/2} \left( \frac{\sin\left(\frac{N}{2}(\omega - \omega_0)\right)}{\sin\left(\frac{1}{2}(\omega - \omega_0)\right)} \right). \quad (3.12)$$

Now if  $x(t)$  is Doppler shifted by an amount  $\omega_D$ , then the DTFT of the Doppler shifted signal is

$$X(\omega - \omega_D) = e^{-j(\omega - \omega_D - \omega_0)(N-1)/2} \left( \frac{\sin\left(\frac{N}{2}(\omega - \omega_D - \omega_0)\right)}{\sin\left(\frac{1}{2}(\omega - \omega_D - \omega_0)\right)} \right). \quad (3.13)$$

The DTFT of the output of the inverse filter,  $C(\omega)$ , is the ratio

$$C(\omega) = \frac{X(\omega - \omega_D)}{X(\omega)} = e^{j\omega_D(N-1)/2} \left( \frac{\sin\left(\frac{N}{2}(\omega - \omega_D - \omega_0)\right)}{\sin\left(\frac{N}{2}(\omega - \omega_0)\right)} \right) \left( \frac{\sin\left(\frac{I}{2}(\omega - \omega_0)\right)}{\sin\left(\frac{I}{2}(\omega - \omega_D - \omega_0)\right)} \right), \quad (3.14)$$

and the time-domain output,  $y(t)$ , is given by

$$c(t) = DTFT^{-1}\{C(\omega)\} = \frac{I}{2\pi} \int_{(2\pi)} Y(\omega) e^{j\omega t} d\omega$$

$$c(t) = \frac{I}{2\pi} e^{j\omega_D(N-1)/2} \int_{(2\pi)} \left( \frac{\sin\left(\frac{N}{2}(\omega - \omega_D - \omega_0)\right)}{\sin\left(\frac{N}{2}(\omega - \omega_0)\right)} \right) \left( \frac{\sin\left(\frac{I}{2}(\omega - \omega_0)\right)}{\sin\left(\frac{I}{2}(\omega - \omega_D - \omega_0)\right)} \right) e^{j\omega t} d\omega. \quad (3.15)$$

Using the change of variables:  $z = e^{j\omega}$ ,  $d\omega = \frac{dz}{jz}$ , the expression for  $c(t)$  becomes

$$c(t) = \frac{I}{2\pi} e^{j\omega_D(N-1)/2} \oint_{|z|=1} \left( \frac{\frac{I}{2j}(z^{N/2} e^{-j(\omega_D + \omega_0)N/2} - z^{-N/2} e^{j(\omega_D + \omega_0)N/2})}{\frac{I}{2j}(z^{N/2} e^{-j\omega_0 N/2} - z^{-N/2} e^{j\omega_0 N/2})} \right) \left( \frac{\frac{I}{2j}(z^{I/2} e^{-j\omega_0/2} - z^{-I/2} e^{j\omega_0/2})}{\frac{I}{2j}(z^{I/2} e^{-j(\omega_D + \omega_0)/2} - z^{-I/2} e^{j(\omega_D + \omega_0)/2})} \right) z^t \frac{dz}{jz}$$

$$c(t) = \frac{I}{2\pi j} e^{j\omega_D(N-1)/2} \oint_{|z|=1} \left( \frac{z^N e^{-j\omega_0 N} e^{-j\omega_D N/2} - e^{j\omega_0 N/2}}{z^N e^{-j\omega_0 N} - 1} \right) \left( \frac{ze^{-j\omega_0} - 1}{ze^{-j\omega_0} e^{-j\omega_D/2} - e^{j\omega_D/2}} \right) z^{t-1} dz \quad (3.16)$$

where the contour integration is taken in the counter-clockwise direction in the complex plane. Note that, for  $t \geq 1$ , the quantity in the integrand has removable singularities at  $z = e^{j\omega_0}$  and  $z = e^{j(\omega_D + \omega_0)}$  and  $N - 1$  simple poles on the contour of integration at  $z = e^{j(\omega_0 + 2\pi k/N)}$ , for  $k = 1, 2, 3, \dots, N - 1$ . This integration above can be performed with the aid of Cauchy's Residue Theorem.

**Cauchy's Residue Theorem:** If  $f(z)$  is single-valued and analytic within a closed domain  $D$  and  $C$  is any closed, smooth curve in  $D$ , and if  $f(z)$  is regular on  $C$  except for a finite number of simple poles, then

$$\oint_C f(z) dz = 2\pi j \left( \sum \text{Res} + \frac{1}{2} \sum \text{Res}' \right)$$

where the integral exists in the Cauchy Principle Value sense, the  $\text{Res}$  are the residues of  $f(z)$  at its singularities inside  $C$ , and the  $\text{Res}'$  are the residues of  $f(z)$  at its simple poles on  $C$ , the integration being taken in the counter-clockwise direction. [56, 68]

Note: the residues of  $f(z) = \frac{Q(z)}{P(z)}$ , where  $Q(z)$  and  $P(z)$  are polynomials in  $z$ , can be found via:

$$\text{Res}(f, z) = \frac{Q(z)}{P'(z)}, \quad (3.17)$$

where  $P'(z) = \frac{d}{dz} P(z)$ , and the notation  $\text{Res}(f, z)$  should be read, "the residue of  $f$  at  $z$ ." In the case at hand,

$$Q(z) = \frac{\left( z^N e^{-j\omega_0 N} e^{-j\omega_D N/2} - e^{j\omega_D N/2} \right) (ze^{-j\omega_0} - 1) z^{l-1}}{ze^{-j\omega_0} e^{-j\omega_D/2} - e^{j\omega_D/2}}, \text{ and} \quad (3.18)$$

$$P(z) = z^N e^{-j\omega_0 N} - 1. \quad (3.19)$$

Taking the derivative of  $P(z)$  and simplifying gives

$$\left. \frac{Q(z)}{P(z)} \right|_{z=e^{j(\omega_0+2\pi k/N)}} = \text{Res}(f, z = e^{j(\omega_0+2\pi k/N)}) = \frac{2j}{N} e^{j\omega_0 t} e^{j2\pi k t/N} \sin\left(\frac{N}{2}\omega_D\right) \frac{\sin\left(\frac{\pi k}{N}\right)}{\sin\left(\frac{1}{2}\omega_D - \frac{\pi k}{N}\right)} \quad (3.20)$$

The application of Cauchy's Residue Theorem then gives the result below.

$$\begin{aligned} c(t) &= \frac{1}{2\pi j} e^{j\omega_D(N-1)/2} \pi j \sum_{k=1}^{N-1} \left. \frac{Q(z)}{P(z)} \right|_{z=e^{j(\omega_0+2\pi k/N)}} , \text{ for } t \geq 1 \\ c(t) &= \frac{j}{N} e^{j\omega_0 t} e^{j\omega_D(N-1)/2} \sum_{k=0}^{N-1} \frac{\sin\left(\frac{N}{2}\omega_D\right) \sin\left(\frac{\pi k}{N}\right)}{\sin\left(\frac{1}{2}\omega_D - \frac{\pi k}{N}\right)} e^{j2\pi k t/N} , \text{ for } t \geq 1 \\ c(t) &= \frac{j}{N} e^{j\omega_0 t} e^{j\omega_D(N-1)/2} \sum_{k=0}^{N-1} \left[ -\cos\left(\frac{1}{2}\omega_D\right) + \sin\left(\frac{1}{2}\omega_D\right) \cot\left(\frac{1}{2}\omega_D - \frac{\pi k}{N}\right) \right] e^{j2\pi k t/N} , \text{ for } t \geq 1 \end{aligned} \quad (3.21)$$

Here several simplifying approximations can be applied. For the narrowband assumption to be valid,  $\omega_D$  must be small relative to the time-bandwidth product of the transmitted signal, and thus also  $\omega_D \ll 1$ , so that the following approximations are valid:  $\cos\left(\frac{1}{2}\omega_D\right) \approx 1$ , and  $\sin\left(\frac{1}{2}\omega_D\right) \approx \frac{1}{2}\omega_D \approx 0$ , and  $c(t)$  can be written as,

$$c(t) \approx \frac{-j}{N} e^{j\omega_0 t} e^{j\omega_D(N-1)/2} \sin\left(\frac{N}{2}\omega_D\right) \sum_{k=0}^{N-1} e^{j2\pi k t/N} , \text{ for } t \geq 1. \quad (3.22)$$

Here note that, given the assumptions and approximations above, the summation of the samples of the complex exponential will evaluate to zero. Thus the time-domain output of the inverse filter, as a function of Doppler shift,  $\omega_D$ , will be:

$$c(t, \omega_D) \equiv 0, \quad \forall t \geq 1. \quad (3.23)$$

What remains then is to solve the original contour integral, (3.11), for the special case of  $t = 0$ . Here  $t = 0$  is the time at which the received signal matches up with the stored replica of the transmitted signal perfectly. The integral then becomes,

$$c(t) = \frac{1}{2\pi j} e^{j\omega_D t (N-1)/2} \oint_{|z|=1} \left( \frac{z^N e^{-j\omega_0 N} e^{-j\omega_D N/2} - e^{j\omega_D N/2}}{z^N e^{-j\omega_0 N} - 1} \right) \left( \frac{ze^{-j\omega_0} - 1}{ze^{-j\omega_0} e^{-j\omega_D/2} - e^{j\omega_D/2}} \right) \left( \frac{1}{z} \right) dz, \text{ for } t = 0, \quad (3.24)$$

where, as before, the integral is taken in the counter-clockwise direction in the complex plane. In addition to the removable singularities at  $z = e^{j\omega_0}$  and  $z = e^{j(\omega_D + \omega_0)}$  and the  $N - 1$  simple poles on the contour of integration,  $z = e^{j(\omega_0 + 2\pi k/N)}$ , for  $k = 1, 2, 3 \dots N-1$ , there is one additional simple pole at  $z = 0$ .

Note that the equation for  $y(n)$  can be written as

$$c(t) = \frac{1}{2\pi j} e^{j\omega_D t (N-1)/2} \oint_{|z|=1} g(z) dz, \quad (3.25)$$

$$\text{where } g(z) = \frac{R(z)}{S(z)},$$

$$\text{and } R(z) = \frac{(z^N e^{-j\omega_0 N} e^{-j\omega_D N/2} - e^{j\omega_D N/2})(ze^{-j\omega_0} - 1)}{ze^{-j\omega_0} e^{-j\omega_D/2} - e^{j\omega_D/2}}, \quad (3.26)$$

$$\text{and } S(z) = z^{N+1} e^{-j\omega_0 N} - z. \quad (3.27)$$

Again, the integral can be solved using Cauchy's Residue Theorem.

$$c(t) = \frac{1}{2\pi j} e^{j\omega_D t (N-1)/2} \left[ 2\pi j \left( \text{Res}(g(z), z=0) + \frac{1}{2} \sum_{k=1}^{N-1} \text{Res}(g(z), z = e^{j(\omega_0 + 2\pi k/N)}) \right) \right], \text{ for } t = 0. \quad (3.28)$$

Once again, note that the residues can be found via,  $Res(g, z) = Res\left(\frac{R(z)}{S(z)}, z\right) = \frac{R(z)}{S'(z)}$ .

The residue at the simple pole at the origin is found to be

$$Res(g, z = 0) = e^{j\omega_D(N-1)/2}, \text{ for } t = 0, \quad (3.29)$$

and the residues on the contour of integration are found to be

$$Res\left(g, z = e^{j(\omega_0 + 2\pi k/N)}\right) = \frac{2j}{N} \sin\left(\frac{N}{2}\omega_D\right) \frac{\sin\left(\frac{\pi k}{N}\right)}{\sin\left(\frac{1}{2}\omega_D - \frac{\pi k}{N}\right)}, \text{ for } t = 0. \quad (3.30)$$

Adding these residues in the manner dictated above and rearranging terms gives

$$c(0) = e^{j\omega_D(N-1)} + \frac{j}{N} e^{j\omega_D(N-1)/2} \sin\left(\frac{N}{2}\omega_D\right) \sum_{k=1}^{N-1} \frac{\sin\left(\frac{\pi k}{N}\right)}{\sin\left(\frac{1}{2}\omega_D - \frac{\pi k}{N}\right)}. \quad (3.31)$$

As was done for the case of  $t \geq 1$ , the term in the summation can be approximated as

$$\frac{\sin\left(\frac{\pi k}{N}\right)}{\sin\left(\frac{1}{2}\omega_D - \frac{\pi k}{N}\right)} \approx -1, \text{ for } \omega_D \ll 1. \quad (3.32)$$

This approximation gives

$$c(0) = e^{j\omega_D(N-1)} + \frac{j(N-1)}{N} e^{j\omega_D(N-1)/2} \sin\left(\frac{N}{2}\omega_D\right). \quad (3.33)$$

With the further approximation that, for large values of  $N$  and small values of  $\omega_D$ ,

$\frac{(N-1)}{N} \approx 1$  and  $\cos(N\omega_D) \approx \cos\left(\left(N - \frac{1}{2}\right)\omega_D\right)$ , the time-domain output of the inverse filter at  $t = 0$  as a function of Doppler shift,  $\omega_D$ , can be approximated as

$$c(0, \omega_D) \approx \frac{1}{2} \left( 1 + e^{j\omega_D N} \right). \quad (3.34)$$

Combining equations (3.23) and (3.34) and applying symmetry arguments gives the time-domain output of the inverse filter for a windowed complex sinusoid, as a function of the Doppler shift of the received signal,  $\forall t$ :

$$c(t, \omega_D) \approx \delta(t) \frac{1}{2} \left( 1 + e^{j\omega_D N} \right), \quad (3.35a)$$

or

$$|c(t, \omega_D)| \approx \delta(t) \left| \cos\left(\frac{N}{2}\omega_D\right) \right|, \quad (3.35b)$$

where  $\delta(t)$  is the discrete-time delta-function having values,  $\delta(t) = \begin{cases} 1, & \text{for } t = 0 \\ 0, & \text{for } t \neq 0 \end{cases}$ .

### 3.2.2 The Inverse Filter Output for a Transmitted Signal with a Flat Spectrum

Using the analysis of the previous section as launching point, the topic of inverse filtering in the presence of Doppler with more arbitrary signals is now addressed [57]. The discussion is extended to include transmitted signals that

possess a reasonably flat spectrum within which most of the signal energy is contained. Outside the flat part of the spectrum, these signals will have skirts, the forms of which are dependent on the time-length of the signal and the energy distribution and phase characteristics of the flat region of the spectrum. This covers a broad class of signals that are used in spread spectrum communications and military ranging applications. Such signals include linear FM chirps and full frequency-hop codes [42] and also CW pulse (windowed sinusoid) waveforms —which may be thought of as signals with a near zero-width flat spectrum region or, equivalently, with a spectrum that is made up almost entirely of the *skirts* described above.

The spectrum of the sampled waveform, then, will be occupied chiefly by two components: the flat part of the signal spectrum where most of the energy resides, and the region outside the signal bandwidth where skirt effects are visible (see Figure 3.3a and 3.3b). The fraction of the spectrum occupied by each component is determined by the sampling rate of the system. As the sampling rate is decreased toward the Nyquist rate, the region occupied by the skirts decreases relative to that of the flat area of the signal spectrum. The converse is true for an increase in the sampling rate.

Due to the inversion process of the IF, the output spectrum of the IF will have sizable energy in the area formerly occupied by the skirts (Figure 3.3c and 3.3d). Thus, this region of the spectrum cannot be neglected in an analysis of the IF output.

In the derivation that follows, the output of the IF will be considered as the composition of the two separate regions delineated above. When the analyses are

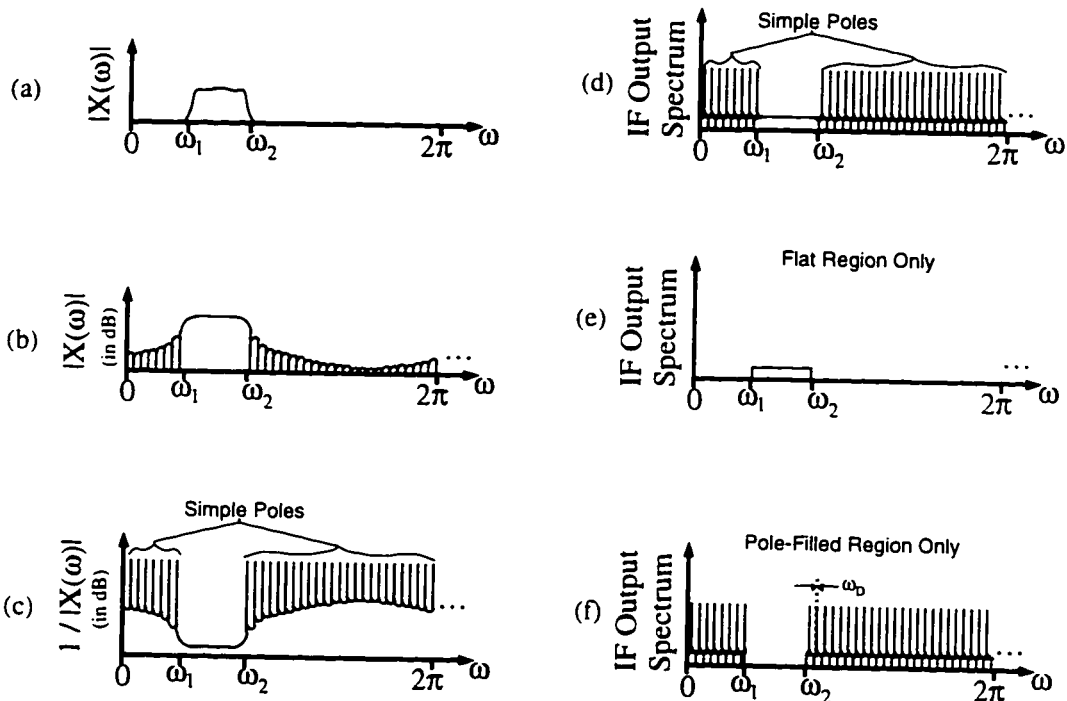


**Figure 3.3** (a) shows the characteristics the spectrum of a well-behaved wideband probing signal,  $X(\omega)$ , and (b) shows the characteristics of the same spectrum when plotted on a log scale. (c) shows what happens when  $X(\omega)$  is inverted. Note the energy in the region of the spectrum formerly occupied by the skirts. (d) shows the output spectrum of the inverse filter (IF); note that the skirts of the finite time-length transmitted signal and Doppler mismatched with the stored reference signal cause significant energy to appear in the output spectrum of the IF in the region formerly occupied by the signal skirts. (e) shows the flat part of the IF output spectrum, and (f) shows the remaining part of the IF output spectrum, which contains skirt effects. The 3 dB points of  $X(\omega)$  are also shown on the  $\omega$  axis.

complete, the linearity property of the Fourier transform will allow the separate analyses of the two regions to be summed for a total IF output.

### 3.2.2.1 The Ambiguity Function Effect

We focus now on the fundamental inverse filtering equation, (3.6), in the

context of signals which have a reasonably flat bandwidth, and make the following manipulation:

$$\tilde{C}_k(\omega) \equiv \frac{X(\omega - \omega_{D_k})}{X(\omega)} = \frac{X^*(\omega)X(\omega - \omega_{D_k})}{|X(\omega)|^2} = W(\omega) \bullet FT\{\chi_{xx}^*(-t, \omega_D - \omega_{D_k})\}, \quad (3.36)$$

where  $\chi_{xx}(t, \omega_D)$  is the narrowband auto-ambiguity function of  $x(t)$  [28,29,34], and the windowing function,  $W(\omega)$ , is the inverted power spectrum of the transmitted waveform,

$$W(\omega) = \frac{1}{|X(\omega)|^2}. \quad (3.37)$$

The power spectrum of a signal which has a flat spectrum in the range  $[\omega_1, \omega_2]$  will also be flat in the same region, and so also will the inverse of the power spectrum (see Figure 3.3). Let us assume that  $x(t)$  is normalized to unit energy such that

$$E_x \equiv \frac{1}{2\pi} \int_{(2\pi)} |X(\omega)|^2 = 1. \quad (3.38)$$

Combining this with the assumption of a flat spectrum and the fact that most of the energy in the signal is contained in the region of flat bandwidth, it thus follows that, within the region  $[\omega_1, \omega_2]$ , the windowing function is approximately constant and is given by

$$W(\omega) = \frac{1}{|X(\omega)|^2} \equiv \frac{BW_x}{2\pi}, \text{ for } \omega_1 < \omega < \omega_2. \quad (3.39)$$

where  $BW_x = \omega_1 - \omega_2$  is the radian bandwidth of the sampled transmitted signal.

The contribution of the flat part of the spectrum to the total time-domain output of the IF can then be written as

$$\tilde{c}_k(t, \omega_D) \equiv \frac{BW_x}{2\pi} \chi_{xx}^*(-t, \omega_D - \omega_{D_k}). \quad (3.40)$$

### 3.2.2.2 The Cosine Effect

Consider now the IF output spectrum in the region outside  $[\omega_1, \omega_2]$ . This part of the IF output spectrum is dominated by the effects of the spectral skirts of the transmitted waveform. These skirts are due to the finite time-length of the probing waveform that is employed in the multi-path estimation system and are a result of the frequency-domain convolution of the spectrum of the flat-spectrum probing signal with the spectrum of the window that is used to truncate the transmitted waveform to finite time-length. In some cases where the bandwidth within  $[\omega_1, \omega_2]$  is reasonably flat and free from abrupt phase changes (later referred to as *well-behaved*) —such as for linear FM sweeps and some full frequency-hop codes—, the behavior of the spectral skirts of the probing signal closely approximates the skirts of the windowed sinusoid that was studied previously (see Figure 3.4). The contribution of the spectral skirts of the probing signal to the IF output can, then, for some signals be approximated by the output of the IF when a windowed sinusoid is used as the input

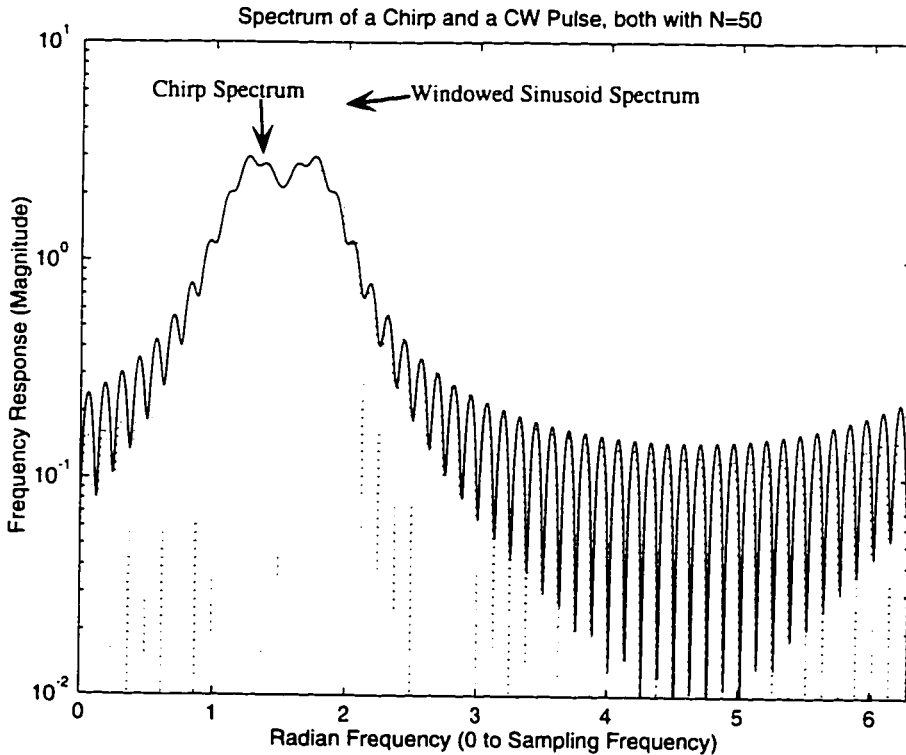


**Figure 3.4** Plot of the spectra of a linear FM chirp and a windowed sinusoid, both of sampled time-length  $N = 50$ . Note the similarity in the form of the skirts. This similarity is employed to approximate the effects of the spectral skirts on the output of an IF/deconvolution system.

probing signal.

Where the skirts of other probing signals closely resemble the skirts of the windowed sinusoid, the previous analysis of sections 3.2.1 and 3.2.1.1 may be used to approximate the time-domain IF output for these *well-behaved* flat-bandwidth probing signals, with the notable difference being that the contour of integration is no longer the entire unit circle but, rather, is the unit circle minus the region  $[\omega_1, \omega_2]$ , as shown in Figure 3.5. In sections 3.2.1 and 3.2.1.1, it was shown for the windowed sinusoid that —due to an even distribution of poles on the unit circle— each segment

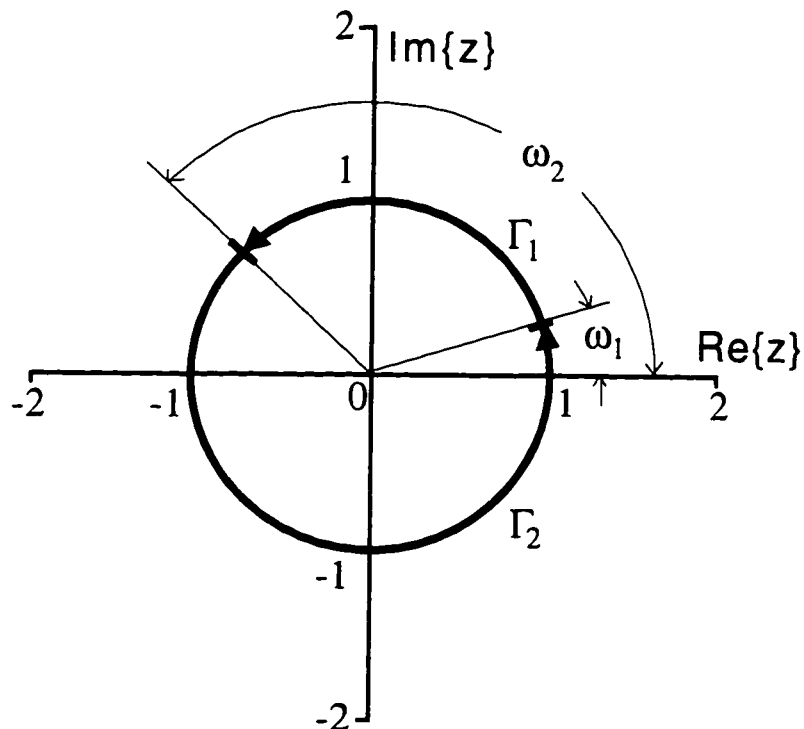


**Figure 3.5** Contour of integration for analysis of the inverse filter output when the transmitted signal has a flat bandwidth.

of the unit circle which is included in the contour of integration (that is needed to calculate the time-domain IF output) contributes an approximately equal portion to the total sum of residues which makes up the final output result (equation (3.10)). Applying this result to the well-behaved flat-bandwidth case gives an approximation for the time-domain IF output due to the spectral skirts of the probing signal.

$$\tilde{c}_k(t, \omega_D) \equiv \left(1 - \frac{BW_x}{2\pi}\right) \delta(t) \frac{1}{2} \left(1 + e^{j\omega_D N}\right), \quad (3.41a)$$

and the magnitude of this contribution to the total IF output for a well-behaved flat-

bandwidth transmitted signal is given by

$$|\tilde{c}_k(t, \omega_D)| \approx \left(1 - \frac{BW_x}{2\pi}\right) \delta(t) \left| \cos\left(\frac{N}{2} \omega_D\right) \right|, \quad (3.41b)$$

where the  $(1 - BW_x/2\pi)$  scale factor is due to the contour of integration,  $\Gamma_2$  in Figure 3.5, that does not include the entire unit circle (the contribution due to  $\Gamma_1$  in Figure 3.5 —the ambiguity-function effect— was found above in 3.2.2.1 by inspection).

Not all probing signals will have skirts that resemble the spectrum of the windowed sinusoid; the spectral zeros may not be evenly spaced in the complex  $z$ -plane and may not lie on or near the unit circle. Thus, the approximation in (3.41a) and (3.41b) is not applicable for all signals of interest. From the analysis of section 3.2.1.1, it is useful to note that the extra pole at time,  $t = 0$ , will still influence the IF output even for probing signals that are not well-behaved, as we have defined the term above. The presence of this extra pole is responsible for part of the ridge of energy visible on the Doppler axis of the IF output (see (3.28) - (3.31) in section 3.2.1.1), while the specific signal characteristics of the windowed sinusoid give this ridge its cosine-like shape. The extra pole might, therefore, be expected to have a similar contribution to the IF output for probing signals that are not well-behaved. Our experimental results demonstrate that this ridge of energy still exists on the Doppler axis for signals that are not well-behaved, with the exact shape of the ridge varying from signal to signal. Note again that an analytic form of the Fourier transform of most flat-bandwidth probing signals of finite length is difficult, if not

impossible, to derive, and, likewise, it is less likely to be able to derive an analytic form of the time-domain IF output for most signals of interest. However, our experimental results indicate that the following general model describes the output of the IF due to the effect of the spectral skirts of flat-bandwidth signals that are not well-behaved.

$$|\tilde{c}_k(t, \omega_D)| = \delta(t) \left[ \gamma + g(\omega_D) \cdot \cos\left(\frac{N}{2} \omega_D + \phi\right) \right] + a(t, \omega_D), \quad (3.41c)$$

where  $\gamma$ ,  $g(\omega_D)$ , and  $\phi$  are signal dependent,  $N$  and  $\delta(t)$  are as defined above, and  $a(t, \omega_D)$  is a function representing the signal dependent artifacts of the IF process that lie outside of the Doppler axis in the delay-Doppler plane. Equation (3.41c) embodies our experimental results. The vague form of (3.41c) indicates that the cosine-like ridge that is visible in the IF output for well-behaved signals may also be present in the IF output for signals that are not well-behaved, but the cosine term appears with a signal dependent amplitude modulation and offset. Furthermore, for the signals that are not well behaved, significant energy may be present in the IF output away from the Doppler axis, as indicated in (3.41c) by the IF artifact term,  $a(t, \omega_D)$ .

Equations (3.41a) and (3.41b) are useful for describing the effect of the skirts on the IF output for such common signals as linear FM sweeps and pulsed sinusoids, as well as for frequency-hop waveforms that are designed to have well-behaved phase characteristics in the region of flat bandwidth. Equation (3.41c) emphasizes

that such a concise description as (3.41a) and (3.41b) is not available for arbitrary signals, and that the skirts for signals that are not well-behaved and the artifacts that these skirts produce in the IF output may adversely affect the accuracy of a deconvolution-based multipath estimation procedure.

### 3.2.3 The Total Estimate of the Inverse Filter Output

Equations (3.40) and (3.41) may be summed to obtain an approximation of the total IF output for a single received multipath component. Combining the equations gives the total IF output as a function of delay and Doppler shift. For well-behaved flat-bandwidth signals,

$$\tilde{c}_k(t, \omega_D) \equiv (1 - \beta) \cdot \delta(t) \frac{1}{2} (1 + e^{j\omega_D N}) + \beta \cdot \mathcal{X}_{xx}^*( -t, \omega_D - \omega_{D_k} ) \quad (3.42a)$$

where  $\beta = BW_x / 2\pi$ , and when the cross terms are small, the magnitude of the IF output can be written as

$$|\tilde{c}_k(t, \omega_D)| \equiv (1 - \beta) \cdot \delta(t) \left| \cos\left(\frac{N}{2} \omega_D\right) \right| + \beta \cdot |\mathcal{X}_{xx}^*( -t, \omega_D - \omega_{D_k} )|. \quad (3.42b)$$

For the case when the flat-bandwidth signals are not well-behaved (as defined in 3.2.2.2 above), the exact form of the cosine effect will vary from signal to signal, and the more general, experimentally-derived, model below is used to describe the IF output in the presence of Doppler.

$$|\tilde{c}_k(t, \omega_D)| = \delta(t) \left[ \gamma + g(\omega_D) \cdot \cos\left(\frac{N}{2}\omega_D + \phi\right) \right] + a(t, \omega_D) + \beta \cdot |\mathcal{X}_{xx}^*(t, \omega_D - \omega_{D_k})|, \quad (3.42c)$$

where  $\gamma$ ,  $g(\omega_D)$ , and  $\phi$  are as described in (3.41c), and —by the definition of the IF—  $\gamma$ ,  $g(0)$ ,  $\cos(\phi)$ , and  $\beta \cdot |\mathcal{X}_{xx}^*(0, 0)|$  must sum to produce  $|\tilde{c}(t, \omega_D)|_{t=0, \omega_D=0} = 1$ .

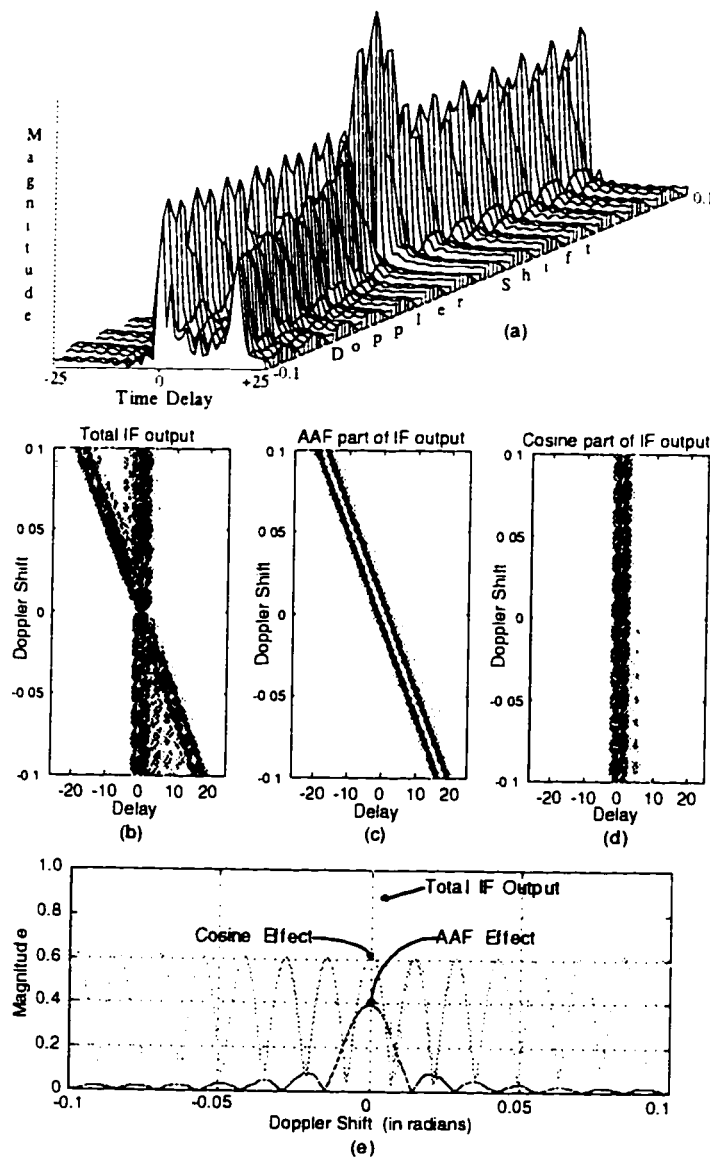
For well-behaved flat-bandwidth signals, (3.42) predicts the output of the IF in terms of quantities that are known or that can be calculated *a priori* based on the characteristics of the transmitted waveform. Note also that the cosine effect is free of range-Doppler coupling effects. Furthermore, for a given signal, the relative importance of the ambiguity effect or cosine effect can be controlled by the system sampling rate. An increase in the sampling rate will cause a linear decrease in  $\beta$ , which lessens the influence of the signal's ambiguity function on the IF output. Thus when the sampling frequency is near the Nyquist rate, the ambiguity effect will dominate. When the received signal is sampled well above the Nyquist rate, the cosine effect will dominate.

For the well-behaved flat-bandwidth signals, the contribution of the spectral skirts to the IF output —as embodied in (3.41a), (3.41b), (3.42a) and (3.42b)— can be used to improve the multipath parameter estimates through the application of appropriate post-processing methods, as will be explained in more detail in section 3.3. The spurious artifacts that are, for signals that are not well-behaved, part of the contribution of the spectral skirts to the IF output —as embodied in (3.41c) and (3.42c)— may actually hinder the estimation procedure. Indeed, for signals that are

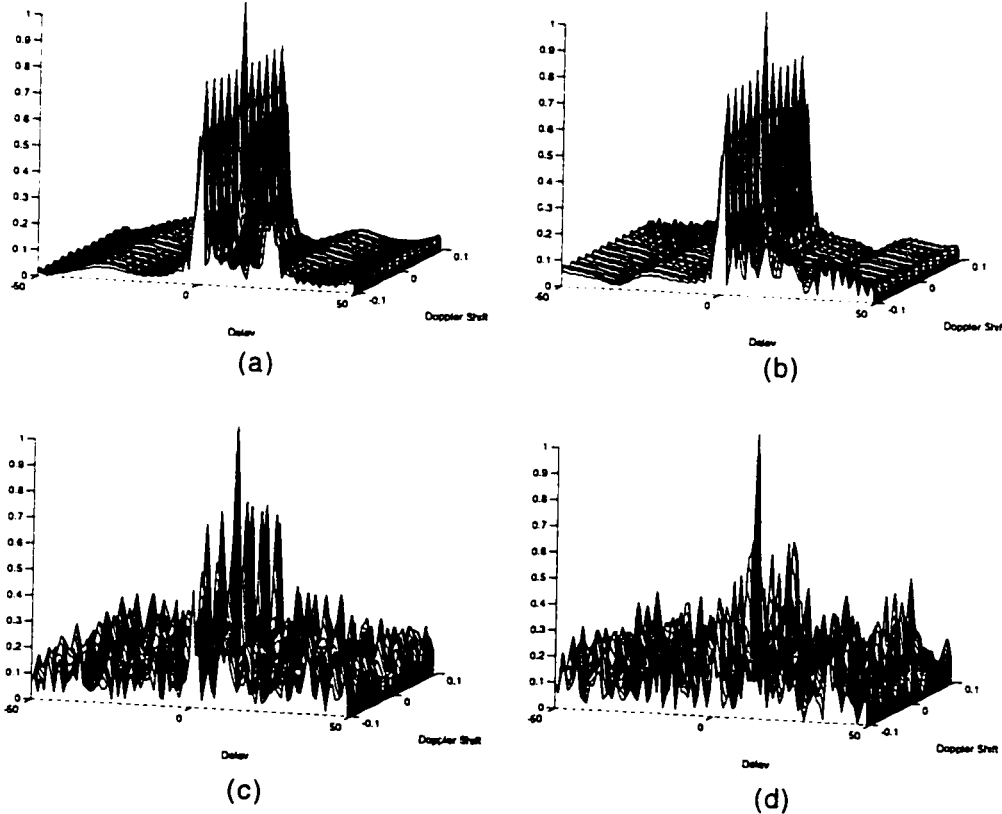
not well-behaved, the artifacts of the spectral skirts may lead to poorer results than those that would be obtained if only the ambiguity effect was used to produce the channel estimate while the region of the IF output spectrum that contains the skirt effects was ignored altogether. So, depending on the properties and design of the probing waveform that is employed in a given system, the skirt effects can be either a tool for more accurate parameter extraction or a hindrance to the estimation process.

Figure 3.2 shows the block diagram of a generic Doppler multipath deconvolution system. Each deconvolution block is centered around a different Doppler shift, the outputs of which are predicted by (3.42). Shown in Figure 3.6 is the output of a system such as that in Figure 3.2 when the deconvolution blocks are direct implementations of (3.4). The probing signal in Figure 3.6 is a linear FM chirp having sampled time-length of  $N = 450$  and a radian bandwidth of  $BW_x = 0.8\pi$ . Shown in the figure are various plots which separate out the effects of the flat part of the bandwidth from the effects of the spectral skirts on the final time-domain output. Note especially on the plot of the Doppler axis, Figure 3.6e, how the IF output conforms to the estimate given in (3.42).

In Figure 3.7, similar outputs are shown for the case when different probing signals are employed, some of which are not well-behaved. In all of the plots in Figure 3.7, the probing signals each have a sampled time-length of  $N = 360$  and a radian bandwidth of  $BW_x = 0.5\pi$ . Note that in Figure 3.7a and 3.7b the IF output corresponds closely to the estimates of (3.42a) and (3.42b), because the signals that are used to produce these plots are well-behaved. A linear congruence frequency-



**Figure 3.6** (a) shows a mesh plot of the output of an ideal inverse filter (IF) in the presence of Doppler for the case when the input is a linear FM chirp with sampled time-length of  $N=450$  and radian bandwidth of  $BW=0.8\pi$ . (b) shows a contour plot of the same data. (c) shows the contour plot of the IF output when only the region of the IF output spectrum inside  $[\omega_1, \omega_2]$  (as shown in Figure 3.1) is considered, thus showing the ambiguity function effect. (d) considers only the effect of the region of the IF output spectrum outside  $[\omega_1, \omega_2]$  and shows that this region contributes directly to the cosine effect. (e) shows a slice of the IF output parallel to the Doppler axis at  $Delay = 0$  and overlays the two contributors to the total IF output, verifying the presence and relative weights of the auto-ambiguity function and cosine effects as described by equation (3.42).



**Figure 3.7** The plots show the output of an ideal inverse filter (IF) for four different probing signals. The probing signals differ in their design and in the degree to which they can be considered as well-behaved. Each probing signal has a sampled time-length of  $N = 360$  and a radian bandwidth of  $BW_x = 0.5\pi$ . (a) shows the IF output for a linear FM chirp. (b) is for a hyperbolic FM sweep. (c) is for a linear congruence frequency-hop code with prime = 11 and multiplier = 2. (d) is for a Welch-Costas frequency-hop code with prime = 11, primitive root = 2, and multiplier = 3. Note that the signals used for (a) and (b) are reasonably well-behaved, and the IF outputs shown in (a) and (b) correspond closely to the estimate in equation (3.42b). The IF output (c) begins to depart from the estimates of (3.42b), showing significant artifacts away from the Doppler axis. The IF output of (d) is for the case when the probing signal is a Welch-Costas frequency-hop code. The phase jumps in this signal are more severe than those in the linear congruence code, as is evidenced in (d) by the greater prevalence of artifacts in the IF output away from the Doppler axis and also by the weakening of the ridge along the Doppler axis.

hop code [26] is used to produce the IF output of Figure 3.7c. Because of the abrupt phase jumps in the flat-bandwidth region of this particular linear congruence code, it begins to depart from what one could properly label as a well-behaved signal. The IF output of Figure 3.7c also begins to depart from the estimates of (3.42a) and (3.42b), showing significant artifacts away from the Doppler axis. Figure 3.7d is the IF output for the case when the probing signal is a Welch-Costas frequency-hop code [26]. The phase jumps in this signal are more severe than those in the linear congruence code, as is evidenced in Figure 3.7d by the greater prevalence of artifacts in the IF output away from the Doppler axis and also by the weakening of the ridge along the Doppler axis.

### 3.3 Deconvolution in the Presence of Doppler

Because of a high sensitivity to small amounts of additive noise, it is impractical to use a direct implementation of the IF. Hence, in order to take advantage of the resolution capabilities of the IF within a realistic setting, some variation of constrained inverse filtering must be performed. In the absence of noise, these practical deconvolution procedures reduce to inverse filtering, but use some kind of shaping, smoothing, and/or clipping process to reduce the susceptibility of the output to spuriously generated artifacts [47,48,51,52,54,58-63]. In this section two possible deconvolution methods —POCS and LS— are considered in the context of the Doppler multipath problem, and the utility and validity of the results that were

derived in section 3.2 are verified.

### 3.3.1 Doppler Multipath Parameter Estimation Via POCS

The method of Projection onto Convex Sets (POCS) has been used in the past as a means of image restoration [54,58-61]. In these applications, POCS operates on a distorted input image and forces the output, via a series of projection operations, to belong to a closed set known to contain the true solution. The projection operators are formulated on the basis of *a priori* knowledge of the distortion function and/or the form of the true output image. The POCS procedure is iterative and uses the output of the  $i^{th}$  iteration —an estimate of the true image—as the input to the  $(i+1)^{th}$  iteration.

Kostic *et al.* [63] applied POCS to the problem of multipath parameter estimation, and recently the method was extended to include Doppler, as in (3.1), as one of the multipath parameters [55]. Below are discussed in brief the possible constraints employed by Kostic, and the relevance of the derivation given in section 3.2 to a practical deconvolution technique is demonstrated. The reader is referred to [63-65] for the derivations and more detailed discussion.

As is common in some other deconvolution methods [47-48], the POCS system benefits from performing a preprocessing operation on the raw received data; in the case of [55,63] the preprocessing consists of passing the received data through a matched filter that is tuned to receive the transmitted signal,  $x(t)$ . The outputs of

the preprocessors are given by

$$g_m(t) = y(t) \otimes x^*(T-t)e^{j\omega_{D_m} t}, \quad (3.43)$$

where  $y(t)$ ,  $x(t)$ , and  $T$  are as given in (3.1) and (3.2),  $\omega_{D_m} = m \cdot \Delta\omega_D$  is the Doppler shift around which the  $m^{\text{th}}$  deconvolution block is centered (Figure 3.2), and  $\Delta\omega_D$  is related to the Doppler resolution of the system.

For use in the operator descriptions below, define the *residual*,  $r(t)$ , associated with the discrete time signal  $c_i(t)$  as:

$$r(t) = g(t) - h(t) \otimes c_i(t), \quad (3.44)$$

where:  $g(t)$  = the matched filter output,

$h(t)$  = the probing signal auto-correlation,

and  $c_i(t)$  = the current channel estimate of one of the  $2M+1$  Doppler slices.

The residual is the result of trying to subtract off all influences of the channel and probing signal from the matched filter output, and, as such, is an indicator of the exactness of the channel estimate. If the current channel estimate is accurate, the residual itself will be a function of the channel noise only, and the variance of the residual should match the variance of the noise. This concept has lead to the development and application of the *variance of the residual* constraint, which for the discrete time case is defined to be

$$C_v = \left\{ \mathbf{c}_i \left| \sum_t |g(t) - h(t) \otimes c_i(t)|^2 \leq B_v \right. \right\}, \quad (3.45)$$

where  $C_v$  denotes the constraint,  $c_i(t)$  denotes the channel estimate made as a result of the constraint, and  $B_v$  is a bound determined by the noise statistics and desired confidence level. In the noiseless case,  $c_i(t)$  is equivalent to the  $c(t)$  of (3.4). In the presence of noise,  $c_i(t)$  approaches the  $c(t)$  of (3.4), but does so while eliminating some of the spurious artifacts that may be incurred when an IF is applied to a noisy received signal. The *variance of the residual* constraint forces the residual to take on the characteristics of the channel noise, which may be measured at a time when it is known that no signal has been transmitted. The tightness of the constraint is determined by the confidence level used in assigning  $B_v$ .

The projection operator used in conjunction with (3.45) is most easily given in the frequency domain:

$$C_i(\omega) = \frac{C_{i-1}(\omega) / \lambda + H^*(\omega)G(\omega)}{|H(\omega)|^2 + 1 / \lambda}, \quad (3.46)$$

where:  $C_i(\omega)$  = the FT of the current estimate of the channel,

$C_{i-1}(\omega)$  = the FT of the previous estimate of the channel  
 $= G(\omega)$  for the first POCS iteration,

$\lambda$  = Lagrange multiplier,

$H(\omega)$  = the power spectrum of the transmitted signal  
 $= X(\omega)X^*(\omega)$ ,

and  $G(\omega)$  = the FT of the matched filter output  
 $= Y(\omega)X^*(\omega)$ .

The variance of the residual constraint is the most powerful within the POCS algorithm proposed in [63]. In the noiseless case,  $\lambda$ , the Lagrange multiplier, grows very large, and (3.46) reduces to direct inverse filtering. Because of this, it is reasonable to expect the output of POCS to approximate the output of an IF, and so the knowledge provided by (3.42) in section 3.2 can be used to devise post-processing methods that are meant to glean the multipath parameters from the POCS output.

In general, a greater number of POCS constraints produces a more accurate channel estimate. Other constraints suggested in [63] include various nonlinear constraints based on the expected form of the channel estimate (*finite support, positivity, realness, and boundedness*) as well as two additional constraints based on the noise statistics (*mean of the residual* and *outliers of the residual*). Not all of these constraints are applicable in all channel estimation contexts. For our purposes, knowledge of the variance of the residual constraint is sufficient, and the reader is again referred to the original works [63-65] to obtain more information on the other constraints.

A POCS output for simulated data is shown in Figure 3.8b. Due to noise effects, surviving IF artifacts, and the interference among received signal echoes, the POCS output itself may appear cluttered, and a clear estimate of the multipath

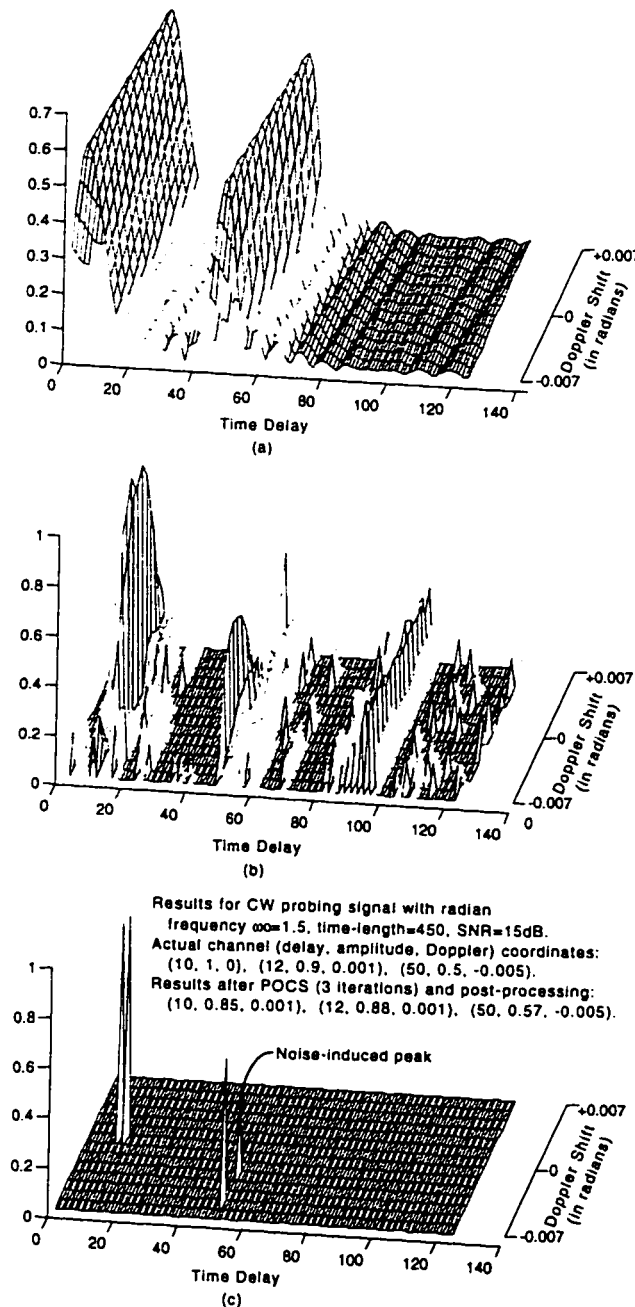


**Figure 3.8** (a) shows the output of a correlation-type estimator when the input is a linear FM chirp with time-length  $N= 450$  and radian bandwidth of  $BW_x = 1.0$ . Note how the two closely spaced peaks near *Delay* = 10 are not resolved and how the range-Doppler coupling of the chirp signal causes "tilt" and, hence, uncertainty along the Doppler axis. (b) shows the output of the POCS deconvolution system for a CW probing signal. (c) shows the final result after post-processing that is based on equation (3.42). Note how most of the extraneous, noise-related information is removed by the post-processing.

parameters is not obvious from inspection. Yet because (3.42) provides a description of how the multipath components influence the IF output, it is possible to remove much of the clutter from the POCS output.

The post-processing method developed and applied to the data in Figure 3.8b performs a curve-fitting analysis parallel to the Doppler axis at each time delay,  $t = \tau_k$ , where the POCS procedure had produced output energy. If, at a given delay value, the observed data parallel to the Doppler axis conform to the sampling-rate-dependent sum of the cosine effect and ambiguity effect described by (3.42b), the curve-fitting procedure determines the Doppler shift value,  $\omega_{D_k}$ , and the amplitude,  $\alpha_k$ , that minimize the error between the observed data and the fitted curve. If the observed data parallel to the Doppler axis at a given delay do not conform to the curve predicted by (3.42b), the data at that delay are assumed to be byproducts of the noise, surviving IF artifacts, and/or interference among the received signal echoes and are eliminated from the final multipath estimate. For a more detailed discussion of the post-processing curve-fitter, refer to section 3.3.1.1.

The final multipath estimate is shown in Figure 3.8c after the POCS output has been evaluated by the post-processing routine. In this case, the transmitted signal was a windowed sinusoid of radian frequency,  $\omega_0 = 1.5$  radians, and sampled time-length,  $N = 450$  samples. The simulated channel contained three specular multipath components with  $\{(\tau_k, \alpha_k, \omega_{D_k}), 1 \leq k \leq N_k\}$  parameters of  $\{(10, 1.0, 0.000)_1, (12, 0.9, 0.001)_2, (50, 0.5, -0.005)_3, 1 \leq k \leq 3\}$ . Note that the time delay of the two closely spaced multipath components is accurately resolved, but the procedure is still

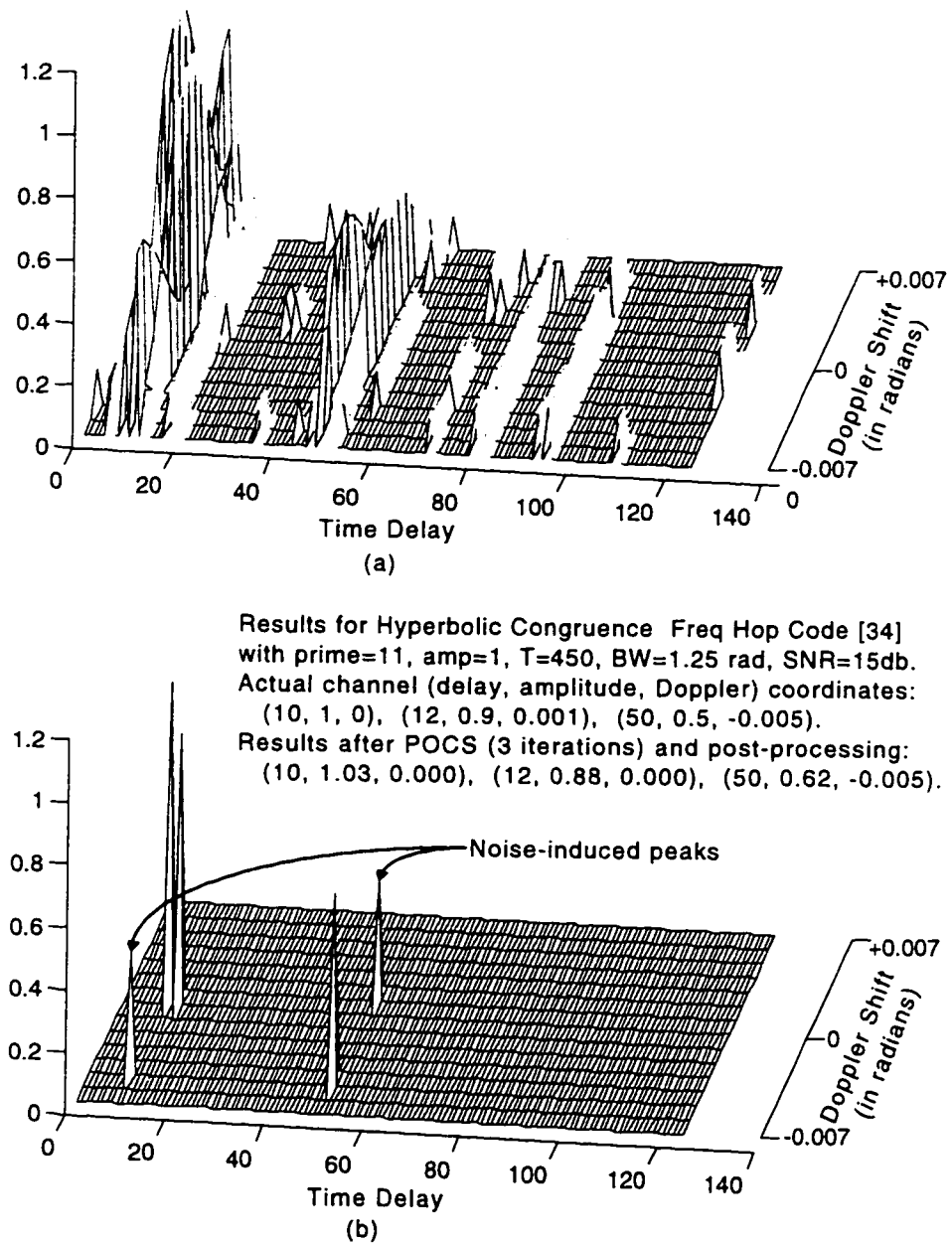


**Figure 3.9** (a) shows the output of the POCS deconvolution system when the probing signal is a hyperbolic congruence frequency-hop code [25] with time-length  $N = 450$  and radian bandwidth of  $BW_x = 1.25$ . (b) shows the result after post-processing based on (3.42) has been applied to the POCS output.

not completely immune to the effects of noise, with small errors being made in the estimation of the amplitude and Doppler parameters. In Figure 3.9 similar results are shown for the case when the probing signal has a flat bandwidth (in this instance a hyperbolic congruence frequency-hop code [25]).

### 3.3.1.1 Description of the Post-Processor Curve-Fitting Operation

This section describes the method used to extract the Doppler and delay parameters from the deconvolution outputs. The curve-fitting operation is performed only on the axis parallel to the Doppler axis. The purpose of the operation is twofold: i.) the curve-fitter eliminates data from the deconvolution output that do not conform to the response predicted by (3.42), and ii.) the curve-fitter extracts Doppler and amplitude estimates at time delays where the data does conform to (3.42).

If the extent of observation is  $C$  time samples, and if the deconvolution algorithm is performed at  $R$  different Doppler shifts, the resultant POCS output matrix will be an  $R$  rows by  $C$  columns matrix. The *post hoc* curve-fitter that was used to obtain the results that are shown in the figures fits the curve described by equation (3.42b) in section 3.2.3 to each column (*i.e.*, each slice of time parallel to the Doppler axis). Instead of calculating the auto-ambiguity function for the transmitted signal, however an approximation is made in our simplistic curve-fitter which assumes that the envelope of the auto-ambiguity function has the  $\sin(x)/x$  shape in the Doppler dimension (see [29]). This approximation is made only to

simplify the code for the curve-fitter. If one so desired, a more accurate curve-fitter could be obtained by using actual samples of the auto-ambiguity function obtained from, for example, a look-up table. The data on each column are normalized by the maximum value on each column. A sum-square-error (SSE) is obtained for each column, given by

$$SSE(\tau_k) = \sum_{\omega_D} \left| \hat{c}(\tau_k, \omega_{D_i}) - \left[ \left( \frac{BW}{2\pi} \right) \left| \frac{\sin\left(\frac{N}{2}(\omega_{D_i} - \omega_{D_{\max\_of\_column}})\right)}{\left(\frac{N}{2}(\omega_{D_i} - \omega_{D_{\max\_of\_column}})\right)} \right| + \left(1 - \frac{BW}{2\pi}\right) \cos\left(\frac{N}{2}(\omega_{D_i} - \omega_{D_{\max\_of\_column}})\right) \right] \right|^2, \quad (3.47)$$

where  $\omega_{D_{\max\_of\_column}}$  is the Doppler location of the maximum deconvolution output at a given time delay (column),  $\hat{c}(\tau_k, \omega_{D_i})$  is the channel estimate at delay  $\tau_k$  for all supported Doppler shifts, and  $BW, N$ , and  $\omega_D$  are as given in (3.1), (3.2), and (3.40). If this error exceeds a preset threshold (this threshold can be manually set *a priori*, or an algorithm can be devised which chooses a threshold based on the input SNR; in our plots, the value of the threshold was manually chosen before the curve-fitting operation), the curve-fitter rejects the data along the Doppler axis at that time delay, and the output will show zero values for the entire column (all the Doppler values at this time delay). If the value of the SSE does not exceed the preset threshold, the curve-fitter locates the Doppler shift value at which the deconvolution output response is greatest and, in keeping with (3.42b), this Doppler shift value and the amplitude of the deconvolution output at this Doppler shift value are saved as the multipath parameter estimates at that particular time delay.

The procedure described above estimates the time, Doppler, and delay

parameters of the multipath channel demonstrates the validity of (3.42). Note, however, that the algorithm assumes that only one multipath component can be present at any given delay value, so that if two multipath components having different Doppler shift values are present at the same time delay (a situation that, by nature, is short-lived), our simple algorithm will reject one or both of the components.

### 3.3.2 Least Squares Estimation Applied to Doppler Multipath

The results of section 3.2 are generally applicable to all deconvolution procedures. This section —which is due in part to the work of Zoran Mitrovski, coauthor of [57,66]— outlines the constrained least-squares (LS) estimation approach [54,62] as a means of deconvolution in the Doppler multipath environment and shows, again, that the implications of (3.42) are accurate and useful in a determination of the channel parameters. As will be elaborated below, the method of LS differs fundamentally from the method of POCS, described above. Yet, both —in the limit— reduce to inverse filtering, and can therefore benefit from the discussion of section 3.2.

In the zero-Doppler case, the equation describing the multipath channel, (3.1), can be written in matrix form,

$$\mathbf{y} = \mathbf{X}\mathbf{c} + \mathbf{n}, \quad (3.48)$$

where the vectors  $\mathbf{y}$ ,  $\mathbf{c}$ , and  $\mathbf{n}$  represent the received signal, the channel response, and the additive channel noise and correspond directly to  $y(t)$ ,  $c(t)$ , and  $n(t)$  as given in (3.1) and (3.3), and  $\mathbf{X}$  is a circulant matrix formed from the sampled transmitted signal,  $x(t)$ . Equivalence between linear and discrete-time circular convolution is achieved by zero padding  $\mathbf{y}$ ,  $\mathbf{x}$ ,  $\mathbf{c}$ , and  $\mathbf{n}$  to the appropriate length,  $L$ .

When the desired information of the channel under consideration is chiefly found in the larger amplitude specular reflections and not in the lower amplitude clutter, a constraint can be developed which limits the purpose of the deconvolution procedure to that of searching for these larger specular reflections. A means of implementing this constraint is to define a vector  $\mathbf{s}$ , which contains only zeros and ones, and to allow for non-zero elements of the estimate of  $\mathbf{c}$  to exist only at the non-zero elements of  $\mathbf{s}$ . The delay values covered by the non-zero elements of  $\mathbf{s}$  correspond to a domain on the delay axis and are referred to as the *indicator set*.

An appropriate indicator set may, for some pulse-compression type waveforms, be found by passing the received signal through a matched filter and thresholding the result with a preselected constant [62]. Alternatively, the LS output itself could be thresholded with a preselected constant, and the resulting indicator set could be applied to a second LS iteration. In either case, the final LS estimate is obtained via

$$\mathbf{c}_s = (\mathbf{X}_s^T \mathbf{X}_s)^{-1} \mathbf{X}_s^T \mathbf{y}, \quad (3.49)$$

where  $\mathbf{X}_s = \mathbf{X} \mathbf{I}_s$ ,  $\mathbf{I}_s$  is an  $L \times p$  matrix ( $p$  being the number of ones in the vector  $\mathbf{s}$ ),

and where the columns of  $\mathbf{I}_s$  have all zeros except one unity value at the row index equal to the index of the corresponding element in  $s$ . The property of the discrete Fourier transform (DFT) to diagonalize circulant matrices [67] may be used to significantly reduce the memory consumption and computational time involved in the evaluation of the matrix equation in (3.49).

In the noiseless case, the LS estimator becomes a simple inverse filter. Thus, the LS estimation procedure can be incorporated into a Doppler multipath parameter estimation system (see again Figure 3.2) in the same manner as was done for POCS, above. Following the LS estimation procedure, the channel estimate undergoes post-processing. This can be a simple peak-finder algorithm or a more sophisticated curve-fitting procedure designed to eliminate spurious peaks in the final estimate, the latter being based on the inherent properties of the outputs of deconvolution based Doppler/delay estimation algorithms, as discussed in section 3.2.

Results are given in Figure 3.10 for the same input signal, SNR, and simulated channel as was used for Figure 3.8. Figure 3.10b shows the final output for the case when the curve-fitting procedure is used. Note that the curve-fitting procedure based on (3.42b) is able to both accurately resolve the Doppler/delay parameters and to reject the spurious, non-target related artifacts. A simple peak-finding algorithm would not, for example, have rejected the artifact at  $\tau = 123$  in Figure 3.10, but the curve-fitting procedure that is based on (3.42b) correctly rejects the artifact.

A comparison of Figure 3.8 with Figure 3.10 reveals that the LS estimation procedure was able to produce a more accurate channel estimate than was produced

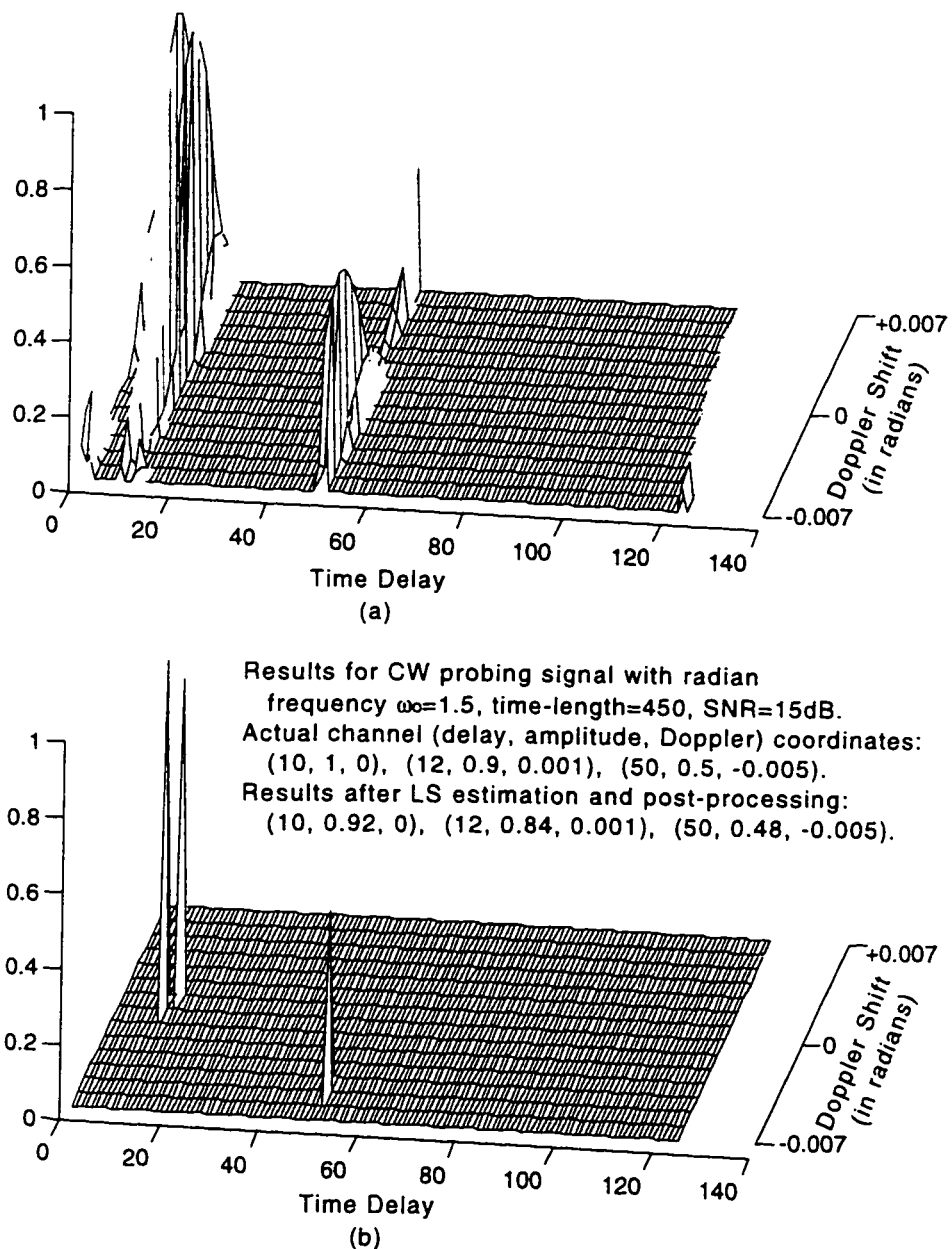


**Figure 3.10** (a) shows the output of a deconvolution system based on least-squares (LS) estimation. (b) shows the final output after post-processing, which relies on the result given in equation (3.42), has been applied to the LS output. Note that, in this case, the post-processing was able to reject all of the noise-related artifacts.

by the POCS method. One would expect LS to perform in a manner that is superior to POCS for the following reason. The output of POCS is the result of several projection operators that manipulate the channel estimate and force the resulting estimate to belong to a set *known to contain* the true estimate. The output of LS is the result of solving a set of linear equations, where the solution to this set of equations is *optimum* in the least squares sense. In this respect, the channel estimate produced via LS is equivalent to the channel estimate produced by POCS when POCS uses the lowest possible bound,  $B_v$ , in (3.45) (see also [62]). Since LS possesses this inherent optimization which POCS lacks, one may expect the estimates produced by LS to be more robust than those produced by POCS. The experimental results that we have observed confirm this expectation. We have found that, while POCS is generally useful for applications where the input SNR is greater than ten to fifteen dB, the LS procedure is useful for input SNRs down to zero dB. The LS procedure, thus, produces better channel estimates than the POCS procedure and does so in a manner that is more computationally efficient than POCS. The generally superior and computationally efficient results of the LS estimation procedure come at the cost of consuming more memory in the processing unit of the system.

The performance of the LS estimation procedure used in tandem with the post-processing technique based on the derived Doppler response of an inverse filter—as summarized by equation (3.42)—is shown in Figure 3.11 for received signal-to-noise ratios ranging from -20 dB to 20 dB (additive zero-mean white Gaussian noise). Three different probing waveforms were used to generate the data in Figure

3.11: a linear FM sweep (*chirp* in the figure), a windowed sinusoidal (*CW* in the figure), and a linear congruence frequency hop code (*FHOP* in the figure) [26]. All three signals have sampled time length of  $N = 400$  samples, and the bandwidth of the chirp and frequency hop waveforms is identical and equal to  $\pi/4$  radians (8X

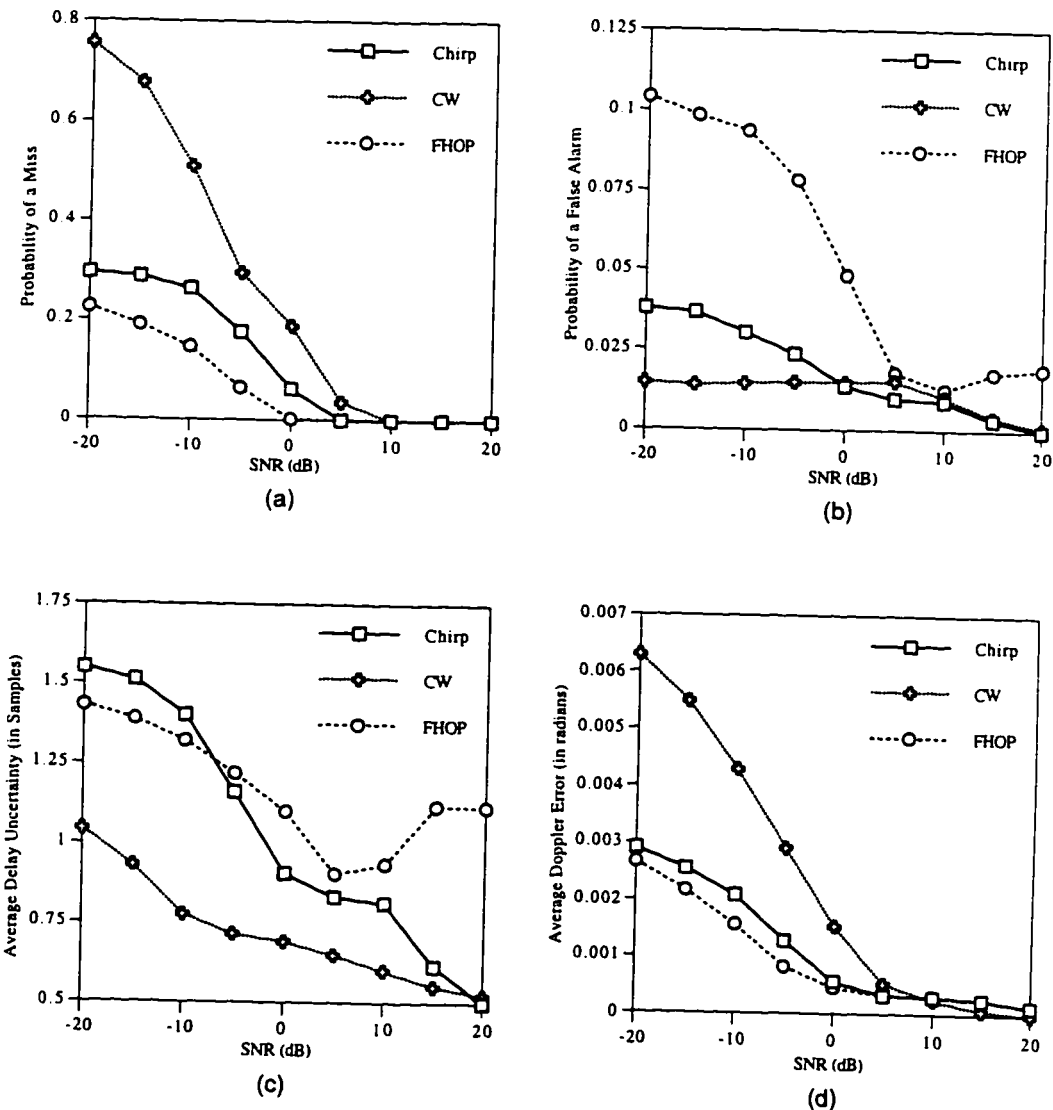


**Figure 3.11** Performance of the least squares (LS) deconvolution procedure in the presence of noise and Doppler. (a) Probability of a miss as a function of input SNR. (b) Probability of a false alarm as a function of input SNR. (c) Average delay uncertainty as a function of input SNR. (d) Average Doppler error as a function of input SNR.

oversampled). Each data point on the plots is derived from the results of one thousand simulation runs, where each run tested sixty different delay hypotheses, and an average of three actual multipath components were present in each simulation run, with each multipath component having a unique Doppler shift and delay offset. The receiver in the simulations was not given knowledge of the received SNR or the number and positions of the multipath components.

As the estimator was not set up to interpolate between received samples, the best delay resolution achievable in the simulations is  $\pm 0.5$  samples. This optimum value was achieved or nearly achieved at high SNR values by both the system that employed the CW waveform and that which used the chirp as a probing waveform.

The non-monotonicity of the plot of Average Delay Uncertainty and of the plot of Probability of a False Alarm for the system that used the FHOP probing waveform is a result of weak signal-related artifacts. These artifacts survive the deconvolution process and are close enough to the expected shape dictated by (3.42) that they also survive the post-processing curve fitting operation at high SNRs. At lower SNRs, these signal-related artifacts are more severely masked by the noise and are eliminated from the final estimate, thus giving the impression that the system performs better with moderate noise than with very small amounts of noise.

If the carrier frequency is assumed to be 5 GHz and the sampling frequency and signal bandwidth are assumed to be 10 Msps and 1.25 MHz, respectively, then the average magnitude of the Doppler error in Figure 3.11d can be converted to velocity error. The relation is 0.001 radian Doppler error equates to approximately

96 meters / second velocity error.

The plots of Figure 3.11 bring to light some interesting results. Note that the CW waveform performs poorly compared to the chirp waveform in the plot of Average Doppler Error and that the CW system outperforms the chirp system in terms of Average Delay Uncertainty. In a correlation-based estimator, one would expect the CW pulse to give a much better Doppler estimate than the chirp, which is prone to range-Doppler coupling, and a much poorer delay estimate than the chirp, since the chirp has inherent pulse-compression properties. These plots confirm the analysis of section 3.2, which concludes that the waveform auto-ambiguity function is not the only indicator of detection properties for a deconvolution-based Doppler-delay estimator.

### 3.3.3 A Word About Resolution

It is well known that, in the absence of Doppler, deconvolution methods are able to resolve multipath parameters to within one sampling interval (see, for example, [44] and the references therein). It follows that the deconvolution processor that is centered at the Doppler shift equal to that of a particular multipath component will produce the same resolution at the output of that deconvolution block. The curve-fitting operation described above will reject those time delay values that do not conform to (3.42b) and accept those that do conform to (3.42b).

According to (3.42), the response along the Doppler axis at the time delay value

where a multipath components exists will have a distinctive shape that is based on the properly weighted summation of the auto-ambiguity function and the cosine effect. The estimation properties of the Doppler parameters may be qualitatively related to the main lobe width in the Doppler direction of the deconvolution output response. Since the main lobe width of the summation of the auto-ambiguity function and the cosine effect is not significantly different from the main lobe width of the auto-ambiguity function alone (see [29,34] and compare to (3.42)), the Doppler estimation properties of the deconvolution-based multipath parameter estimation systems described in this chapter will be comparable to those of a correlation-based system, while time delay estimation may be improved, due to the deconvolution that takes place in the delay dimension.

### 3.4 Discussion and Conclusions

A number of deconvolution algorithms exist and have been applied to the problem of multipath parameter estimation. Each such algorithm, either directly or in an asymptotic sense, forms an inverse operator and, thus, approximates the function of an inverse filter. Based on this premise, it was shown that, where the narrowband approximation is satisfied, the output of a deconvolution-based multipath parameter estimation system is characterized by the weighted summation of two signal-related functions. The two functions were shown to be the probing signal's auto-ambiguity function and a function that was called by the name "cosine effect" due to the

predictable oscillations that it exhibits parallel to the Doppler axis when well-behaved probing signals are employed. Experimental results based on two known deconvolution methods, POCS and LS, were also presented, both verifying and utilizing the aforementioned derivation.

The derived results, as summarized in equation (3.42), lead to the following conclusions regarding signal design and receiver implementation issues as they pertain to multipath parameter estimation in the presence of Doppler.

- 1.) Because the probing signal's auto-ambiguity function contributes to the total deconvolution output, it is desirable to employ a probing signal which has an auto-ambiguity function with uniformly low sidelobes —that is, the classical thumbtack ambiguity function [28,29,34]. Such a signal would ensure that sidelobe interaction between the various received multipath components would not, through a shift in the output peaks in either the Doppler or delay dimensions, add inaccuracies to the parameter estimates.
- 2.) The contribution of the cosine effect to the total deconvolution output can be emphasized over the contribution of the auto-ambiguity effect —which is prone to range-Doppler coupling and sidelobe interaction— through an increase in the system sampling rate. Thus, even for signals with poor ambiguity properties, the accuracy of the delay and Doppler estimates may be improved by increasing the system sampling rate; ergo, increased accuracy may be obtained at the cost of increased computational complexity.

For signals that have abrupt phase jumps in the region of flat bandwidth

—hitherto labeled as signals that are *not well-behaved*—, the spectral skirts may complicate the parameter estimation procedure through the introduction of inverse filter artifacts in the final estimate. For such signals that are not well-behaved, the adverse effects of the spectral skirts on the parameter estimate can be lessened by a decrease in the system sampling rate.

3.) A surprising result of the analysis leading to (3.42) is that a CW pulse (windowed sinusoid) is actually a good signal for use in a deconvolution-based multipath parameter estimator. Because the effective bandwidth of the CW pulse is zero, the contribution of the ambiguity function is absent from the deconvolution output ( $\beta = 0$ ) . Only the cosine effect, which is well behaved and has significant energy only on the Doppler axis, is present. Thus, there are no ambiguity sidelobes about which to be concerned, and the derived form of the cosine effect (3.42) can be used as part of a post-processing procedure which extracts an accurate estimate of both the Doppler and delay parameters from the output of the deconvolution system.

4.) The derived results show that, within a Doppler multipath environment, deconvolution methods are able to resolve multipath component delay parameters to within one sample period and Doppler shift parameters to within a fraction of the inverse of the time-length of the transmitted waveform; that is, the delay estimation accuracy of deconvolution-based multipath estimators can, at the cost of increased computational complexity, significantly exceed the accuracy of correlation methods, while Doppler resolution is comparable to correlation methods. Thus, for applications such as radar or sonar, the analyses show that deconvolution is a

plausible means of delay and Doppler estimation.

For an application such as cellular mobile radio, which seeks the time delay parameters only, the analyses show that deconvolution is tolerant to small Doppler shifts in the received multipath components. This is because the cosine effect, for the small Doppler shifts experienced in the context of cellular mobile radio, is approximately constant in the Doppler dimension. Hence, accurate multipath delay estimates can be made using deconvolution methods despite small Doppler shifts.

Furthermore, though Doppler is not a desired parameter in all multipath estimators, the additional information provided by examining the outputs of Doppler-shifted deconvolution blocks can be used to produce more accurate time delay estimates. This is because the shape of the function parallel to the Doppler axis at a given delay will have a shape as dictated by (3.42) if a multipath component truly exists at that delay. Thus (3.42) can be incorporated as an additional constraint into a POCS-type algorithm or used as *post hoc* means of cleaning up the spurious artifacts of the output data from any deconvolution-based parameter estimation system.

# Chapter 4 Analysis of Low-Power Matched Filter Structures for Asynchronous CDMA Receivers

---

The types of circuits in which analog design techniques are employed typically differ from those in which digital design methods are used, with analog circuits being commonly applied to high speed, low precision functional blocks such as mixers and RF modulators, while digital circuits are chosen for high precision, high complexity blocks that operate at frequencies well below the  $f_T$  of the transistors from which the circuits are comprised. Yet there still exist applications for which the superior circuit implementation—analog or digital—is unclear. The recent birth of commercial interest in spread-spectrum communications provides the motivation for investigating one such application, that of the parallel programmable matched filter.

In this chapter, analog and digital circuit realizations of a parallel programmable matched filter are examined. Through wide variations of the design space parameters, the general trend that is observed is that short, fast circuits tend to favor an analog implementation, while longer, slower circuits make a digital implementation more

appropriate. A methodology is provided for choosing the preferable circuit-implementing technology when power consumption—as a function of data precision, filter length, operating frequency, technology scaling, and the maturity of the fabrication process—is used as the primary metric of comparison. It is shown that neither the analog nor the digital matched filter implementation is universally more power efficient than the other. Rather, a surface is mapped in the multidimensional design space where, on one side of this surface, a digital solution is preferable, while on the other side of the surface, an analog circuit is appropriate. Equations are given which delineate the position of this transitional surface in terms of the design space parameters, and example calculations and plots depicting the regions of dominance for the digital and analog matched filters for specific process and system parameters are provided.

## 4.1 Introduction

The time frame over which groups and individuals have debated whether digital or analog circuit techniques should be used to realize a given functional block can be measured in decades. For many functions, the debate has been settled for quite some time. There is not much question, for example, that digital is the preferred circuit implementation for a multiplier with precision equivalent to 64 bits, nor is there much question that analog is the proper choice for a 2 GHz RF modulator/upbander.

Functions still exist, however, for which the choice between a digital or an analog circuit implementation is unclear. Recent commercial interest in spread-spectrum systems for wireless data networks [5,31,69] provides motivation for evaluating one of these remaining areas, that of programmable parallel matched filters.

In the discussion that follows, two different CMOS realizations of a programmable parallel matched filter—one digital and one analog—are evaluated and compared in order to determine the most appropriate circuit-implementing technology for use in commercial spread-spectrum communication systems. Throughout this chapter, power consumption—as a function of data precision, filter length, operating frequency, technology scaling, and the maturity of the fabrication process—is used as the primary metric of comparison. In section 4.2 of this chapter, the function and utility of matched filters are reviewed. In section 4.3, a low-power digital matched filter is presented and analyzed, while in section 4.4 the same is done for an analog matched filter. In section 4.5, the analog and digital implementations are compared, and a unified result is presented that shows under which set of conditions the digital solution is superior to the analog solution, and vice versa. Lastly, the conclusions of the chapter are found in section 4.6.

## 4.2 A Review of Matched Filters

The sole purpose of a matched filter is to monitor the communication channel for a preselected waveform, say  $s(t)$ . The matched filter is in fact a finite impulse

response (FIR) filter with a system response that is a time reversed replica of the waveform that is to be detected. If the preselected waveform is present in the data that are input to the matched filter, the matched filter will compress most of the energy of that waveform into a small slot of time, allowing signal detection —even in the presence of large amounts of noise— to be performed by thresholding the matched filter output (see Figure 4.1). For an additive white gaussian noise channel, the matched filter is the ideal receiver, and it can be shown that the signal-to-noise ratio (SNR) is improved by a factor that is proportional to the time-bandwidth product of the transmitted waveform [1,34,70,71]. That is

$$SNR_{OUT} = SNR_{IN} \cdot TW, \quad (4.1)$$

where  $T$  is the time-length and  $W$  is the one-sided bandwidth of the transmitted signal.

In addition to noise rejection, the matched filter is able to select one out of many signals simultaneously transmitted over the same channel and within the same spectrum allocation, provided the signals are designed to have small cross-correlation values with respect to each other [1,18,26]. The ability of the matched filter to compress the energy of the signal into a small time slot permits the utilization of energy from multiple signal reflections (*e.g.*, from the line-of-sight path, and reflections from buildings and/or geographical features) to be combined for a further increase in output SNR. In existing non-spread-spectrum mobile radio systems, this multipath effect is not exploited and, in fact, results in signal degradation through Rayleigh fading. Proposed

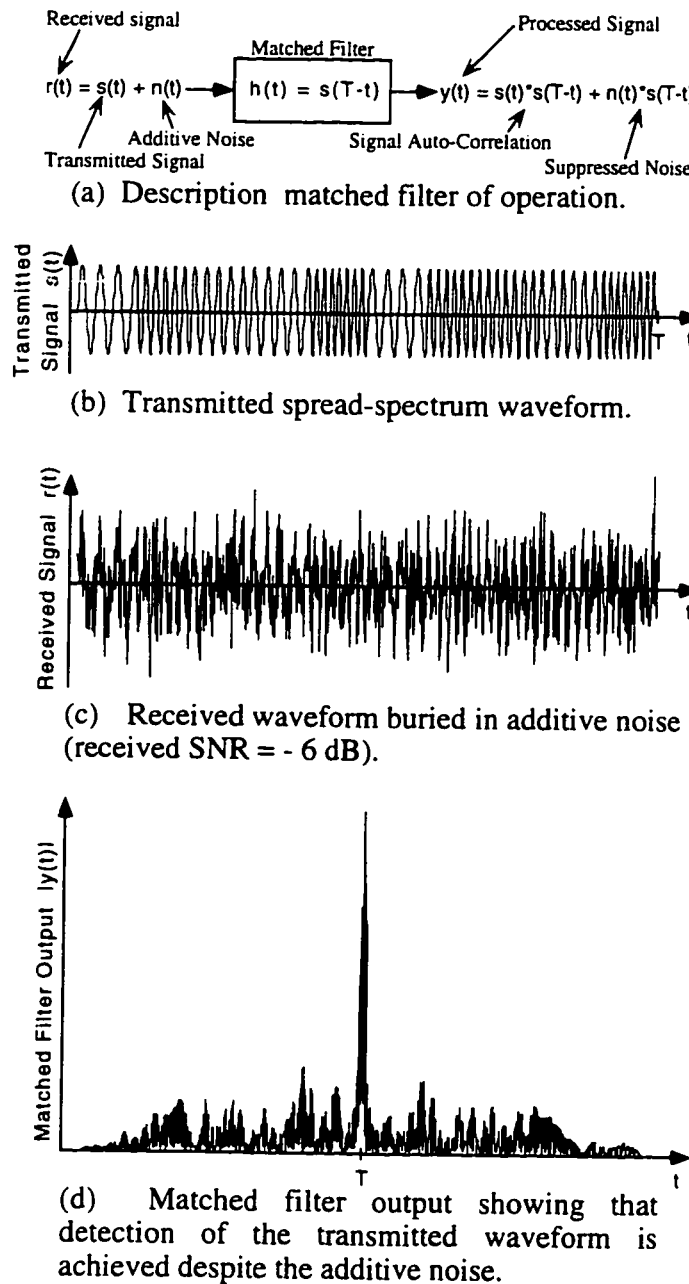


**Figure 4.1** The utility of a matched filter in a communications environment is shown in (a) through (d). The matched filter can pluck a pulse-compression spread-spectrum signal (in this case a hyperbolic-congruence frequency-hop code [25]) out of a noisy channel by concentrating the energy of the signal into a small time slot around  $t = T$ .

spread-spectrum CDMA systems use multipath reflections as diversity branches, combining energy from the multipath branches using a multi-fingered *rake receiver* in conjunction with the matched filter or correlator [4,6,31,69]. Thus, transmitted signal energy that is normally lost or that normally causes self-interference and fading is used to improve signal quality.

In the past, most of the interest in spread-spectrum systems has been confined to military applications and satellite communications. Within the past several years, however, commercial systems have been proposed and implemented which exploit desirable spread-spectrum characteristics such as immunity to the fading effects of multipath, ease of multiple-access overlay, and the ability to transmit at lower radiated power levels [4-6,31,69]. A birth of interest in spread-spectrum communication systems targeted to commercial applications has occurred and is due in part to the steady advances in high density semiconductor fabrication technologies, which allow the complex modulate and demodulate functions of the spread-spectrum transceivers to be realized while still meeting the size, cost, and power budgets imposed by the consumer marketplace.

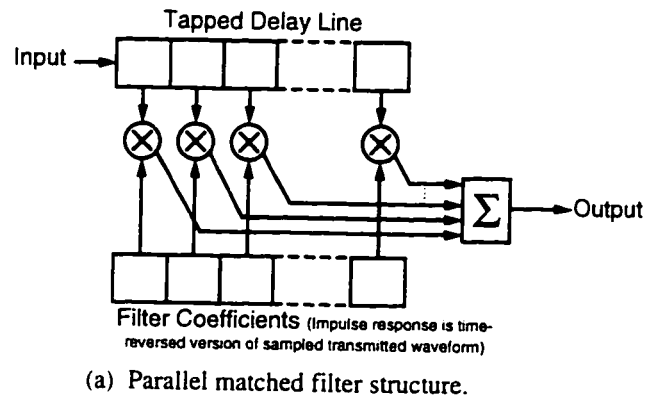
A matched filter [70,72] is an integral part of an asynchronous spread-spectrum communication receiver or range-finding device and may be used to shorten search and synchronization times within receivers of *long code* systems [5,73,74], such as the CDMA cellular proposal, IS-95 [8]. Many evolving areas of commercial use employ portable communication terminals with limited power sources. Thus, low-power transmitters and receivers are required if spread-spectrum systems are to become

commercially viable. Though the generation and transmission of spread-spectrum signals is well understood and can be realized by technologies which consume relatively small amounts of power [1,18], the receivers for these systems —including the matched filter block— are considerably more complex [5,7,32], and, thus, work is ongoing to develop practical lower-power devices.

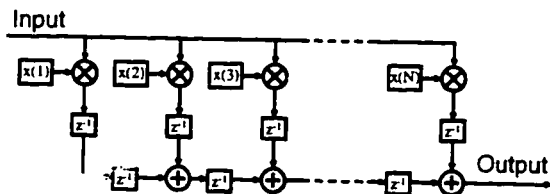
The matched filter block (shown in Figure 4.2a) of a radio occupies a place between the RF input circuitry and the digital data processing circuitry. As such, the conversion from analog to digital can take place either just before the matched filter input or just after its output, leaving the designer with the freedom to implement the most suitable matched filter in either analog or digital circuitry.

The analysis that follows compares digital and analog integrated circuit implementations of programmable parallel matched filters, using power consumption as the primary metric of comparison. The qualifier *programmable* is an important one, and it is used here to mean: 1) the sampling frequency can be changed to accommodate various data rates, and 2) the stored coefficients of the tapped delay line can be changed by an external microcontroller or memory. These design constraints allow maximum flexibility of the portable receiver and make it suitable for multimedia applications where, for example, voice or text information may be transmitted over the same channel at different bit rates.

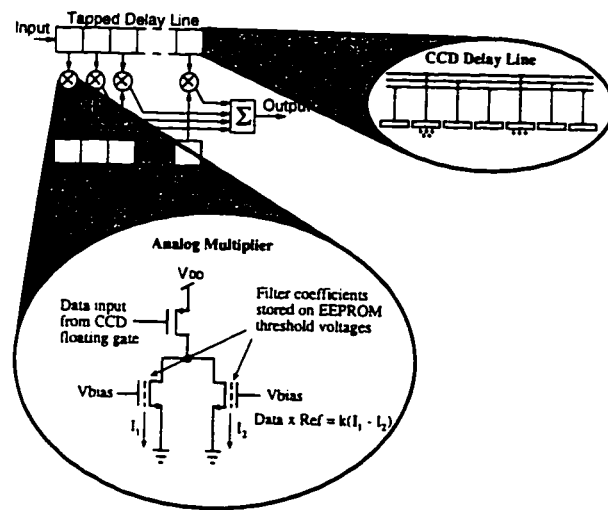
### 4.3 A Digital Matched Filter Implementation



(a) Parallel matched filter structure.



(b) Digital matched filter architecture.



(c) Analog matched filter architecture.

**Figure 4.2** The block diagram of the parallel matched filter structure is shown in (a). The digital and analog circuit implementations are outlined in (b) and (c), respectively.

Within this section, a low-power digital matched filter is presented and analyzed. The issues associated with quantization levels, specifically as these levels relate to the digital matched filter, are discussed in section 4.3.1. A discussion of the primary subcircuits of the digital matched filter —the multipliers, adders, and registers—is presented in section 4.3.2. A power estimate of the digital matched filter is formulated in section 4.3.3.

#### 4.3.1. Data and Reference Quantization Levels

A parallel matched filter is identical in structure to a FIR tapped delay line filter. The function of the matched filter, however, permits some of the constraints associated with the FIR filter to be relaxed. The FIR filter requires precise representation of the input data and stored tap coefficients in order to suppress the spectral components within the *stopband* areas of the filter frequency response. This required precision often calls for a data representation of eight bits, ten bits, or greater [75,76].

The parallel matched filter does not, however, rely on the precision of the stored coefficients as strongly as the FIR filter. The sign (positive or negative) of the result of each of the  $N$  multiplications (where  $N$  is the sampled time-length of the transmitted signal) in the parallel structure carries most of the desired information. Turin [70] has used this property as the basis for a discussion of all-digital matched filters which represent both data and reference with only one bit ( $\pm 1$ ). Degradation in matched filter performance accompanies this coarse level of quantization [76], but, due

to the inherent processing gain of spread-spectrum systems, such degradation may be tolerable for some applications given the dramatic reduction in hardware costs. In practice, higher quantization levels may be used (typically up to approximately six bits) to accommodate chirp-type waveforms or continuous-phase fast-frequency-hop codes, or to compensate for an imperfect automatic-gain-control (AGC) amplifier at the receiver input. In the discussion that follows, the quantization levels of the input data and stored reference coefficients are used as design parameters.

#### 4.3.2. Digital Matched Filter Subcircuits

The digital programmable parallel matched filter structure that is used in this analysis is pictured in block diagram form in Figure 4.2b. The operation of the filter is such that each new input data sample appears simultaneously at the input of each multiplier block. After multiplication with the  $N$  stored reference coefficients, the partial sums of products are shifted one cell to the right during each clock cycle, with the final sum at the bottom right being the desired matched filter output. This structure is commonly used in FIR filters (*e.g.*, [77]) and has several advantages over a direct implementation of Figure 4.2a, such as ease of layout and no need for a single large adder to generate the output result.

The power consumption of the digital matched filter can be estimated by summing the contribution of the major functional blocks: the registers, adders, and multipliers. In the following analysis, it is assumed that the dynamic charging and

discharging of the inherent circuit capacitances is the primary contributor to the total circuit power consumption. The total circuit power may therefore be estimated by computing or measuring the effective switched capacitance of each of the major logic blocks and calculating the familiar  $CV^2f$  dynamic power dissipation. However, in the spirit of [78], supply voltage can vary as a function of operating frequency and quantization level. A single supply voltage is assumed for the entire matched filter chip, with the value for  $V_{DD}$  determined by the speed requirements of the most performance-limiting circuit elements, the multipliers.

For data and reference quantization level,  $Q_d$  and  $Q_r$ , respectively, exceeding two to three bits each, the multiplier block is the most complex of the subcircuits of the digital matched filter, and as such it exhibits the longest delay between registers. When a single supply voltage  $V_{DD}$  is used for the entire integrated circuit (IC), the multiplier block defines the minimum supply voltage that is required by the IC to meet the operating frequency specifications. In general, the basic  $m$ -bit multiplier consists of an  $m \times (m-1)$  array of adders. For a straightforward array implementation, the multiplier speed decreases nearly linearly with increasing  $m$ .

A number of schemes have been proposed that reduce the delay and/or the power required to implement the multiplication operation in digital circuitry. For a discussion of these schemes, the reader is referred to [79] and the references therein. A noteworthy result shown by the analysis of [79] is that, for multipliers with  $m$  less than eight bits, there is little difference—in terms of power and worst case delay—between the straightforward array implementation and the various *recoded* multiplier

schemes. Because of this characteristic, and because the parallel matched filter uses word sizes smaller than eight bits in width, the choice of multiplier architecture is not critical for these applications, and array-type multipliers are assumed in the power analysis for the remainder of the chapter.

The adder blocks within the matched filter also consume a sizable fraction of the total IC power. Reference [80] contains a comparison of six of the most common adder types. In this comparison, there is significant differences in the worst case delay among the adder types, even at bit widths as small as 16 bits, with a carry lookahead adder exhibiting a delay less than one third of that exhibited by a ripple carry adder. Yet, at a fixed supply voltage and operating frequency, the ripple carry adder consume 25-30% less power. Note again that for  $Q_d$  greater than one or two bits, the multiplier blocks of the matched filter set the critical delay and, therefore, the power supply voltage level. This means that, as long as the chosen adder architecture can add two numbers in less time than is required to multiply two numbers, the most power efficient adder should be used, irrespective of the worst case delay. Hence, for the pipelined partial sum adders shown at the bottom of the structure in Figure 4.2b, simple ripple carry adders can be used.

Finally, static CMOS implementations of the multipliers, adders, and registers are assumed throughout the analysis. This assumption is made since, for a given technology, static logic design techniques facilitate a greater degree of voltage scaling than dynamic logic techniques.

### 4.3.3. Power Estimate of the Digital Matched Filter

From [78], an estimate of gate propagation delay  $T_d$  is given as a function of supply voltage  $V_{DD}$ , threshold voltage  $V_T$ , load capacitance  $C_L$ , oxide capacitance per unit area  $C_{ox}$ , electron mobility  $\mu$ , and the CMOS gate width-to-length ratio  $W/L$ :

$$T_d \equiv \frac{C_L}{\mu C_{ox} W/L} \cdot \frac{V_{DD}}{(V_{DD} - V_T)^2}. \quad (4.2)$$

Also, for a given technology, the time required to complete a  $Q_d$  bit  $\times$   $Q_r$  bit multiplication can be approximated as [81,82]

$$T_{\text{multiply}} \equiv M(Q_d + Q_r - 1), \quad (4.3)$$

where  $M$  is the delay of a one-bit adder in units of seconds/bit, and  $Q_d$  and  $Q_r$  are the level of data and reference quantization, respectively.

Combining (4.2) and (4.3) gives

$$T_{\text{multiply}} \equiv K_d(Q_d + Q_r - 1) \cdot \frac{V_{DD}}{(V_{DD} - V_T)^2}, \quad (4.4)$$

where  $\frac{C_L}{\mu C_{ox} W/L}$  and  $M$  have been merged to form the parameter  $K_d$ , a technology dependent constant with units of volt  $\cdot$  seconds / bit.

The value of  $V_{DD}$  that is derived from (4.4) can be used to estimate the total power consumption of a digital multiplier,

$$P_{\text{multiply}} \equiv \frac{K_p Q_d (Q_r - 1)}{T_{\text{multiply}}} \left[ \frac{1}{2} \left( \beta + \sqrt{\beta^2 - 4V_T^2} \right) \right]^2, \quad (4.5)$$

where  $\beta = 2V_T + \frac{K_d (Q_d + Q_r - 1)}{T_{\text{multiply}}}$ ,

and  $K_p$  is a technology dependent constant with units of farads / bit<sup>2</sup>.

The total power consumption of the digital matched filter is

$$P_{\text{DMF}} \equiv NP_{\text{multiply}} + AC_{\text{adder}} V_{DD}^2 f_{\text{clk}} + RC_{\text{register}} V_{DD}^2 f_{\text{clk}}, \quad (4.6)$$

where  $N = 2^k$  is the number of filter taps,  $f_{\text{clk}}$  is the operating frequency of the matched filter,  $C_{\text{adder}}$  and  $C_{\text{register}}$  are the effective switched capacitance of the full adders and one-bit registers, respectively, and  $A$  and  $R$  are the number of full adders and one-bit registers in the digital matched filter, respectively, as given by

$$A = (2^K - 1)(Q_d + Q_r) - K + \sum_{m=1}^{K-1} (m2^m)$$

and  $R = 2^{K+1}(Q_d + Q_r) - (2^K + 1) + \sum_{m=1}^{K-1} (m2^m)$ .

In the ensuing plots, the following values are assumed for a 2.0  $\mu\text{m}$  CMOS process:

$$V_T = 1.0 \text{ volt},$$

$$K_p = 1.5 \text{ pF / bit}^2,$$

$$K_d = 10^{-8} \text{ volt} \cdot \text{sec / bit},$$

$$C_{\text{register}} = 250 \text{ fF, and}$$

$$C_{\text{adder}} = 600 \text{ fF.}$$

The choice of implementing technology has an enormous effect on the power consumption of the digital matched filter. Assuming the operating frequency requirements of the matched filter can be satisfied by a particular technology, the supply voltage in the scaled technology can be decreased to realize additional power savings [78] beyond those that are achievable by a direct application of classical scaling rules [83,84]. The reduction in power dissipation depends upon the degree of technology scaling (represented by the scaling constant  $\kappa$  [83]) and the ratio of the threshold voltage to the supply voltage in the unscaled technology,

$$\rho = \frac{V_{T_{\text{unscaled}}}}{V_{DD_{\text{unscaled}}}}. \quad (4.7)$$

The power scaling constant, which is defined in this work as  $S_{C_E}$ , is

$$S_{C_E} = \frac{1}{\kappa^3} \left( \rho + \frac{(1-\rho)^2}{2\kappa} + \frac{(1-\rho)}{2} \sqrt{\frac{4\rho}{\kappa} + \left( \frac{1-\rho}{\kappa} \right)^2} \right)^2, \quad (4.8)$$

or

$$S_{C_{CVR}} = \frac{1}{\kappa} \left( \rho + \frac{(1-\rho)^2}{2\kappa^2} + \frac{(1-\rho)}{2\kappa} \sqrt{4 - \left( \frac{1-\rho}{\kappa} \right)^2} \right)^2. \quad (4.9)$$

$S_{C_E}$  is applicable assuming ideal constant electric field scaling [83].  $S_{C_{CVR}}$  is applicable assuming the threshold voltage does not scale with the other device parameters. The current industry trend lies somewhere between these two schemes, as shown in Figure 4.3.

Applying (4.8) and (4.9) to (4.6) yields an estimate of the power consumption of a digital matched filter as a function of operating frequency, quantization level, filter length (number of taps), and technology scaling.

$$P_{DMF_{CE}} \cong S_{C_{CE}} P_{DMF}, \quad (4.10a)$$

or

$$P_{DMF_{CVT}} \cong S_{C_{CVT}} P_{DMF}, \quad (4.10b)$$

depending on which scaling procedure is used to shrink the device dimensions and operating voltages.

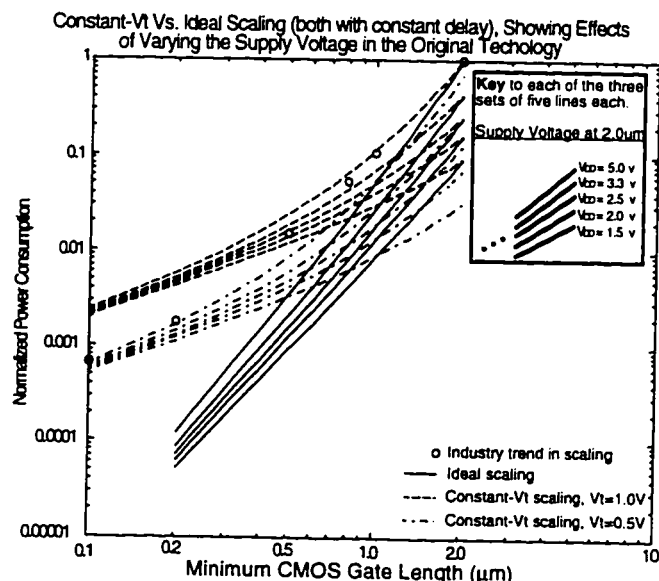


**Figure 4.3** Effects of technology scaling on digital circuit power consumption.

## 4.4 An Analog Matched Filter Implementation

In this section, a low-power analog matched filter is presented and analyzed. A

discussion of the primary subcircuits of the analog matched filter is presented in section 4.4.1, and a power estimate for the analog circuit is formulated and given in section 4.4.2.

#### 4.4.1. Analog Matched Filter Subcircuits

The tapped delay line that is required by the parallel matched filter that is shown in Figure 4.2a can be implemented in analog form via a number of circuit techniques, including bucket-brigade devices (BBDs), surface acoustic wave (SAW) devices, and charge-coupled devices (CCDs). The BBDs are generally inferior to CCDs in terms of power expenditure for a given level of signal integrity [85]. SAW devices do not lend themselves well to programmability of both the sampling rate and the filter tap weights [86,87]. In addition, the physical size of SAW devices is strongly dependent upon the time-length of the signal to which the filter is matched (requiring approximately 3 mm of piezoelectric substrate per  $\mu$ s of signal length), making the SAW size prohibitively long for most portable data terminal applications (30 cm for a 100  $\mu$ s signal). The analysis that follows, therefore, employs CCDs as the chosen means of implementing the tapped delay line that is essential to the operation of the matched filter.

There are two ways to implement CCDs in a silicon CMOS process (see [85,88,89] for general references on CCDs). The charge stored under the MOS capacitor can be held either at the interface of the bulk semiconductor and the oxide layer, or the signal charge can be stored away from the oxide interface and inside the

bulk semiconductor through the use of a channel implant. The former method is known as a surface-channel CCD (SCCD), and the latter is known as a bulk- or buried-channel CCD (BCCD). BCCDs have been used extensively for image sensing applications, because —for low signal levels— signal degradation due to carrier trapping effects is less severe in the bulk semiconductor than it is at the semiconductor-oxide interface. However, the charge handling capacity of SCCDs is greater than BCCDs, and it has been shown by Wong *et al.* [90] that when the signal charge is electrically injected into the CCD, the SNR of the SCCDs can be made superior to the SNR of the BCCDs. In addition, SCCDs are inherently more linear than BCCDs, and the SCCD devices can be fabricated in a standard double-poly CMOS process, while the BCCDs require an extra mask step for the buried-channel implant. Thus, for reasons related to power consumption, programmability, linearity, signal integrity, and manufacturability, the analog matched filter in Figure 4.2c that is analyzed in the following discussion is based on a SCCD delay line.

In the configuration that is depicted in Figure 4.2c, a floating-gate tap [91] is attached to every third CCD gate and is used to non-destructively sense the signal charge packets which pass under these gates. The multiply function and reference coefficient storage are achieved by the two-transistor EEPROM structure shown in Figure 4.2c. The reference coefficient voltage  $V_{REF}$  is stored by altering the threshold voltages of the two EEPROMs in a cell via control circuitry not shown in Figure 4.2c. The resulting thresholds are:

$V_{T_1} = V_T - \delta V_{REF}$ ,  
and

$$V_{T_2} = V_T + \delta V_{REF}.$$

The sources of the two EEPROMs are connected to separate current-summing busses, both of which are held at virtual ground. When operating in the triode (or linear) region, the difference between the drain currents through the two EEPROMs is proportional to a multiplication of the drain voltage and the stored reference voltages.

The structure and circuit elements pictured in Figure 4.2c have appeared in the literature in various forms for over two decades [91-94]. This structure is used here because, as far as the authors are aware, it is the most power efficient means to implement an analog parallel programmable matched filter in readily available silicon technology. As such, the structure is suitable for comparison with its digital counterpart.

#### 4.4.2. Analog Matched Filter Power Estimate

The power consumption of the analog matched filter is a function of the signal-to-noise ratio (SNR), where the SNR is defined as the ratio of the maximum signal swing to the physical self-noise of the analog electronics. This relationship is analogous to considering the power consumption of the digital matched filter as a function of quantization level. The analog SNR and the digital quantization level are related via

$$SNR = \sqrt{3}(2^{Q_d} - 2), \quad (4.11)$$

where  $Q_d$  is the data quantization level that is used in (4.2)

The static current of the multiplier/tap structures and the dynamic switching of the CCD gates are the dominant sources of power dissipation within the analog matched filter. The dominant noise sources are the thermal noise of the tap and multiplier FETs and interface trapping effects under the CCD gates [90,95,96]. The problem of flicker noise is assumed to be alleviated by a correlated-double-sampling amplifier [97] on the matched filter output. With these assumptions, and with the aid of the CCD signal capacity and signal quality equations given in [90,96] and the CMOS amplifier noise equations given in [95], an estimate of the power dissipation within the entire analog matched filter is

$$P_{AMF} \equiv 8 \cdot SNR^2 \cdot f_{clk} \cdot kT \cdot N \left( \frac{a(a-b)}{a - \sqrt{ab}} + \frac{b(a-b)}{\sqrt{ab} - b} \right), \quad (4.12)$$

where

$$a = \frac{1}{4} \ln(2) \cdot N \cdot N_{ss} \cdot \frac{q}{C_{ox}} \cdot \frac{V_{DD}}{V_{DD} - \phi_s},$$

$$b = \frac{\sqrt{2} \cdot V_{DD}}{3(V_{DD} - 3V_T)} + \frac{V_{DD}(V_{DD} - 2V_T)}{(V_{DD} - 5V_T/2)V_T},$$

the thermal energy  $KT$  is in units of joules,  $N$  is the number of filter taps,  $f_{clk}$  is the operating frequency,  $N_{ss}$  is the surface state density,  $V_T$  is the threshold voltage of the EEPROM and PFETs (assumed to be equal in magnitude),  $q$  is the charge of an electron,  $C_{ox}$  is the oxide capacitance per unit area, and  $\phi_s$  is the minimum surface

potential under the CCD gates. Note also that the  $a$  term in (4.11) is dependent upon the physical parameters of the CCD fabrication process, while the  $b$  term is dependent upon the bias conditions of the multiplier/tap FETs.

As noted above, an enormous power savings in the digital circuitry is possible by scaling the device dimensions and power supply voltage. These significant savings are generally not realized with the analog matched filter implementation of Figure 4.2c. The decrease in anneal time for thinner gate oxides may lead to an increase in surface state density [98]. Thus, even though the switched capacitance of a scaled analog matched filter may be smaller than the unscaled filter, the supply voltage may need to be increased to offset the negative effects of the increased surface state density within the scaled device. Thus the effect of scaling on the power consumption of the analog matched filter is process dependent. Similar, more general conclusions pertaining to analog circuits and scaling issues are drawn in [99].

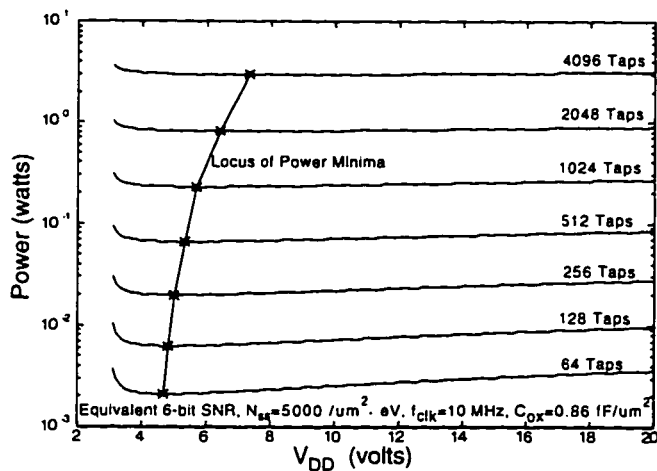


**Figure 4.4** Analog matched filter power as a function of supply voltage and filter length.

The choice of supply voltage is more flexible in the analog filter than in the digital filter. This flexibility exists because a matched filter of equivalent performance can be made from a circuit with a higher supply voltage if the CCD gate areas are decreased. For example, in Figure 4.4 it is shown that only a small change in the power dissipation of the analog matched filter occurs for wide changes in the supply voltage.

## 4.5 Comparison of the Digital and Analog Matched Filter Implementations

Both of the circuit implementations under consideration perform the same operation and use the same physical device —the MOS capacitor— as the primary circuit element. The digital implementation, in treating the MOS capacitor-based devices as binary switches, sacrifices power efficiency for the ability to regenerate weak or degraded signals within the circuit.

The analog implementation uses the fundamental device I-V transistor relationships to efficiently achieve the sum and multiplication functions. However, the analog circuit is unable to regenerate weak or degraded internal signals. Thus, at the cost of additional power consumption, the analog circuit must inject added signal quality (surplus SNR) at the input of the shift register structure, such that the design specifications are satisfied by the degraded signal at the end of the shift register. This difference is depicted in the power consumption equations, which quantify how the

power consumption as a function of filter length increases at a quadratic rate for the analog circuit, while at a less harsh, nearly linear rate for the digital circuit.

The digital implementation is more sensitive to changes in circuit speed. This sensitivity is due to the ability of the digital circuit to exploit a decrease in operating frequency by supporting a corresponding decrease in the supply voltage. The digital circuit is also more sensitive to changes in technology. By decreasing the minimum feature size of the CMOS technology, significant power savings may be realized. This behavior is not necessarily true for the analog circuit, since device physics limit the analog circuit more severely than the digital circuit.

Since changes in filter size, technology scaling, and operating frequency have different effects on the power consumption of the analog and digital circuits, it follows that there may be points in the design space where the digital circuit is more power efficient than the analog circuit, and still other points in the design space where the opposite may be true. The plot shown in Figure 4.5 confirms this expectation. For a

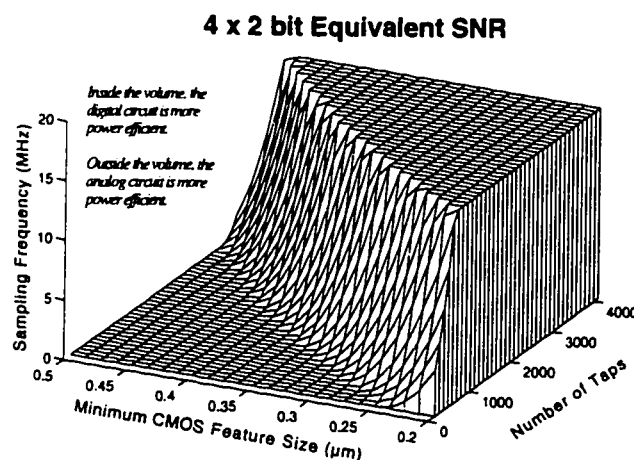


**Figure 4.5** Surface of equal power dissipation for the analog and digital matched filter implementations as a function of filter length, sampling frequency, and technology.

given effective quantization level and for given process parameters, a surface exists in the multidimensional design space that defines the boundary between the regions of superior power efficiency of an analog implementation and a digital implementation of a matched filter. Inside the volume in Figure 4.5, the digital implementation is more power efficient. Outside the volume, the analog circuit is more power efficient.

The surface of equal power dissipation changes position for variations in the quantization level (SNR) and the quality of the analog fabrication process. The plot in Figure 4.6 shows that a digital circuit implementation becomes more preferable to an analog circuit implementation as the level of signal integrity (that is, the quantization level or effective SNR) is increased. In Figure 4.7, a range of positions for the surface of equal power dissipation is shown for four currently available analog processes, with the analog process quality ranging from that of a commercial imaging-CCD foundry in Figure 4.7a to that of an inexpensive digital process (not optimized for analog circuits) in Figure 4.7d. Specific estimates of the power dissipated by the digital and analog circuit implementations may be obtained with (4.10) and (4.12), respectively.

## 4.6 Conclusions

The analog circuit implementation that is described in this chapter is more power efficient for shorter, faster matched filters, and, conversely, the digital circuit is more power efficient where the filters are longer and slower. These generalizations, when coupled with the specific information that is contained in the digital and analog

Comparison for Varying Quantization Level

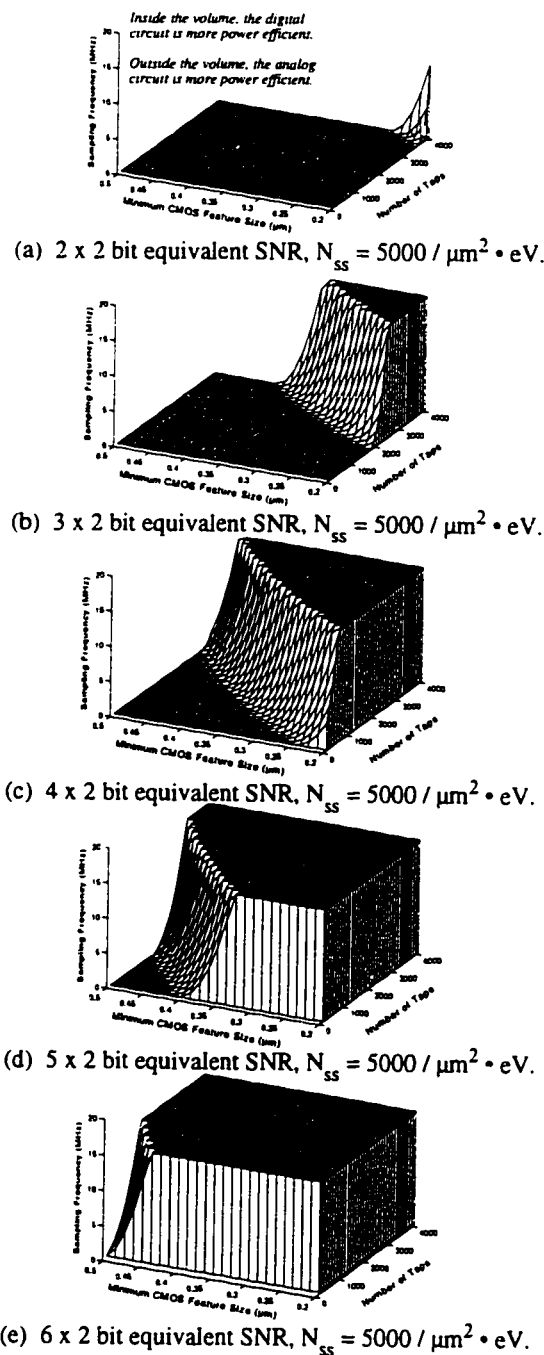


**Figure 4.6** Surface of equal power dissipation for the analog and digital matched filter implementations, demonstrating the effect of varying quantization level (or, equivalently, varying the analog SNR). The  $Q_d \times Q_r$  bit equivalent quantization levels for Figures 6a through 6e are (a) 2 x 2 bit, (b) 3 x 2 bit, (c) 4 x 2 bit, (d) 5 x 2 bit, and (e) 6 x 2 bit. The analog process parameter  $N_{ss}$  has a value of  $5000 / \mu\text{m}^2 \cdot \text{eV}$ .

Comparison for Varying Analog Process Quality

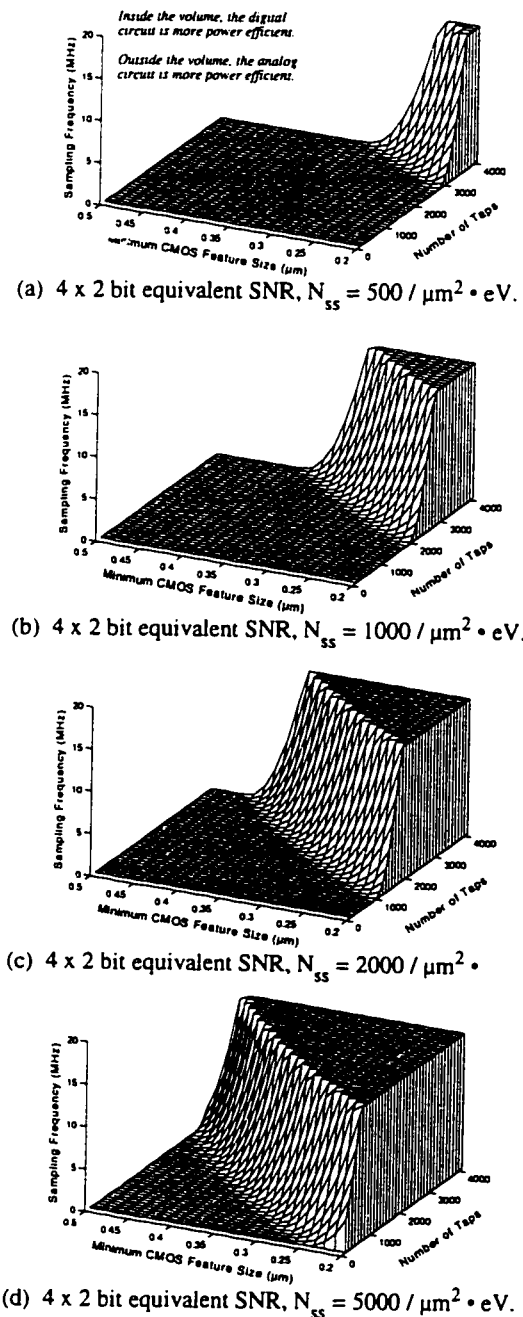


**Figure 4.7** Surface of equal power dissipation for the analog and digital matched filter implementations, demonstrating the effect of improving the quality of the analog fabrication process — as measured by the surface state density,  $N_{ss}$  (smaller values of  $N_{ss}$  indicate a superior analog process). Figures 7a through 7d are for a 4 x 2 bit equivalent SNR and  $N_{ss}$  values of (a)  $500 / \mu\text{m}^2 \cdot \text{eV}$ , (b)  $1000 / \mu\text{m}^2 \cdot \text{eV}$ , (c)  $2000 / \mu\text{m}^2 \cdot \text{eV}$ , (d)  $5000 / \mu\text{m}^2 \cdot \text{eV}$ .

power equations, (4.10) and (4.12), indicate which circuit-implementing technology yields a more power efficient matched filter for a given set of system and process parameters. These concepts and the preceding analyses may be applied to electronic circuit design in general and provide insight into why the preferred implementation of a 64 bit multiplier or a 2 GHz modulator/upbander is straightforward, while determining the most power efficient means to implement a programmable parallel matched filter requires close investigation.

# Chapter 5 Signal Design Issues and Local Oscillator Mismatch

---

Wireless terminals that are physically separate most often are not able to share the same oscillator source. In such cases, local oscillators are used, the output frequencies of which may have inherent instabilities or imprecisions. The local oscillator mismatch that is the result of these instabilities can lead to signal acquisition problems. In this paper, the role of signal design as a tool for combating these problems is discussed. Particular attention is given to the design of signals that are suitable for suppressed carrier CDMA communications. A known code family with the desired properties is presented, and simulation results are given.

## 5.1 Introduction

The nature of wireless communications requires that remote wireless terminals generate local estimates of the RF carrier frequency for the RF-to-baseband downconversion operation. Instabilities and imprecisions due to temperature variations and/or manufacturing limitations can lead to a mismatch in local oscillator

(LO) frequencies between a wireless transmitter and the corresponding receiver or receivers. This mismatch can cause degradation of the signal estimate at the receiver output and complicate signal acquisition. Spread spectrum code-division multiple-access (CDMA) radar and wireless communication systems [1,31] are not exempt from the adverse effects of LO mismatch.

CDMA systems typically employ pulse-compression waveforms and correlation-based processors. The narrowband ambiguity function [29,34], widely used in the radar community as a means of characterizing the delay-Doppler properties of probing waveforms, is also a fitting tool for understanding the effect of LO drift on the output of the matched filter or correlator that may be employed in a CDMA receiver. Shown in Figure 5.1 is the ambiguity function of a generalized CDMA signal, demonstrating the effect of LO mismatch—characterized by  $f_{\text{offset}}$ —on the output of a correlation-based receiver. In the figure,  $T$  and  $W$  are the time-length and bandwidth, respectively, of the transmitted waveform. Waveforms are

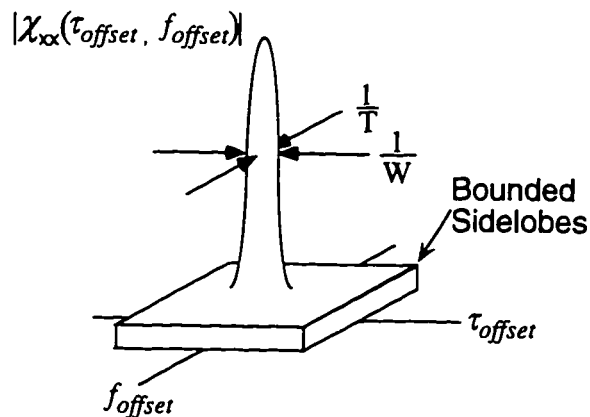


Figure 5.1 Generic ambiguity function.

often designed so that their ambiguity functions have a narrow peak in the  $\tau_{\text{offset}}$  -  $f_{\text{offset}}$  space [29,34]. This characteristic permits unambiguous delay and Doppler estimation, but is not necessarily ideal when the goal is to overcome local oscillator drift.

As an example, consider the following. If the  $T = 100 \mu\text{s}$  and the carrier frequency is  $f_O = 2 \text{ GHz}$ , then a LO mismatch of as little as five parts per million is sufficient to remove the ambiguity peak completely from the correlation processor output. The bounded sidelobes are usually quite small relative to the main peak and, therefore, provide no useful information as to the presence or absence of the signaling waveform. In order to acquire the timing of the signaling waveform, a search must be performed via a series of incremental changes of the LO frequency.

## 5.2 Suitable Signals

In order to minimize the search and acquisition time for suppressed carrier CDMA systems in an environment prone to LO mismatch, it is beneficial to employ signals designed to have the following characteristic.

*The area away from the main peak in the ambiguity function of these signals should contain information of sufficiently large energy that will aid the receiver in establishing the correct LO frequency.*

In essence, in the region occupied by the bounded sidelobes in Figure 5.1, one would like to introduce little road signs that point the receiver in the direction of the main ambiguity peak, where the highest SNR is achievable.

The *road sign* property is closely related to the Doppler-invariant property of some radar and sonar waveforms (e.g. [27,103]). In fact, waveforms belonging to the family of FM sweeps (or *chirps*) have ambiguity properties that meet the requirement stated above. The linear FM chirp, for example, has an ambiguity function with a continuous, narrow triangular ridge that sweeps from the  $(\tau_{\text{offset}}, f_{\text{offset}})$  ambiguity coordinates  $(-T, -W)$  to  $(T, W)$ , with a peak at  $(0, 0)$  [27,29,34,103], as shown in Figure 5.2. By adjusting the LO frequency up an increment and then down an increment and then comparing the correlator outputs for the two cases, the receiver of a chirp-based system can determine whether the value of  $f_{\text{offset}}$  is positive, negative, or zero, and correct accordingly. The drawback to the chirp waveforms is that, for a

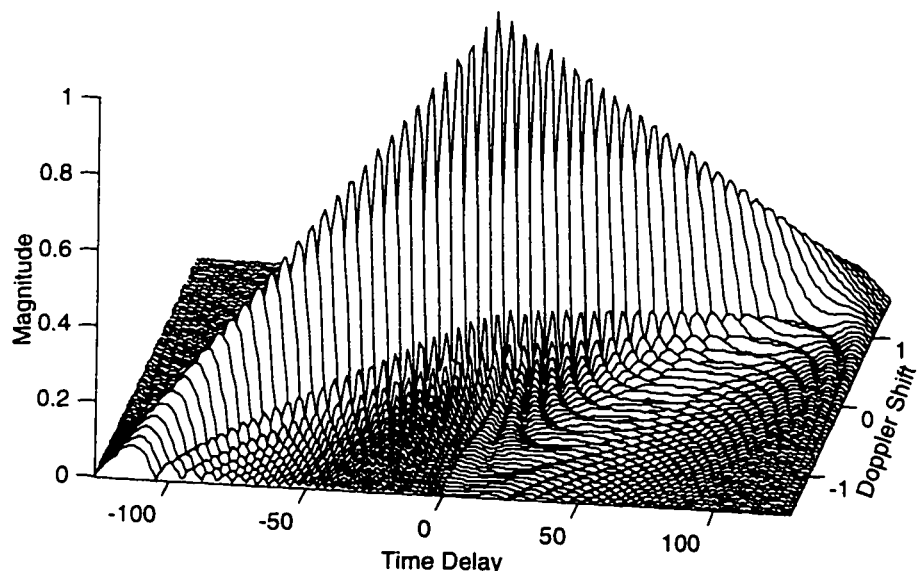


**Figure 5.2** Ambiguity function of a linear FM chirp.

given  $T$  and  $W$ , there are only two waveforms in a family with good cross-ambiguity properties relative to each other, limiting the usefulness of these signals in CDMA applications.

There is a family of waveforms, however, that combines the desirable tolerance to LO mismatch sported by the chirp signals, while also having a large CDMA family size. These are the linear congruence frequency hop (FH) codes [21] defined previously in (2.5) in Chapter 2. For the sake of convenience, the code definition is again given here for the special case of  $b = 0$ . The linear congruence FH codes have hopping patterns defined via the placement operator

$$\alpha_i = (a \cdot i) \bmod p, \quad (5.1)$$

where  $\alpha_i$  is the frequency placement operator for code  $a$  in a family of  $p - 1$  codes,  $p$  is prime, both  $a$  and  $i$  may take integer values in the range  $[1, p - 1]$ , and the postscript *mod p* denotes that the expression is evaluated modulo- $p$ . These FH codes are described by placement operators that are straight lines on the finite field. There are  $p - 1$  codes in a family with  $p - 1$  frequency hops, and there is at most one frequency coincidence in the cross-ambiguity function between any two codes in a family. The hopping patterns for the entire family of linear congruence FH codes are shown in Figure 5.3 for  $p = 11$ .

Shown in Figure 5.4 is the auto-ambiguity function of a unit-energy normalized linear congruence FH code with  $p = 11$ ,  $a = 3$ , and  $T \cdot W = 90$ . An auto-

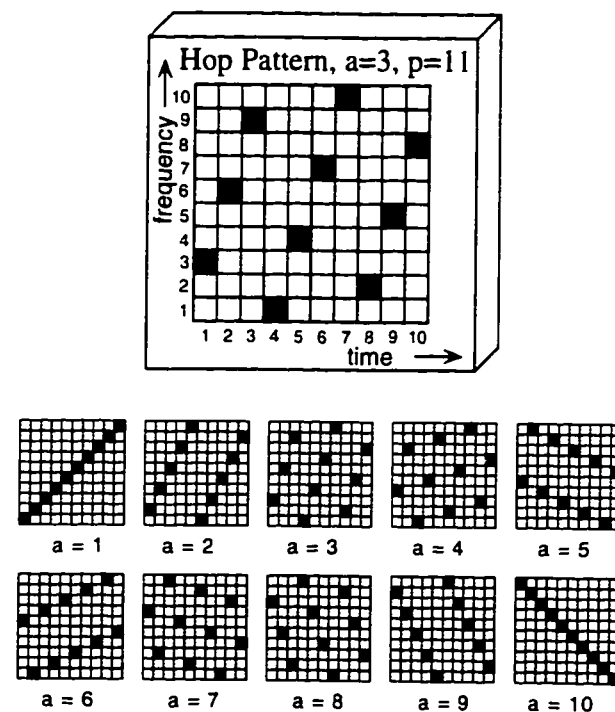


**Figure 5.3** Hopping patterns of the entire linear congruence code family for  $p = 11$ . An enlarged view of the  $a = 3$  code is shown with a description of the axes.

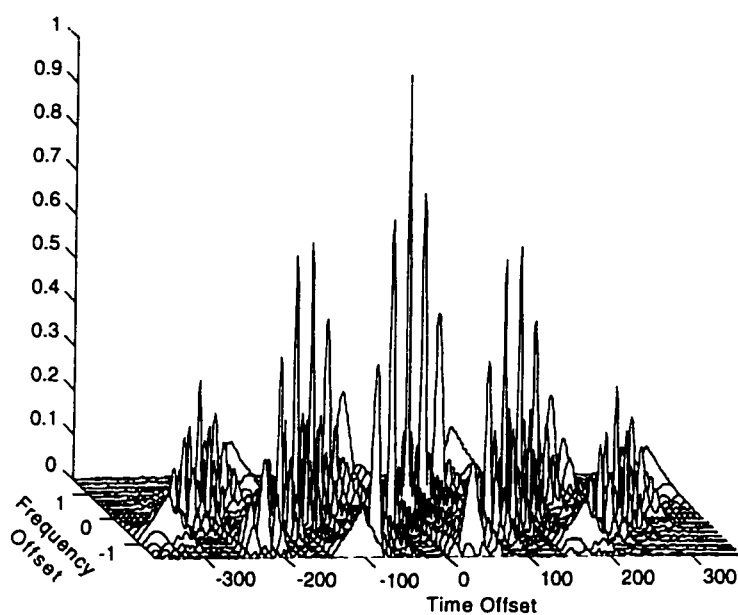


**Figure 5.4** Ambiguity function of the  $a = 3, p = 11$  linear congruence FH code.

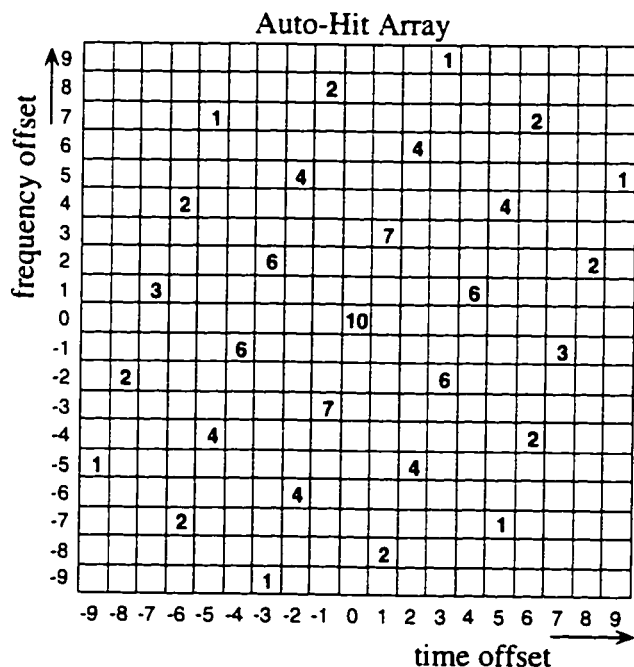


Figure 5.5 Auto-hit array of the  $a = 3, p = 11$  linear congruence FH code.

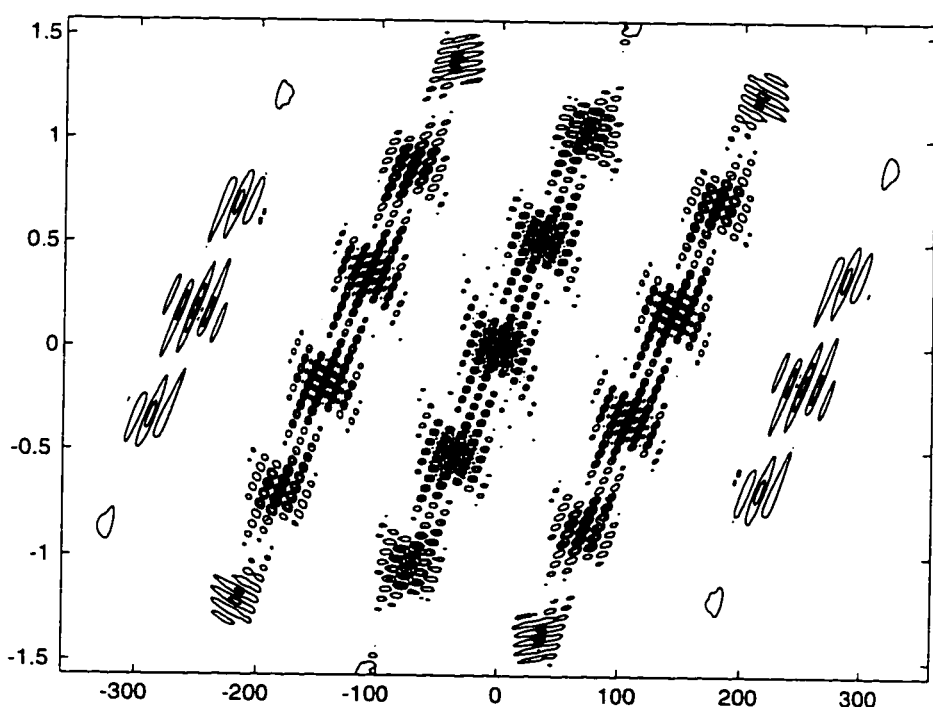


Figure 5.6 Contour plot of the ambiguity function shown in Figure 5.4.

hit array (which may be thought of as a zeroth order approximation to the auto-ambiguity function [104]) of the same signal is shown in Figure 5.5. Note the presence of large peaks in the sidelobe region of the ambiguity function in Figure 5.4. The relative size and position of these peaks is visible from the hit-array of Figure 5.5. In addition, the main lobe and each of the major ambiguity sub-peaks shown in Figure 5.4 is surrounded by a cluster of *grating lobes*, as is visible in the contour plot of Figure 5.6.

### 5.3 An Algorithm for Speedy LO Alignment

The ambiguity function shown in Figures 5.4-5.6 has the characteristics specified above for speedy local oscillator alignment in spread spectrum CDMA receivers. The large amount of signal energy away from the  $\tau_{\text{offset}}-f_{\text{offset}}$  origin of the ambiguity function of the linear congruence FH codes provides the “little road signs” that are sought after, which point in the direction of the main ambiguity peak. Using the knowledge of the position of the main ambiguity sub-peaks and the general distribution of the grating lobes around these sub-peaks (as analytically determined in [21] and [105], respectively), a search algorithm can be invented that will speed the alignment process for a spread spectrum CDMA receiver that receives one of these FH codes. One such algorithm is described below in pseudo-code form.

**Speedy Alignment Algorithm:**

- 1.) Receiver starts at an initial unknown ( $\tau_{\text{offset}}, f_{\text{offset}}$ ) relative to the received waveform.
- 2.) Two correlators are assigned to search in opposite directions in the  $\tau_{\text{offset}}, f_{\text{offset}}$  space for signal energy that surpasses some predetermined threshold.
- 3.) When the threshold is surpassed by one of the correlators, both correlators are used to find the local energy maximum at that region in  $\tau_{\text{offset}}, f_{\text{offset}}$  space.
- 4.) When the local maximum is found, the correlators search at  $\tau_{\text{offset}}$  and  $f_{\text{offset}}$  increments that are consistent with the *a priori* known grating lobe spacing until the main sub-peak in a cluster of peaks is found.
- 5.) When the main sub-peak in a cluster is found, the correlators search at  $\tau_{\text{offset}}$  and  $f_{\text{offset}}$  increments that are consistent with the *a priori* known sub-peak spacing until the main ambiguity peak is found.
- 6.) When the main ambiguity peak is found, the search stops. Receiver alignment has been achieved. The two correlators are then used to track the received signal and maintain the alignment during data transmission and reception.

An algorithm designed for a system which cannot exploit the ambiguity properties of the linear congruence FH codes contains only steps 1.), 2.), and 6.) from the above algorithm. Such an algorithm —as might be used in a system employing binary pseudo-noise (PN) spreading sequences— is, essentially, an exhaustive serial search through all  $\tau_{\text{offset}}, f_{\text{offset}}$  hypotheses until the main ambiguity peak is found.

The benefits of the speedy algorithm are demonstrated pictorially in Figures 5.7 and 5.8. In Figure 5.7, the hypotheses required to achieve receiver alignment are

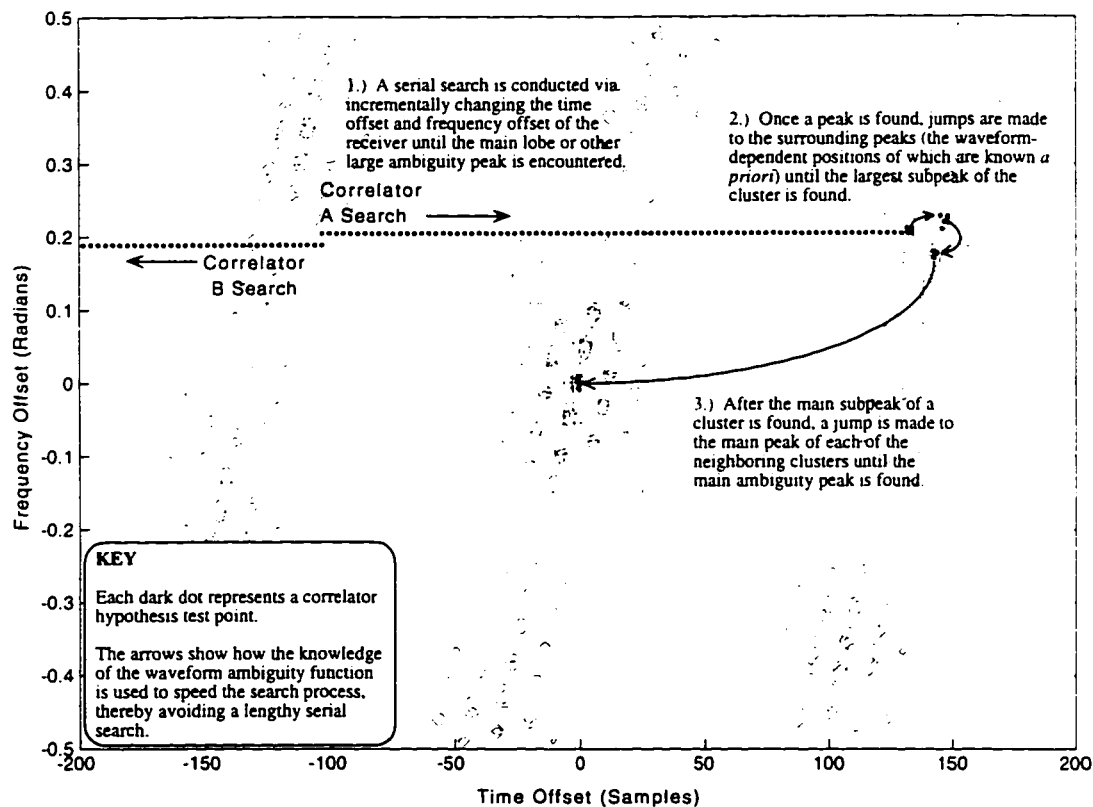


**Figure 5.7** Speedy acquisition/alignment process for linear congruence FH code.

indicated by the dark dots. The hypotheses are overlaid on an enlarged version of the contour plot shown in Figure 5.6. Again, since the receiver initially has no indication as to its offset relative to the received waveform, the receiver must incrementally search until significant signal energy is found. Upon locating the first cluster of grating lobes, the speedy alignment algorithm quickly jumps over large distances in the  $\tau_{\text{offset}}-f_{\text{offset}}$  space, using its knowledge of the ambiguity function of the received signal to efficiently direct the jumps toward the main ambiguity peak. This algorithm is in contrast to Figure 5.8, where the receiver is trying to align to a binary PN code. In such circumstances, a serial search must be performed over the  $\tau_{\text{offset}}-f_{\text{offset}}$  space

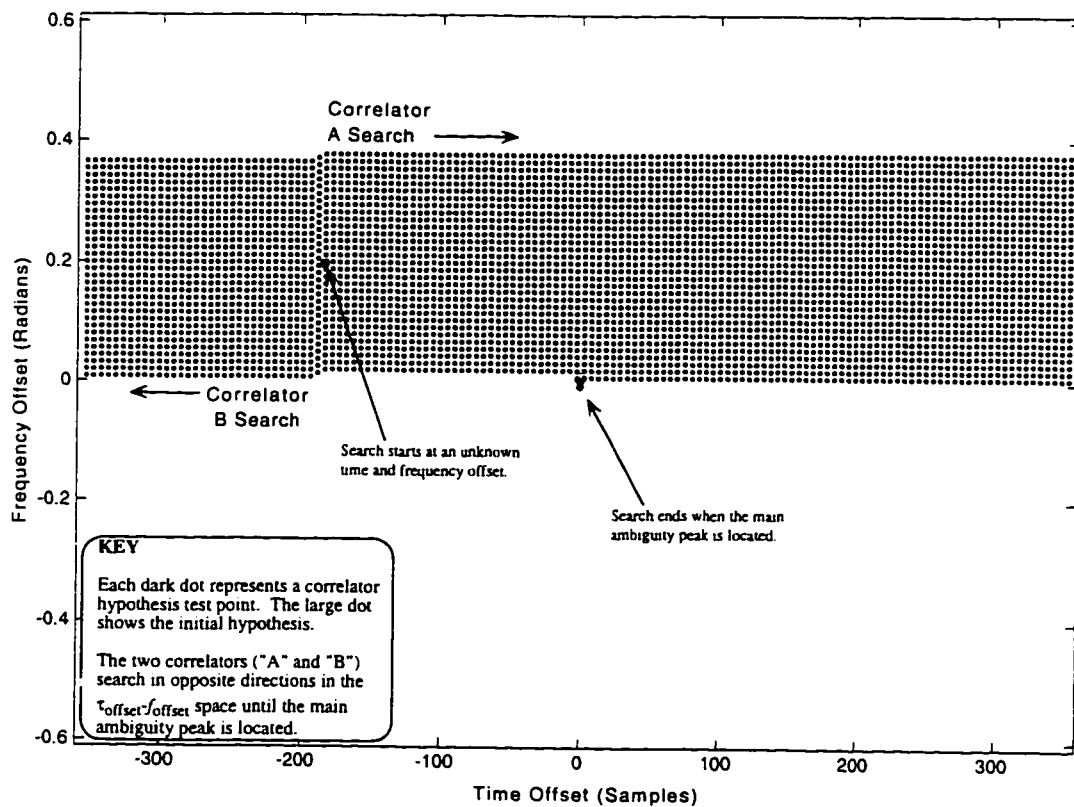


**Figure 5.8** Acquisition/alignment process for a typical spreading waveform.

until the main peak is located.

Simulations verify the performance gains of the speedy algorithm compared to the conventional serial search alignment algorithm. The results are summarized in Figure 5.9. For the speedy algorithm, a linear congruence FH code with  $p = 11$ ,  $a = 3$ , and  $T \cdot W = 90$  is used as the spreading waveform. For the conventional algorithm, a binary PN spreading waveform is used, also with a  $T \cdot W$  product of 90. Each data point represents the average of one thousand simulation runs. The received signal-to-noise ratio is zero dB for all simulation runs. The results are plotted in terms of the average number of correlator search hypotheses required to achieve alignment at

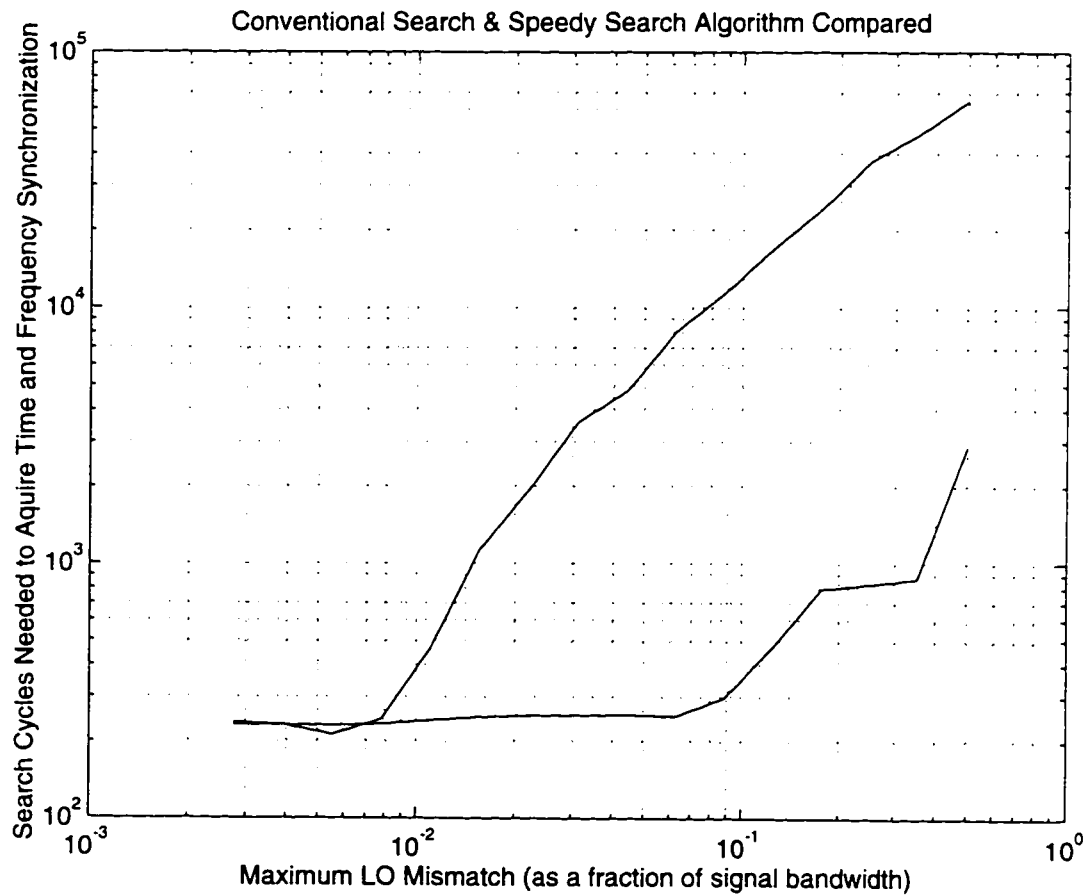


**Figure 5.9** Acquisition time required for the conventional search algorithm (top curve) and the speedy receiver alignment algorithm (bottom curve).

some given level of maximum frequency mismatch. The coherence bandwidth [2] of each of the signals is approximately equal to  $10^{-2} \cdot W$ .

The simulations show that, for frequency offsets less than the coherence bandwidth of the spreading waveform, the speedy algorithm results in little or no performance gain. This result is consistent with expectations, since a frequency offset of less than the coherence bandwidth implies that the main lobe will be encountered on the first  $f_{\text{offset}}$  hypothesis that is tested. For such cases, there is no need for a speedy algorithm. When the  $f_{\text{offset}}$  is larger than the coherence bandwidth,

however, the speedy algorithm clearly shows its worth, with alignment being achieved up to 30 times faster when compared to the conventional algorithm.

## 5.4 Conclusions

Choosing an appropriate signal family can lead to improved search and acquisition properties for CDMA receivers in environments prone to local oscillator mismatch. Guidelines based on the ambiguity properties of spreading waveforms are given for selecting such suitable signals. The family of linear congruence frequency hop codes are shown to exhibit the qualities that can lead to improved acquisition time, while still maintaining excellent CDMA properties. The savings in acquisition time afforded by these signals is a function of average local oscillator mismatch, with greater savings being realized for larger mismatches. An algorithm is described for achieving speedy local oscillator alignment in systems which employ linear congruence frequency hop codes. Simulations results were presented which show that, using the guidelines and algorithms put forth in this chapter, a significant reduction in acquisition time can be achieved.

# Chapter 6 Design, Simulation, and Experimental Results for a Parallel Programmable Matched Filter Circuit

---

Described in this chapter is the actual implementation of a matched filter suitable for use in a real-world spread spectrum communication system. This design exercise combines the spread spectrum theory and practical circuit implementation methodologies discussed in Chapters 1 through 5. In section 6.1, the function and benefits of a pseudo-FM spread spectrum modulation and demodulation scheme are outlined. This discussion is used as a motivation for the design and fabrication of a programmable parallel matched filter, presented in section 6.2. The proposed communication system is based on the concepts presented in Chapter 2, while the circuit design follows the methodology presented in Chapter 4. Design decisions and simulation results are discussed, and a summary of the final realization of a matched filter integrated circuit is presented. Conclusions are given in section 6.3

## 6.1 Pseudo-FM Asynchronous CDMA Wireless Voice

Analysis [31] and field tests [41] have shown that a digital spread spectrum CDMA system is able to provide more simultaneous voice calls over existing cellular telephony bands than either the recently proposed digital time-division multiple-access (TDMA) scheme [100] or the old analog advanced mobile phone system (AMPS). Digital voice communication systems, such as the CDMA or TDMA cellular systems, however, rely on sophisticated and computationally intensive compression and decompression algorithms which convert a voice signal to and from a low bit-rate (less than 10 kbits / second) data stream that is suitable for transmission over a wireless channel. Digital voice coding procedures often require a dedicated digital signal processor (DSP) chip that is capable of performing tens of millions of operations per second [101] and which may consume many milliwatts of battery power [102].

The data in Table 6.1 (adapted from [101]) quantify the computational burden of a given level of compression for a number of voice compression algorithms. The required burden is characterized by the number of millions of instructions per second (MIPS) a processor must execute for a given compression algorithm.

There are applications where the benefits of spread spectrum such as low transmitted power and inherent cryptographic incorporation —both of which are discussed in Chapter 2— may be desirable, while the large CDMA capacity discussed in [8] is not required. In these applications, one may be willing to

**Table 6.1** Computational requirements for 3.2 kHz bandwidth speech coders [101].

Algorithm	Rate (kb/s)	Compression	MIPS	Application
PCM	128	1	0	network
Mu-Law	64	2	0	network
ADPCM	32	4	1	network
LD-CELP	16	8	50	network
LC-CELP	16	8	10	voice messaging coder
RPE-LTP	13.0	9.7	10	digital cellular
VSELP	8	16	24	digital cellular
CELP+	6.8	18.8	30	videophone/digital cellular
RCELP	4.8	26.7	16	telephone security device
CELP	4.8	26.7	30	security
TFI	4	32	150	digital cellular
LPC10E	2.4	53.3	15	security
TFI	2.4	53.3	120	security

compromise some CDMA capacity in order to simplify and reduce the power consumption of the portable receivers.

In [8], a digital synchronous wireless mobile phone system is described. In this system, a base spread spectrum waveform is transmitted at precise intervals. A change in the phase of this base waveform is used to transmit a binary zero or one. The information is contained in the phase of the received signal, and the timing of the signal is used only to align the binary decision circuitry of the receiver.

In an asynchronous spread spectrum CDMA system, the timing of the received waveform can be used to carry the signal data information. By encoding analog voice information, for example, in a pulse-position modulation fashion (as described in Figure 6.1), the receiver may recover the original voice information without the use of a dedicated voice coder or decoder DSP chip at either the

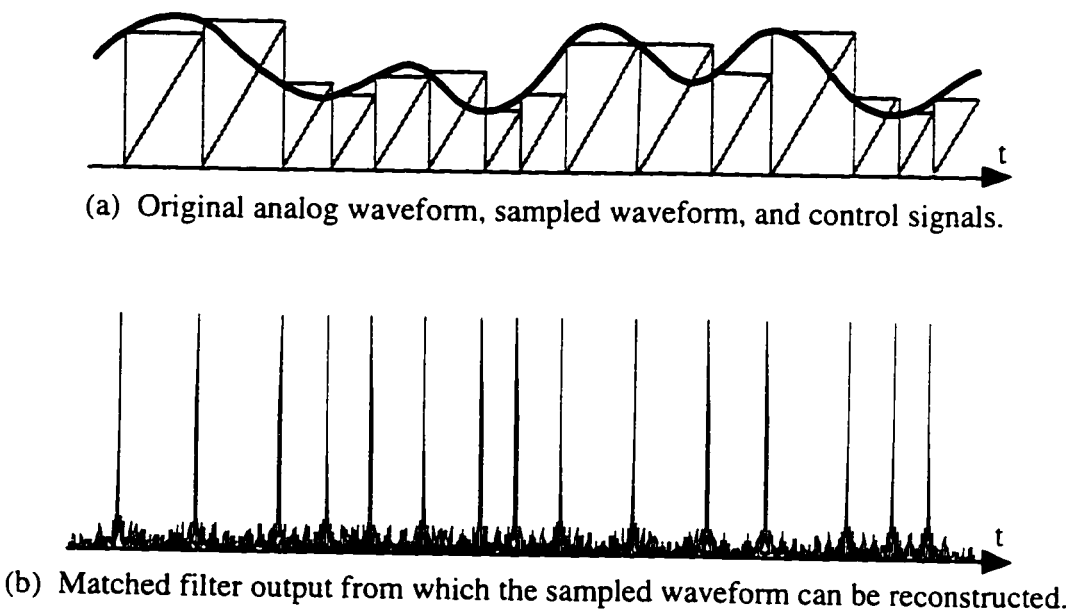


**Figure 6.1** Important waveforms in the pseudo-FM transmitter and receiver. (a) the original analog waveform (smooth thick curve), the sampled waveform (thin solid horizontal line segments), and various control signals (thin gray lines). The length of time between successive transmitted spreading codes carries the amplitude information and time duration of each sample of the analog waveform. Through the use of a matched filter, the receiver is able to recover this timing information, as shown in (b), and reconstruct the sampled waveform.

transmitter or receiver. The overall capacity of an asynchronous CDMA system will typically be somewhat less than a synchronous CDMA system [2], however, in an application such as cordless (in house or in plant) telephony, one may be willing to sacrifice some of the capacity of a synchronous system if the asynchronous system is less complex to implement and/or is less power hungry in an operational mode.

The asynchronous scheme outlined above and in Figure 6.1 may be understood also from the following point of view: A voice signal is used to frequency modulate a low-frequency carrier. At the zero-crossings of the resulting FM waveform, the transmitter transmits a predetermined CDMA waveform.

Through the use of a matched filter, the timing information is recovered at the receiver, facilitating the reconstruction of the original voice signal. This means of transmitting voice information using asynchronous spread spectrum CDMA signaling is referred to in the following pages as pseudo-FM, or PFM.

At the heart of the PFM receiver is a complex (in-phase, I, and quadrature, Q) parallel matched filter. The remainder of this chapter describes the design process, simulation results, and experimental findings related to a matched filter integrated circuit that is suitable for use in a PFM receiver. Since low power consumption is a key requirement for the intended application of cordless telephony, the matched filter design process outlined below follows the methodology presented in Chapter 4.

The filter to be designed requires 64 taps and should operate at sampling frequencies up to 10 MHz. The required effective input data quantization level is 4 bits. The required effective reference coefficient quantization level is 2 bits, allowing ternary tap values of  $\pm 1$  or 0.

## 6.2 Design of an Integrated Circuit Matched Filter

Presented in this section are the design considerations, simulations results, and experimental data derived during the implementation and evaluation of an integrated circuit matched filter. In section 6.2.1, the methodology of Chapter 4 is applied to the design of a specific matched filter. In section 6.2.2, the actual implementation and some of the relevant design decisions are discussed.

### 6.2.1 Process Selection: Analog or Digital?

Following the low-power matched filter design methodology presented in Chapter 4, the first design decision that needs to be made is whether the circuit will be implemented in an analog or a digital process. At the time of consideration, two fabrication processes from the MOSIS service were considered. The first process is a 0.5  $\mu\text{m}$  digital CMOS process. The second process is a 1.2  $\mu\text{m}$  double-poly CMOS process suitable for implementing CCD shift registers and, therefore, analog matched filters. The main performance limiting factor in the 1.2  $\mu\text{m}$  process is the surface-state density,  $N_{ss}$ , which is in the range of  $1000 \sim 10000 \text{ }/\mu\text{m}^2 \cdot \text{eV}$  over the several fabrication runs studied. The plot shown in Figure 4.5 in Chapter 4 at the  $(f_s, L_{\mu\text{m}}, N_{\text{taps}})$  coordinates (10 MHz, 0.5  $\mu\text{m}$ , 64 Taps) pictorially illustrates the position of this design in the design space and indicates that an analog solution is more power efficient than a digital solution for these specific performance goals. Thus, an analog matched filter is implemented in the 1.2  $\mu\text{m}$  double-poly CMOS process available through the MOSIS service and foundried by Orbit Semiconductor, Inc.

### 6.2.2 Matched Filter Circuit Design

The analog matched filter specified in Chapter 4 and pictured in Figure 4.2c is the functional model for the circuit design. The key data path elements for the

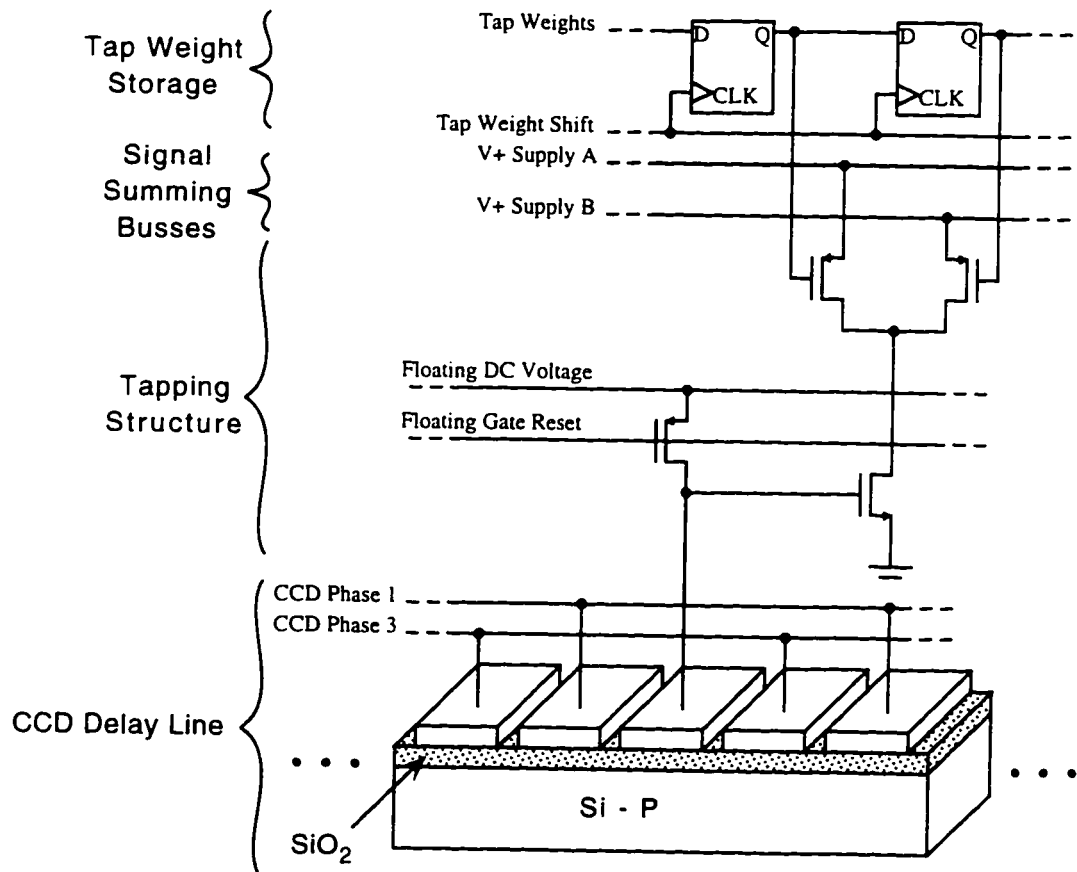


**Figure 6.2** Pictorial and schematic view of a single analog matched filter cell (the “Si - P” term denotes p-type silicon).

implemented circuit are shown in Figure 6.2. The structure in Figure 6.2 is explained in detail in the paragraphs that follow. Special attention is given to those elements that deviate from the model depicted in Figure 4.2c.

#### 6.2.2.1 The CCD Delay Line

The CCD tapped delay line is of critical importance to the performance of the analog matched filter. The noise introduced in the CCD delay line and the tap

sensitivity ultimately limit the effective supported data quantization level for the analog matched filter. The delay line shown in Figure 6.2 is based on a two-and-a-half phase floating-gate tap CCD shift register [88].

In lieu of channel implants that shape the energy bands of the bulk semiconductor under each of the CCD gates, three CCD gates are needed to unambiguously move signal charge in one direction. In the realization pictured in Figure 6.2, two of these gates are clocked by overlapping non-50% duty-cycle square waves, and the third gate in the cell, the tap gate, is held at a constant DC potential. By applying the appropriate clocking signals to the CCD gates, the signal charge can be moved beneath the floating gate. The potential on the floating gate changes in proportion to the amount of signal charge isolated beneath the gate, providing the tapping function required by the matched filter. The floating gate is reset to the specified DC potential at a time when no signal charge is beneath the gate.

The clocking waveforms are shown in Figure 6.3. The sharp rising edge

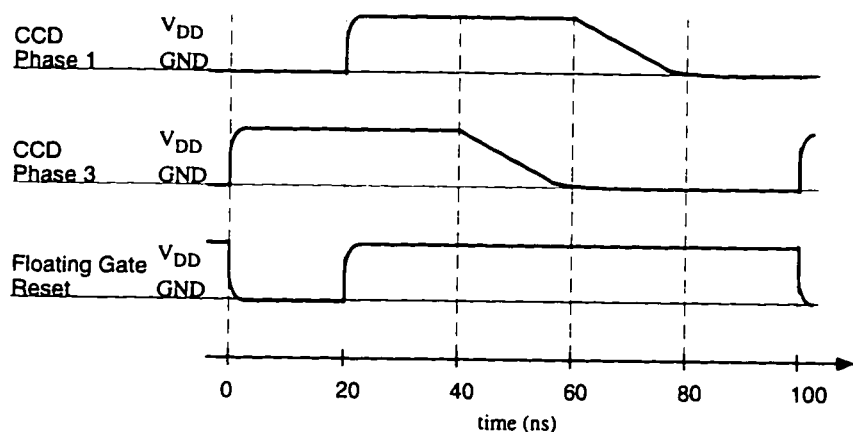


**Figure 6.3** Shape and timing characteristics of the CCD delay line clock waveforms for a system sampling frequency of 10 MHz.

allows charge to move quickly under an active CCD gate. The slow falling edge helps mitigate the backward flow of charge out of the well underneath a gate that is turning off [88,89]. A feature is included in the chip implementation which allows the falling time of the CCD clocking waveforms to be adjusted to minimize signal charge loss between CCD transfers under varying sampling rate applications.

Because the CCD delay line could not be adequately simulated with tools

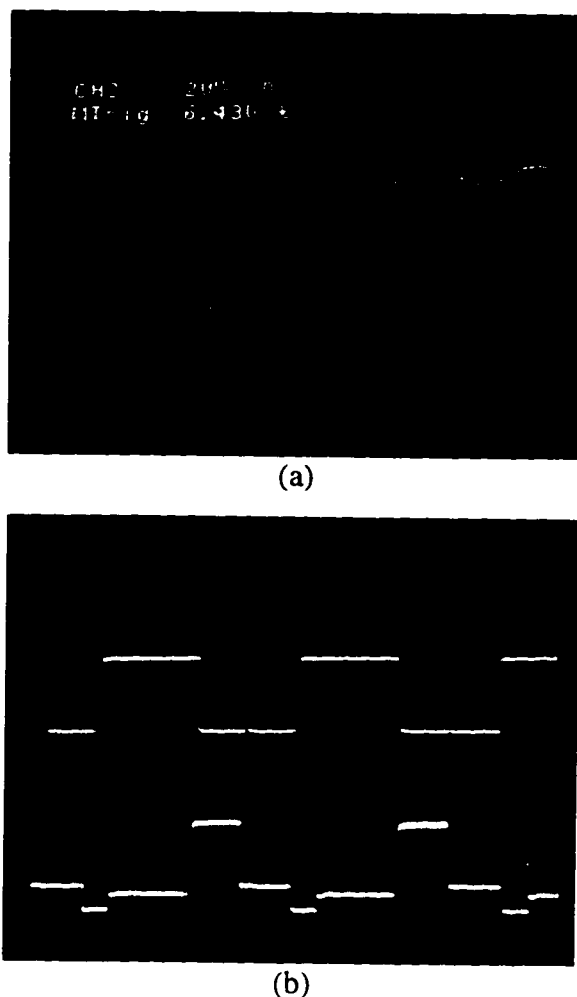


**Figure 6.4** Shown in (a) is an oscilloscope trace of a sinusoidal input (top) and CCD delay line output (bottom). The bottom trace in (b) provides a close-up view of the CCD delay line output waveform. The output is valid during the high amplitude portion of the step-like waveform. The top trace in (b) is the phase 1 CCD clock.

existent at the University of Rochester, a test chip was fabricated to aid in the matched filter design process. This test chip contained several different CCD delay lines with several different tapping structures. Oscilloscope traces of the tapped CCD delay line output from the test chip is shown in Figure 6.4. Photographs of the test environment and circuit under test are shown in Figures 6.5 and 6.6, respectively.

The clocking circuitry of the CCD delay line is the major source of power dissipation in the analog matched filter. The typical oxide thickness in the 1.2  $\mu\text{m}$  CMOS process is approximately 240  $\text{\AA}$ , leading to a value for  $C_{OX}$ , the gate capacitance per unit area, of approximately 1.43 fF /  $\mu\text{m}^2$ . The average CCD gate area is 34.5  $\mu\text{m}^2$ , and there are two clocked gates in each of the cells for each of the 64 tap I and Q filters. Thus, the total switched capacitance associated with the CCD delay lines is approximately 12.8 pF. The voltage level of the CCD clocks is

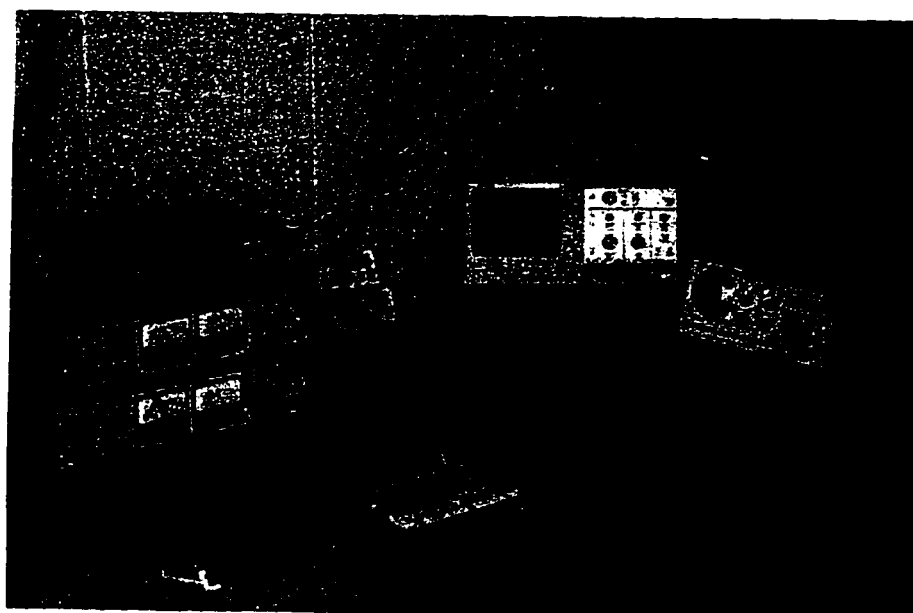


**Figure 6.5** A photograph of the test setup used to obtain the traces shown in Figure 6.4.

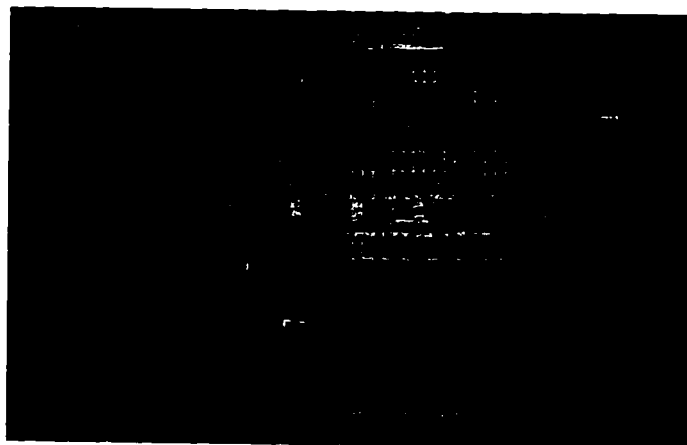


**Figure 6.6** A close-up view of the circuit under test.

flexible, permitting manipulation of the effective SNR (see (4.12) of Chapter 4) based on system requirements. The contribution of the dynamic CCD gate clocking to the total power dissipation of the chip is roughly 12.8 mW at a supply voltage level of 10 V and a sampling frequency of 10 MHz. At a power supply voltage level of 3 V and a sampling frequency of 1 MHz, the clocking of the CCD gates dissipates 115  $\mu$ W. These two data points bracket the anticipated usable range of the device. In practice, the actual power dissipation may be greater than the numbers specified above. Large clock drivers are employed to achieve the speed of operation and waveform shape required by the analog matched filter. These drivers are less than 100% efficient, and simulation results indicate that the driver inefficiencies may double the power estimates given above.

#### 6.2.2.2 The CCD Floating Gate Taps

The design of the floating gate taps involves a tradeoff between sensitivity and dynamic range. The voltage on the floating gate tap changes according to the relation [88],

$$\Delta V_{FG} \equiv V_{SIG} \cdot \frac{C_{GATE}}{C_L}, \quad (6.1)$$

where  $V_{SIG}$  is the sampled signal voltage,  $C_{GATE}$  is the capacitance of the CCD floating gate, and  $C_L$  is a combination of the gate capacitance of the tap transistor and any other parasitic capacitances on the floating gate node. A small  $C_L$  will result in a high tap sensitivity, however, if the tap voltage changes too much, the potential well that holds the signal charge associated with  $V_{SIG}$  will collapse, and the signal will be lost. A large value of  $C_L$  ensures that the potential well will not collapse, but permits only a small change in the floating gate voltage for large variations of the signal voltage.

A value of  $C_L$  equal to approximately  $5 \cdot C_{OX}$  is chosen for the circuit under consideration because this value leads to a tap sensitivity and dynamic range well suited to the anticipated input signal levels. This choice implies that a 5 V change in the value of  $V_{SIG}$  will result in a 1 V change in the floating gate potential.

### 6.2.2.3 Tap Weight Storage and Signal Summing Busses

In Chapter 4, the use of EEPROM-type devices is suggested as a means of

storing the tap weights at each cell in the tapped delay line of the analog matched filter. The design in Figure 6.2 deviates from that suggestion for two reasons: Firstly, the 1.2  $\mu\text{m}$  CMOS process for which the design is targeted does not support the thin oxide layer required for EEPROM devices, and, secondly, the circuit design, in this case, calls only for ternary tap weights, having values of  $\pm 1$  or 0. As a result, two normal PFETs are used as current routing transistors (these are the PFETs at the top of Figure 6.2, the gates of which are connected to the outputs of the registers).

The tap contribution to the total matched filter output is measured by calculating the difference in current flowing from each of the two V+ supplies (“Supply A” and “Supply B” in Figure 6.2). By turning on only the PFET connected to Supply A, the tap weight has a value of +1. Conversely, by turning on only the PFET connected to Supply B, the tap weight has a value of -1. By either turning both of the PFETs on or by turning both of the PFETs off, a value of 0 is assigned to the tap (since the tap weight is determined by the difference in the current flowing through each of the PFETs).

In lieu of the EEPROM option, the tap weights are controlled via a digital shift register. A single 128 stage digital shift register controls each of the 64 tap I and Q matched filters on the chip. The tap coefficient pairs are shifted serially into this pipeline, requiring only a single data input pin and a “shift enable” pin in the final chip package.

#### 6.2.2.4 Other Chip Features

In addition to the programmable parallel matched filter, the chip includes much of the control circuitry associated with the operation and testability of the filter. These features include on-chip digital clock generation circuitry, an input sample-and-hold amplifier for each of the two filter channels, an on-chip output differential transconductance amplifier for each of the two filter channels, and observability circuitry for system setup and test.

Control of the CCD gate voltages and input structures requires six different clock signals. Each of these clock signals is derived from a master input clock which runs at 2.5 times the sampling frequency of the filter. The registers used in the clock generation circuitry are double-edge-triggered flip flops [107]. These registers trade silicon area for lower power dissipation than the typical single-edge-triggered registers. The clock generation circuitry can be operated from a power supply that is separate from the analog power supply of the chip. This separate power supply assists in reducing switching noise in the analog circuit and allows a low voltage to be used in the clock generation circuitry while a higher voltage is used in the analog portion of the chip. The clock generation circuitry is designed to run at voltages as low as 1.75 V. With a digital supply voltage of 3.0 V and an input clock frequency of 25 MHz, simulations indicate that the digital clock generation circuitry dissipates roughly 3.0 mW.

On-chip sample-and-hold amplifiers (SHAs) may be used to reduce input sample distortion when the system sampling frequency approaches the bandwidth of

the input signal. A separate SHA is included for each of the two filter channels (I and Q) on the chip. The SHAs also perform part of the level shifting required to bring a zero-mean input signal into the voltage range required at the CCD delay line input. The SHAs are bypassable, permitting the option of feeding the CCD delay line directly with the input signal. At a sampling frequency of 10 MHz and an analog supply voltage level of 10 V, the SHAs dissipate about 1 mW per channel.

The on-chip differential transconductance amplifiers convert the differential current-based signal of the analog matched filter output to a single-ended voltage signal suitable for transmission off of the chip. The transconductance amplifiers and the pin-driving source-followers used to drive the output pin together dissipate about 2.6 mW per channel at a sampling frequency of 10 MHz and an analog supply voltage level of 10 V (according to simulations).

#### **6.2.2.5 Chip Floorplan and Design Statistics**

The layout of the entire chip was done manually using the tool Magic available at the University of Rochester. All simulations were performed using SPICE Level 3, also available at the University of Rochester. The chip was fabricated using the MOSIS service, which brokered the part to Orbit Semiconductor, Inc. for the actual foundry work. The final chip floorplan is shown in Figure 6.7, and a chip microphotograph is shown in Figure 6.8. The active area occupied by the matched filter in the 1.2  $\mu\text{m}$  double-poly CMOS process is 1050  $\mu\text{m}$  by 1040  $\mu\text{m}$ , or

about 1.1 mm<sup>2</sup>. The active area of the chip, including the pad ring, is 1935  $\mu\text{m}$  by 1941  $\mu\text{m}$ , for a total active area of 3.765 mm<sup>2</sup>. The actual size of the final die is 2200  $\mu\text{m}$  by 2200  $\mu\text{m}$ , or 4.84 mm<sup>2</sup>. The chip contains approximately 8000 transistors, in addition to the two 64-stage CCD delay lines. The circuit has 22 input pins and 4 output pins. The digital supply voltage level is flexible, permitting the digital inputs to be TTL and CMOS compatible. The option of TTL input compatibility may be sacrificed for lower power dissipation, if desired. The final package for the circuit is a 40 pin dual in-line (DIP) ceramic package that is the standard option available through the MOSIS service.

To date, tests have been performed that verify the functionality of the on-chip digital control circuitry and the analog delay line observability tap. A layout error was found, however, that causes a disconnect between the CCD input structure and

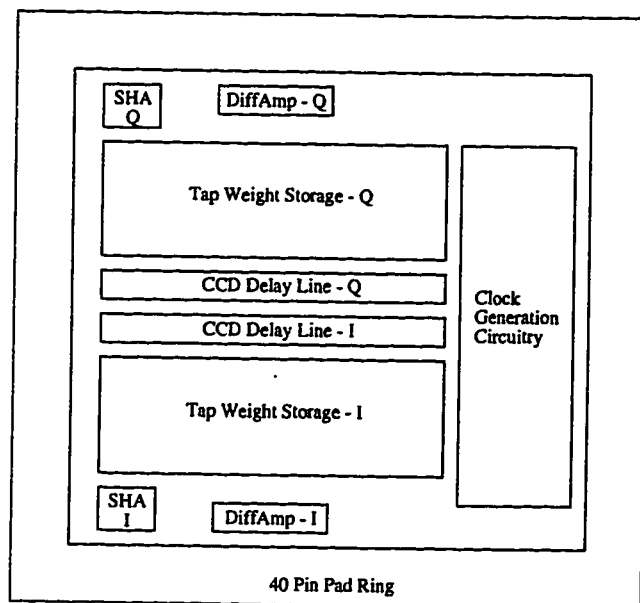


Figure 6.7 Matched filter chip floorplan.

one of the on-chip generated clock signals. The observability features of the chip allow this clock signal to be replaced by an externally generated signal. Work is underway to achieve this, using a programmable logic device as the new clock generator.

### 6.3 Conclusions

A spread spectrum wireless voice communication system is presented as a motivation for the design and construction of a low-power parallel programmable

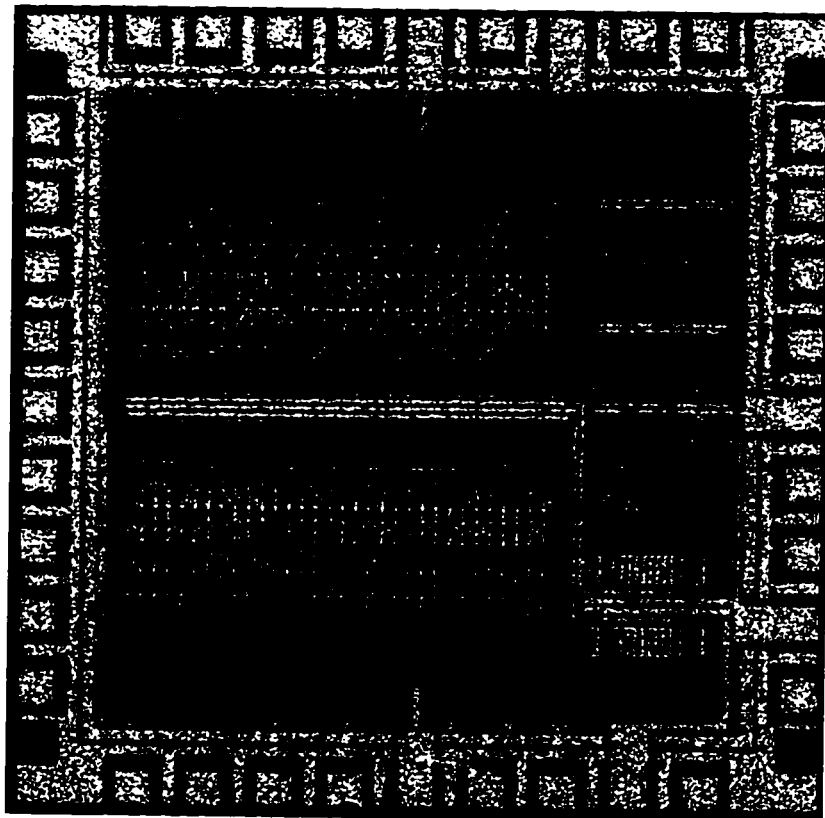


Figure 6.8 Matched filter chip microphotograph.

matched filter. Applying the methodology presented in Chapter 4 to the design of this circuit led to the conclusion that an analog circuit is the most power efficient solution for the given set of operating and process parameters. An analog matched filter was designed, simulated, and fabricated. The pertinent chip features and specifications are presented in Table 6.2. This exercise demonstrates that powerful spread spectrum receivers can be fabricated in a small silicon area while consuming small amounts of power. The analog matched filter performs over one billion multiply-add operations per second and dissipates approximately 50 mW of power in a standard 1.2  $\mu\text{m}$  CMOS process.

**Table 6.2** Summary of chip features and specifications.

---

FEATURES	
• Two 64-tap (I & Q) parallel programmable matched filters	
• Two sample-and-hold amplifiers	
• Two transconductance amplifiers with pin drivers	
• Low voltage clock generation circuitry	
• Test and observability provisions	
SPECIFICATIONS	
Process Technology:	1.2 $\mu\text{m}$ CMOS, double-poly, double-metal
Matched Filter Area:	1.1 $\text{mm}^2$
Total Die Size:	4.84 $\text{mm}^2$
I/O Pins:	22/4
Package:	40 Pin DIP
Number of transistors:	6109
Sampling Frequency:	Up to 10 MHz
Effective Input Quantization:	4 bits
Effective Tap Quantization:	2 bits
Analog Supply Voltage Level:	Up to 10 V
Digital Supply Voltage Level:	Down to 1.75 V
Total Chip Power Dissipation:	-50 mW (@ 10 MHz $f_s$ )

---

# Chapter 7 Summary and Conclusions

---

The dissertation goals, as stated in Chapter 1, have been accomplished. The development and characterization of a signal processing tool suitable for use in estimating the channel parameters in a Doppler multipath environment are presented in Chapter 3. A methodology for choosing the appropriate implementing technology for low-power integrated circuit matched filters is described in Chapter 4. The signal design issues associated with local oscillator mismatch and signal acquisition are discussed in Chapter 5. The design and evaluation of an integrated circuit parallel programmable matched filter are presented in Chapter 6. A brief review of the contributions of this work are given in this chapter.

## 7.1 Review of Dissertation Contributions

A signal processing tool for use in multipath environments where the specular reflectors are in motion relative to the receiver has been developed and characterized. The response of deconvolution algorithms in a Doppler multipath environment has been characterized. It is shown that, when used in conjunction with intelligent

probing signal design, a system based on a bank of Doppler-shifted deconvolution blocks outperforms correlation-based estimators. The time delay resolution of the deconvolution methods in a Doppler environment is shown to approach the sampling period of the system. This behavior is in comparison to correlation-based processors, the delay-resolution of which is limited by the bandwidth of the probing signal. The Doppler resolution of the deconvolution-based systems is shown to equal or surpass the resolution capabilities of correlation-based systems. This increase in resolution for the deconvolution-based systems comes at the expense of increased computational burden.

A design methodology is established for low-power parallel programmable matched filter design. This methodology guides the selection of an appropriate circuit implementing technology for designs where low power consumption is the primary goal. It is shown that the choice of implementing technology is a function of filter length, required effective quantization levels, required filter sampling frequency, and the properties of the fabrication process. A universally power efficient solution is not revealed. Rather, it is shown that, for a given set of process-dependent constants, a surface exists in the multidimensional design space where, on one side of this surface, an analog filter is more power efficient, and, on the other side, a digital circuit is more power efficient. The position of this surface is mapped over a wide range of process technologies and filter parameters, providing a ready reference on which the design of a matched filter may be based. The methodology is applied to the design of an integrated circuit matched filter, and the simulation and

experimental results associated with this design are presented.

A strategy for mitigating the problem of local oscillator alignment within spread spectrum receivers is proposed and evaluated. The strategy involves the design of a novel searching algorithm, as well as signal design guidelines specific to the problem of local oscillator mismatch. The existent family of linear congruence frequency hop codes is shown to possess the ambiguity properties that are key for speedy local oscillator alignment, while also possessing excellent CDMA properties. These codes are used in conjunction with a novel searching algorithm to achieve acquisition times up to 30 times more speedy than conventional methods.

In short, this dissertation describes algorithms, signals, and circuits that may be applied in practice to better the performance of spread spectrum receivers. From the characteristics of the waveform that enters the antenna, to the circuit which locks on to the RF carrier, to the signal processing routine that maps out the wireless channel, and to the multiple-billions-of-operations-per-second filter that recovers the transmitted data from the noisy received signal, this dissertation has —through contributions to each of these areas— successfully contributed to improving the performance of spread spectrum receivers.

## Chapter 8 Future Work

---

This dissertation has expanded the body of knowledge in several key areas related to spread spectrum receiver issues. Much work yet remains however. Even with the world-wide commencement of digital spread spectrum commercial cellular phone systems, research is being directed toward developing techniques to improve existing systems and innovate the next generation of systems. The continued increase in achievable silicon integration levels enables higher complexity receivers to squeeze additional information capacity from adverse communication channels. This brief chapter is directed toward a vision of research that still needs to be done in the area of spread spectrum receiver issues, especially as these areas pertain to the contributions of this dissertation. Items related to multipath parameter estimation are presented in section 8.1. Future work dealing with matched filter power estimation methodologies is presented in section 8.2. Desired advancements in the area of algorithm and signal design for speedy local oscillator alignment are discussed in section 8.3. Prospective explorations in spread spectrum receiver design and matched filter implementation are discussed in section 8.4. Lastly, some concluding remarks are offered in section 8.5.

## 8.1 Future Work in Multipath Parameter Estimation

The work discussed in Chapter 3 establishes new applications for multipath parameter estimation systems based on deconvolution algorithms. Approximate system responses are derived for a specific group of signals, and Doppler resolution superior to correlation methods is demonstrated. The algorithms do not work equally well with all probing signals. A general group of “well-behaved” signals for which the algorithms perform well is loosely defined in Chapter 3, but no precise requirements or analytic arguments are put forth describing the general class of signals which demonstrate similar performance. Future work needs to be directed toward developing a more complete description of the class of signals which may be confidently used in Doppler multipath parameter estimation system.

As is briefly mentioned at the close of Chapter 3, the algorithms and signal design guidelines that are presented for use in Doppler multipath parameter estimation systems may also be used in multipath estimation systems where Doppler is not a relevant parameter. The results described in Chapter 3 demonstrate that information may be gleaned from Doppler-mismatched deconvolution receivers and be applied toward improving multipath delay estimates, even where Doppler is not a concern. In essence, by not looking in the Doppler dimension, information is discarded that may be used to improve system performance. A complete study of this topic, including quantification of the performance gains achievable by adding this extra dimension to the signal space, is an open area of research.

## 8.2 Future Work in Matched Filter Power Estimation

The methodology presented in Chapter 4 offers a strategy for determining the proper technology for a low-power matched filter implementation and describes the relative cost —in terms of circuit power dissipation— of choosing an inappropriate technology. This methodology is based largely on first order circuit effects and assumptions. An improvement to the methodology could be made by considering some of the second and third order effects and incorporating them into the suggested design guide.

One of these improvements could be made by developing a more accurate multiplier power estimation model. The model described in Chapter 4 is common in the literature, but contains simplifications that forge inherent inaccuracies. The model assumes the power is linearly related to the number of single-bit adders required to build the structure. While this assumption appears intuitive at the outset, this type of linear model does not include the increase in switching activity that occurs for larger bit width adders. At large bit widths, an adder in the array multiplier may change state several times as the other adders that feed its inputs settle. This behavior may result in an effective switched capacitance that is several times larger than the actual physical capacitance of the multiplier elements, and is non-linearly related to the input quantization levels. This work has not been adequately addressed in the literature and has applications to general purpose

microprocessor arithmetic logic units and general purpose finite impulse response filters, as well as matched filters.

The model presented in Chapter 4 does not include the impact of technology on the system components that surround and support the matched filter. The digital circuit, for example, requires a fairly high speed analog-to-digital converter further upstream in the signal path. The analog matched filter requires high speed clock drivers, the power efficiencies of which are less than ideal. The desired form of the output data will also impact the total power dissipation of the spread spectrum system and may favor either the analog or the digital implementation, depending on how the data following the matched filter need to be processed. These effects are not included in the present model. A description of the contribution of these effects to total system power dissipation would add to the overall utility of the methodology presented in Chapter 4 and is an area of future research.

### 8.3 Future Work in Local Oscillator Alignment

As described in Chapter 5, initial signal acquisition and local oscillator alignment are complicated in spread spectrum systems by the narrow response in the frequency offset dimension of most typical correlation-processed waveforms. A method is presented in Chapter 5 which yields significant reductions in signal acquisition time through intelligent signal and algorithm design. The experimental results demonstrate improvements in acquisition time by up to a factor of 30 for

spread spectrum signal acquisition in noise. An analytic quantification of the typical savings in acquisition time for algorithms based on the concepts of Chapter 5 is desirable, and future work is recommended on this subject.

Also, it is shown in Chapter 5 that the family of linear congruence frequency hop codes have properties which make them useful in a CDMA environment where speedy signal acquisition is necessary. General guidelines are given in Chapter 5 for designing other CDMA signals that also have these desirable properties. Future work needs to be directed toward finding or designing other families of codes that follow these guidelines and which yield improvements in acquisition time in an environment prone to local oscillator mismatch.

## 8.4 Future Work in CDMA Receiver Integration

In Chapter 6, the design of a parallel programmable matched filter is presented, where the methodology presented in Chapter 4 is used as a guide. Much was learned in the design process that will benefit future implementations of spread spectrum receivers.

From an area perspective, the analog datapath circuitry in the circuit implementation described in Chapter 6 and pictured in Figure 6.5 is dwarfed by the digital coefficient storage. The digital storage scheme is used because a thin oxide was not available for EEPROM devices. Future versions of the analog matched filter built in more advanced technologies stand to save a fair amount of silicon real estate

by using EEPROM devices in place of a digital register for coefficient storage.

In general, higher levels of integration should lead to lower total system power. This is true, since it is a fairly power-intensive task to drive the large capacitive loads associated with off-chip package pins. The integrated circuit described in Chapter 6 contains only the matched filter and some supporting circuitry. A future realization should include the pseudo-FM voice demodulator and, possibly, the speaker amplifier to reduce off-chip interaction and lower overall system power dissipation.

A method for achieving power savings while driving large capacitive loads is introduced in [106]. This method uses auxiliary storage capacitors to recycle some of the energetic charge that is normally routed from a switching capacitive node to ground during every complete cycle of a clock. The method is well suited to driving the large capacitive loads associated with the CCD clock phases and may result in power savings of up to 50%. A future realization of a CCD-based matched filter would benefit from the incorporation of such a scheme.

Most dedicated CCD processes still have relatively large feature sizes. This characteristic is due to the fact that the main applications of CCDs today is that of electronic cameras and camcorders. For these applications, it is necessary to keep the CCD gate/pixel size large enough such that optical diffraction is properly limited. CCDs for signal processing applications may be implemented in any CMOS process that has a two layer polysilicon option. Depending on how the oxide layer and surface state density change for smaller technologies, per the discussion of Chapter 4,

section 4.4.2, a smaller technology may or may not result in a lower power matched filter. A smaller technology is, however, likely to result in a smaller—and, therefore, cheaper—circuit. Research that investigates the performance of analog matched filters at scaled processes is lacking in the literature and is an area of future research.

## 8.5 Concluding Remarks

It is the hope of the author that the research results presented in this dissertation will kindle interest in all areas of spread spectrum system design and implementation and that a union between the signal processing theory and circuit realization will foster a novel breed of communication services and devices.

## Bibliography

- [1] R.C. Dixon, *Spread Spectrum Systems with Commercial Applications*, Wiley, New York, 1994.
- [2] M.K. Simon, *et al.*, *Spread Spectrum Communications Handbook*, McGraw-Hill, New York, 1994.
- [3] R.L. Pickholtz, D.L. Shilling and L.B. Milstein, "Theory of Spread-Spectrum Communications—A Tutorial," *IEEE Transactions on Communications*, Vol. COM-30, No. 5, pp. 855-884, May 1982.
- [4] J.K. Hinderling, *et al.*, "CDMA Mobile Station ASIC," *IEEE Journal of Solid-State Circuits*, Vol. SC-28, No. 3, pp. 253-260, March 1993.
- [5] D.T. Magill, *et al.*, "Spread-Spectrum Technology for Commercial Applications," *Proceedings of the IEEE*, Vol. 82, No. 4, pp. 572-584, April 1994.
- [6] Y.C. Lee, "Overview of Cellular CDMA," *IEEE Transactions on Vehicular Technology*, Vol. VT-40, No. 2, pp. 291-302, May 1991.
- [7] B. Tuch, "Development of WaveLAN, an ISM Band Wireless LAN," *AT&T Technical Journal*, pp. 27-37, July/August 1993.
- [8] EIA/TIA/IS-95 Interim Standard, Telecommunication Industry Association, July 1993.
- [9] J.G. Proakis, *Digital Communications*, McGraw-Hill, New York, 1983.
- [10] C.E. Shannon, "A Mathematical Theory of Communication," *Bell System Technical Journal*, Vol. 27, pp. 379-423, July 1948.
- [11] C.E. Shannon, "A Mathematical Theory of Communication," *Bell System Technical Journal*, Vol. 27, pp. 623-656. October 1948.
- [12] S.W. Golomb, *Shift Register Sequences*, Holden-Day, San Francisco, 1967.
- [13] R. Gold, "Optimal Binary Sequences for Spread Spectrum Multiplexing," *IEEE Transactions on Information Theory*, Vol. IT-13, pp. 619-621, October 1967.
- [14] R. Gold, "Maximal Recursive Sequences with 3-Valued Recursive Cross Correlation Functions," *IEEE Transactions on Information Theory*, Vol. IT-14, pp. 154-156, January 1968.
- [15] T. Kasami, "Weight Distribution Formula for Some Class of Cyclic Codes," University of Illinois, Urbana, Illinois, Tech. Report No. R-285, April 1966.

- [16] D.V. Sarwate and M.B. Pursley, "Cross-Correlation Properties of Pseudo-Random and Related Sequences," *Proceedings of the IEEE*, Vol. 68, No. 5, pp. 593-619, May 1980.
- [17] L.R. Welch, "Lower Bounds on the Maximum Cross-Correlation of Signals," *IEEE Transactions on Information Theory*, Vol. IT-20, No. 3, pp. 397-399, May 1974.
- [18] R.S. Mowbray and P.M. Grant, "Wideband coding for uncoordinated multiple access communication," *Electronics & Communication Engineering Journal*, pp. 351-361, December 1992.
- [19] U. Madhow and M.B. Pursley, "Acquisition in Direct-Sequence Spread-Spectrum Communication Networks: An Asymptotic Analysis," *IEEE Transactions on Information Theory*, Vol. 39, No. 3, pp. 903-912, May 1993.
- [20] D.V. Sarwate and M.B. Pursley, "Hopping Patterns for Frequency-Hopped Multiple-Access Communication," *Proceedings of the IEEE International Conference on Communications*, Vol. 1, pp. 7.4.1-7.4.3, 1978.
- [21] E.L. Titlebaum, "Time-Frequency Hop Signals Part I: Coding Based Upon the Theory of Linear Congruences," *IEEE Transactions on Aerospace and Electronic Systems*, Vol. AES-17, No. 4, pp. 490-493, July 1981.
- [22] E.L. Titlebaum and L.H. Sibul, "Time-Frequency Hop Signals Part II: Coding Based Upon Quadratic Congruences," *IEEE Transactions on Aerospace and Electronic Systems*, Vol. AES-17, No. 4, pp. 494-499, July 1981.
- [23] R.M. Mersereau and T.S. Seay, "Multiple Access Frequency Hopping Patterns with Low Ambiguity," *IEEE Transactions on Aerospace and Electronic Systems*, Vol. AES-17, No. 4, pp. 571-578, July 1981.
- [24] J.P. Costas, "A Study of a Class of Detection Waveforms Having Nearly Ideal Range-Doppler Ambiguity Properties," *Proceedings of the IEEE*, Vol. 72, No. 8, pp. 996-1009, August 1984.
- [25] S.V. Maric and E.L. Titlebaum, "A Class of Frequency Hop Codes with Nearly Ideal Characteristics for Use in Multiple-Access Spread-Spectrum Communications and Radar and Sonar Systems," *IEEE Transactions on Communication*, Vol. COM-40, No. 9, pp. 1442-1447, September 1992.
- [26] E.L. Titlebaum, "Frequency- and Time-Hop Coded Signals for Use in Radar and Sonar Systems and Multiple Access Communication Systems," *Proceedings of the Twenty-Seventh Asilomar Conference on Signals, Systems, & Computers*, pp. 1096-1100, November 1993.
- [27] R.O. Rowlands, "Detection of a Doppler-Invariant FM Signal by Means of a Tapped Delay Line," *The Journal of the Acoustical Society of America*, Vol. 37, No. 4, pp. 608-615, April 1965.

- [28] C.E. Cook and M. Bernfeld, *Radar Signals, An Introduction to Theory and Application*, Academic Press, New York, 1967.
- [29] A.W. Rihaczek, *Principles of High-Resolution Radar*, McGraw-Hill, New York, 1969.
- [30] A.J. Viterbi, *CDMA Principles of Spread Spectrum Communication*, Addison-Wesley, Reading, MA, 1995.
- [31] K.S. Gilhousen, *et al.*, "On the Capacity of a Cellular CDMA System," *IEEE Transactions on Vehicular Technology*, Vol. VT-40, No. 2, pp. 303-312, May 1991.
- [32] H. Meyr and R. Subramanian, "Advanced Digital Receiver Principles and Technologies for PCS," *IEEE Communications Magazine*, pp. 68-78, January 1995.
- [33] G.R. Thompson and D.R. Harris, *The Signal Corps: The Outcome (Mid-1943 Through 1945) (United States Army in World War II, Vol. 6, Part 5: The Technical Services, Vol. 3)*. Washington, DC, Off. Chief of Military History, U.S. Army, 1966.
- [34] H.L. VanTrees, *Detection, Estimation, and Modulation Theory Vol. III*, John Wiley and Sons, Inc., New York, 1971.
- [35] *An Overview of the Application of Code Division Multiple Access (CDMA) to Digital Cellular Systems and Personal Cellular Networks*, QUALCOMM Incorporated, Document Number EX60-10010, May 21, 1992.
- [36] *Telephony*, p. 14, February 27, 1995.
- [37] T.S. Rappaport, *Wireless Communications Principles and Practice*, Prentice Hall PTR, Upper Saddle River, NJ, 1996.
- [38] G.L. Turin, "Introduction to Spread-Spectrum Antimultipath Techniques and Their Application to Urban Digital Radio," *Proceedings of the IEEE*, Vol. 68, No. 3, pp. 328-353, March 1980.
- [39] E.J. Baghdady, "Novel Techniques for Counteracting Multipath Interference Effects in Receiving Systems," *IEEE Journal on Selected Areas in Communications*, Vol. SAC-5, No. 2, pp. 274-285, February, 1987.
- [40] D.L. Noneaker and M.B. Pursley, "On the Chip Rate of CDMA Systems with Doubly Selective Fading and Rake Reception," *IEEE Journal on Selected Areas in Communications*, Vol. 12, No. 5, pp. 853-861, June 1994.
- [41] R. Padovani, "The Capacity of CDMA Cellular: Reverse Link Field Test Results," Springer-Verlag, *Mobile Communications, Advanced Systems and Components, Proceedings of the 1994 International Zurich Seminar on Digital Communications*, pp. 56-66, March 1994.

- [42] E.L. Titlebaum, S.V. Maric and J. R. Bellegarda, "Ambiguity Properties of Quadratic Congruential Coding," *IEEE Transactions on Aerospace and Electronic Systems*, Vol. 27, No. 1, pp. 18-29, January 1991.
- [43] B.P. Bogert, M.J.R. Healy and J.W. Tukey, "The Quefrency Alanysis of Time Series for Echos: Cepstrum Pseudo-Autocovariance, Cross-Cepstrum and Saphe Cracking," Chapter 15 in *Time Series Analysis*, edited by M. Rosenblatt, John Wiley and Sons, Inc., 1963.
- [44] Q. Zhang, J. Huang and Y. Xie, "High Resolution Delay Estimation," *IEEE TENCON*, Beijing, pp. 579-583, 1993.
- [45] F. McCarthy, A. Paulraj and T. Kailath, "Eigenstructure Approach to Doppler Estimation for Wideband Signals," *Proceedings of the IEEE International Conference on Acoustics, Speech, and Signal Processing*, Tokyo, pp. 1917-1920, 1986.
- [46] A.M. Bruckstein, T.-J. Shan and T. Kailath, "The Resolution of Overlapping Echos," *IEEE Transactions on Acoustics, Speech, Signal Processing*, Vol. ASSP-33, No. 6, pp. 1357-1367, December 1985.
- [47] S.M. Riad, "The Deconvolution Problem: An Overview," *Proceedings of the IEEE*, Vol. 74, No. 1, pp. 82-85, January 1986.
- [48] P.B. Crilly, "A Quantitative Evaluation of Various Iterative Deconvolution Algorithms," *IEEE Transactions on Instrumentation and Measurement*, Vol. 40, No. 3, pp. 558-562, June 1991.
- [49] J. Biemond, R.L. Lagendijk and S.M. Mersereau, "Iterative Methods for Image Deblurring," *Proceedings of the IEEE*, Vol. 78, No. 5, pp. 856-883, May 1990.
- [50] R.W. Schafer, R.M. Mersereau and M.A. Richards, "Constrained Iterative Restoration Algorithms," *Proceedings of the IEEE*, Vol. 69, No. 4, pp. 432-450, April 1981.
- [51] B.L. Johnson, D.W. Ricker and J.R. Sacha, "The Use of Iterative Deconvolution for Scattering Function Identification," *Journal of the Acoustical Society of America*, Vol. 91, No. 5, pp. 2790-2798, May 1992.
- [52] J.R. Sacha and B.L. Johnson, "A Constrained Iterative Multiple Operator Deconvolution Technique," *Journal of the Acoustical Society of America*, Vol. 96, No. 1, pp. 181-185, July 1994.
- [53] W.L. Gans, "Calibration and Error Analysis of a Picosecond Pulse Waveform Measurement System at NBS," *Proceedings of the IEEE*, Vol. 74, No. 1, pp. 86-90, January 1986.
- [54] J.J. Anaya, L.G. Ullate and C. Gritsch, "A Method for Real-Time Deconvolution," *IEEE Transactions on Instrumentation and Measurement*, Vol.

41, No. 3, pp. 413-419, June 1992.

[55] M.D. Hahm and E.L. Titlebaum, "Multipath Parameter Estimation in the Presence of Doppler by the Method of Projection onto Convex Sets," *Proceedings of the 1994 Conference on Information Sciences and Systems*, Princeton, NJ, pp. 903-908, 1994.

[56] E.T. Copson, *An Introduction to the Theory of Functions of a Complex Variable*, Oxford University Press, London, 1935.

[57] M.D. Hahm, E.L. Titlebaum and Z.I. Mitrovski, "Inverse Filtering in the Presence of Doppler with Application to Specular Multipath Parameter Estimation," *Proceedings of the IEEE International Conference on Acoustics, Speech, and Signal Processing*, pp. 3167-3170, 1995.

[58] D.C. Youla and H. Webb, "Image Restoration by the Method of Convex Projections: Part 1 — Theory," *IEEE Transactions on Medical Imaging*, Vol. MI-1, No. 2, pp. 81-94, October 1982.

[59] M.I. Sezan and H. Stark, "Image Restoration by the Method of Convex Projections: Part 2 — Applications and Numerical Results," *IEEE Transactions on Medical Imaging*, Vol. MI-1, No. 2, pp. 95-101, October 1982.

[60] M.I. Sezan and A. M. Tekalp, "Iterative Image Restoration with Ringing Suppression Using the Method of POCS," *Proceedings of the IEEE International Conference on Acoustics, Speech, and Signal Processing*, pp. 1300-1303, 1988.

[61] A. Levi and H. Stark, "Restoration from Phase and Magnitude by Generalized Projections," Chapter 8 in *Image Recovery: Theory and Applications*, edited by H. Stark, Academic Press, Orlando, 1987.

[62] T.G. Manickam and R.J. Vaccaro, "A Non-Iterative Deconvolution Method for Estimating Multipath Channel Responses," *Proceedings of the IEEE International Conference on Acoustics, Speech, and Signal Processing*, I333-I336, 1993.

[63] Z. Kostic, M.I. Sezan and E.L. Titlebaum, "Estimation of the parameters of a multipath channel using set-theoretic deconvolution," *IEEE Trans. on Communications*, Vol. 40, No. 6, pp. 1006-1011, June 1992.

[64] Z. Kostic, *Spread-Spectrum Coding, Performance Evaluation and Dispersive Channel Estimation for Several Classes of Code-Division Multiple-Access Communication Systems*, Ph.D. Thesis, University of Rochester, College of Engineering and Applied Science, Department of Electrical Engineering, pp. 110-126, 1990.

[65] H.J. Trussell and M.R. Civanlar, "The Feasible Solution in Signal Restoration," *IEEE Transactions on Acoustics, Speech, and Signal Processing*, Vol. ASSP-32, No. 2, pp. 201-212, April 1984.

- [66] M.D. Hahm, Z.I. Mitrovski, and E.L. Titlebaum, "Deconvolution in the Presence of Doppler with Application to Specular Multipath Parameter Estimation," accepted for publication in the *IEEE Transactions on Signal Processing*.
- [67] R.C. Gonzalez and R.E. Woods, *Digital Image Processing*, Addison-Wesley, Reading, pp. 261ff., 1992.
- [68] Emil Wolf, Department of Physics and Astronomy, University of Rochester, Class notes from *Physics 401 Analytical Methods of Theoretical Physics Part I: Complex Analysis*, Fall 1994.
- [69] T.P. Bursh, Jr., *et al.*, "Digital Radio for Mobile Applications," *AT&T Technical Journal*, pp. 19-26, July/August 1993.
- [70] G.L. Turin, "An Introduction to Digital Matched Filters," *Proceedings of the IEEE*, Vol. 64, No. 7, pp. 1092-1112, July 1976.
- [71] B.P. Lathi, *Modern Digital and Analog Communication Systems*, HRW Saunders, USA, 1989.
- [72] G.J.R. Povey and P.M. Grant, "Simplified matched filter receiver designs for spread spectrum communications applications," *Electronics & Communications Engineering Journal*, pp. 59-64, April 1993.
- [73] L.B. Milstein, *et al.*, "Rapid Acquisition for Direct Sequence Spread-Spectrum Communications Using Parallel SAW Convolvers," *IEEE Transactions on Communications*, Vol. COM-33, No. 7, pp. 593-600, July 1985.
- [74] B.B. Ibrahim and A.H. Aghvami, "Direct Sequence Spread Spectrum Matched Filter Acquisition in Frequency-Selective Rayleigh Fading Channels," *IEEE Journal on Selected Areas in Communications*, Vol. SAC-12, No. 5, pp. 885-890, June 1994.
- [75] L.B. Jackson, *Digital Filters and Signal Processing*, Kluwer Academic Publishers, Boston, MA, 1989.
- [76] A.V. Oppenheim and R.W. Schafer, *Discrete-Time Signal Processing*, Prentice Hall, Englewood Cliffs, NJ, 1989.
- [77] M. Hatamian and S.K. Rao, "A 100 MHz 40-Tap Programmable FIR Filter Chip," *Proceedings of the IEEE International Symposium on Circuits and Systems*, pp. 3053-3056, May 1990.
- [78] A.P. Chandrakasan, *et al.*, "Low-Power CMOS Digital Design," *IEEE Journal of Solid-State Circuits*, Vol. SC-27, No. 4, pp. 473-484, April 1992.
- [79] T.K. Callaway and E.E. Swartzlander, Jr., "Optimizing Multipliers for WSI," *Proceedings of the IEEE International Conference on WSI*, pp. 85-94, January 1993.

- [80] T.K. Callaway and E.E. Swartzlander, Jr., "Estimating the Power Consumption of CMOS Adders," *Proceedings of the IEEE Symposium on Computer Arithmetic*, pp. 210-216, June 1993.
- [81] S.Y. Kung, *et al.*, *VLSI and Modern Signal Processing*, Prentice Hall, Englewood Cliffs, 1985.
- [82] N.H.E. Weste and K. Eshraghian, *Principles of CMOS VLSI Design*, Addison-Wesley, New York, 1993.
- [83] R.H. Dennard, *et al.*, "Design of Ion-Implanted MOSFETs with Very Small Physical Dimensions," *IEEE Journal of Solid-State Circuits*, Vol. SC-9, No. 5, pp. 256-268, October 1974.
- [84] H.B. Bakoglu, *Circuit Interconnections and Packaging for VLSI*, Addison-Wesley, Reading, 1990.
- [85] C.H. Séquin and M.F. Tompsett, *Charge Transfer Devices*, Academic Press, New York, 1975.
- [86] R.L. Miller, *et al.*, *Acoustic Charge Transport: Device Technology and Applications*, Artech House, Boston, 1992.
- [87] C. Campbell, *Surface Acoustic Wave Devices and Their Signal Processing Applications*, Academic Press, San Diego, 1989.
- [88] J.D.E. Beyon and D.R. Lamb, *Charge-coupled devices and their applications*, McGraw-Hill, London, 1980.
- [89] D.K. Schroder, *Advanced MOS Devices*, Addison-Wesley, Reading, 1987.
- [90] H.-S. Wong, *et al.*, "TDI CCDs: Design and Applications," *IBM Journal of Research & Development*, Vol. 36, No. 1, pp. 83-106, January 1992.
- [91] P.B. Denyer, *et al.*, "Miniature Programmable Transversal Filter Using CCD/MOS Technology," *Proceedings of the IEEE*, Vol. 67, No. 1, pp. 42-50, January 1979.
- [92] D.R. Lampe, *et al.*, "An Electrically-Reprogrammable Analog Transversal Filter," *Proceedings of the IEEE International Solid-State Circuits Conference*, pp. 156-157, February 1974.
- [94] J.R. Tower, *et al.*, "A CMOS/CCD 256-Stage Programmable Transversal Filter," *IEEE Journal of Solid-State Circuits*, Vol. SC-17, No. 6, pp. 1062-1069, December 1982.
- [94] T. Blyth, *et al.*, "A Non-Volatile Analog Storage Device Using EEPROM Technology," *Proceedings of the IEEE International Solid-State Circuits Conference*, pp. 192-193, February 1991.

- [95] W.M. Leach, Jr., "Fundamentals of Low-Noise Analog Circuit Design," *Proceedings of the IEEE*, Vol. 82, No. 10, pp. 1515-1538, October 1994.
- [96] J.E. Carnes and W.F. Kosonocky, "Noise Sources in Charge Coupled Devices," *RCA Review*, Vol. 33, pp. 327-343, June 1972.
- [97] R.J. Kansy, "Response of a Correlated Double Sampling Circuit to 1/f Noise," *IEEE Journal of Solid-State Circuits*, Vol. SC-15, No. 3, pp. 373- 375, June 1980.
- [98] P. Balk, *The Si-SiO<sub>2</sub> System*, Elsevier, Amsterdam, 1988.
- [99] E.A. Vittoz, "Low-Power Design: Ways to Approach the Limits," *Proceedings of the IEEE International Solid-State Circuits Conference*, pp. 14-18, February 1994.
- [100] Telecommunications Industry Association/ Electronic Industries Association (TIA/EIA) Interim Standard, IS-54-B, *Dual-Mode Mobile Station - Base Station Compatibility Standard*, 1992.
- [101] L.R. Rabiner, "Applications of Voice Processing to Telecommunications," *Proceedings of the IEEE*, Vol. 82, No. 2, pp. 199-228, February 1994.
- [102] E.G. Friedman, S.-M. Kang, E.A. Vittoz, D.J. Allstot, E.P. Harris, and R.-H. Yan, "From 100 Milliwatts/MIPS to 10 Microwatts/MIPS," *Proceedings of the IEEE International Symposium on Circuits and Systems*, Vol. 4, pp. 1-6, May 1994.
- [103] R.C. Thor, "A Large Time-Bandwidth Product Pulse-Compression Technique," *IRE Transactions on Military Electronics*, pp. 169-173, April 1962.
- [104] J.R. Bellegarda, *et al.*, "The Hit Array: A Synthesis Tool for Multiple Access Frequency Hop Signals," *IEEE Transactions on Aerospace and Electronic Systems*, Vol. 29, No. 3, pp. 624-635, July 1995.
- [105] L.A. Osadciw, E.L. Titlebaum, and M.D. Hahm, "Mainlobe Characteristics of Ambiguity Functions for Linear Congruence Codes," to appear in the *Proceedings of the 1997 Conference on Information Sciences and Systems*, March 1997.
- [106] M. Hahm, "Modest Power Savings for Applications Dominated by Switching of Large Capacitive Loads," *Proceedings of the IEEE Symposium on Low Power Electronics*, pp. 60-61, October 1994.
- [107] R. Hossain, L. D. Wronski, and A. Albicki, "Low Power Design Using Double Edge Triggered Flip-Flops," *IEEE Transactions on Very Large Scale Integration Systems*, Vol. 2, No. 2, pp. 261-264, June 1994.

## Publications

### Journal Publications

M. D. Hahm, Z. I. Mitrovski, and E. L. Titlebaum, "Deconvolution in the Presence of Doppler with Application to Specular Multipath Parameter Estimation," accepted for publication in the *IEEE Transactions on Signal Processing*.

M. D. Hahm, E. G. Friedman, and E. L. Titlebaum, "A Comparison of Analog and Digital Circuit Implementations of Low-Power Matched Filters for Use in Portable Wireless Communication Terminals," accepted for publication in the *IEEE Transactions on Circuits and Systems II: Analog and Digital Signal Processing*, June 1997.

S. V. Maric, M. D. Hahm, and E. L. Titlebaum, "Construction and Performance Analysis of a New Family of Optical Orthogonal Codes for CDMA Fiber-Optic Networks," *IEEE Transactions on Communications*, Vol. 43, No. 2, pp. 485-489, February 1995.

### Conference Publications

L. A. Osadciw, E. L. Titlebaum, and M. D. Hahm, "Mainlobe Characteristics of Ambiguity Functions for Linear Congruence Codes," to appear in the *Proceedings of the Conference on Information Sciences and Systems*, March 1997.

M. D. Hahm, E. G. Friedman, and E. L. Titlebaum, "Analog vs. Digital: A Comparison of Circuit Implementations for Low-Power Matched Filters," *Proceedings of the IEEE International Symposium on Circuits and Systems*, Atlanta, GA, Vol. 4, pp. 280-283, May 1996.

M. D. Hahm and E. L. Titlebaum, "Wideband Signal Design Issues and Local Oscillator Drift," *Proceedings of the Conference on Information Sciences and Systems*, Princeton, NJ, pp. 1151-1152, March 1996.

M. D. Hahm, E. G. Friedman, and E. L. Titlebaum, "Receiver Power Issues Related to Matched Filter Implementation for Portable Wireless Communication Terminals," *Proceedings of the IEEE Wireless Communications Systems Symposium*, Smithtown, NY, pp. 211-216, November 1995.

M. D. Hahm, E. L. Titlebaum, and Z. I. Mitrovski, "Inverse Filtering in the Presence of Doppler with Application to Specular Multipath Parameter Estimation," *Proceedings of the IEEE International Conference on Acoustics, Speech, and Signal Processing*, pp. 3167-3180, Detroit, MI, May 1995.

M. Hahm, "Modest Power Savings for Applications Dominated by Switching of Large Capacitive Loads," *Proceedings of the IEEE Symposium on Low Power Electronics*, San Diego, CA, pp. 60-61, October 1994.

S. V. Maric, M. D. Hahm, and E. L. Titlebaum, "Construction and Performance Analysis of a New Family of Optical Orthogonal Codes with Ideal Auto- and Cross-Correlation Functions for Use in CDMA Fiber-Optic LANs," *Proceedings of the IEEE International Conference on Communications*, pp. 136-140, 1994.

M. D. Hahm and E. L. Titlebaum, "Multipath Parameter Estimation in the Presence of Doppler by the Method of Projection onto Convex Sets," *Proceedings of the Conference on Information Sciences and Systems*, Princeton, NJ, pp. 903-908, March 1994.